On the Distances and Energetics of AGN Outflows

Bartlett Douglas Edmonds, Jr.

Dissertation submitted to the Faculty of the
Virginia Polytechnic Institute and State University
in partial fulfillment of the requirements for the degree of

Doctor of Philosophy
in
Physics

Nahum Arav, Chair
Mark Pitt
Eric Sharpe
John Simonetti

August 28, 2013
Blacksburg, Virginia

Keywords: AGN, Active Galactic Nuclei, Quasars, Seyfert Galaxies

On the Distances and Energetics of AGN Outflows

Bartlett Douglas Edmonds, Jr.

(ABSTRACT)

Active galactic nuclei (AGN) ubiquitously show outflows. It is now widely recognized that these outflows are key components in the evolution of super-massive black holes and their host galaxies. As important as these outflows are, we still lack sufficient understanding of their structure and energetics. The majority of the work presented in this thesis involved photoionization modeling of AGN outflows along with analysis of density diagnostics in order to determine the distances and energetics of observed outflows. The main findings of these analyses are that 1) outflows are often at distances of hundreds to thousands of parsecs from the central supermassive black hole and 2) quasars outflows can be sufficiently powerful to provide feedback in galactic evolution scenarios. We also find in some cases that the recombination timescales of metal ions are long compared with the flux variability timescales. The large distances we find provide a challenge to current outflow models. For example, these outflows cannot be connected with an accretion disk surrounding the supermassive black hole as assumed in some models. Furthermore, the outflows may be out of equilibrium as we find in Mrk 509. In this case, a thorough understanding of time-dependent photoionization effects is necessary. In this thesis, I include early steps toward understanding time-dependent photoionization as well as ionization studies of accretion disk winds. The main results of these theoretical studies is that 1) the appearance of multiple ionization components in an outflow can be an artifact of the incorrect assumption that the outflow is in ionization equilibrium and 2) the shielding gas required in accretion-disk-wind models should have a clear signature in UV spectra, but none has been observed to date.

We acknowledge support from NASA grants HST-AR-12653, HST-GO-12022, HST-AR-13233 and ADAP12-0181, as well as from NSF grant AST 0837880.

To

Kara

and

Isaac

and

Lucas.

Contents

List of Figures

List of Tables

Chapter 1

Introduction

The two largest subdivisions of active galactic nuclei (AGN) are Seyfert galaxies and quasars (Peterson, 1997). Under the unified model (Urry & Padovani, 1995), the nuclei of these galaxies contain accreting, super-massive (10^5 - 10^8 $M_\odot$) black holes and are similar objects, with Seyferts being lower luminosity ($L_{bol} \sim 10^{43}$ – 10^{45} erg/s), lower redshift ($z \lesssim 0.1$) versions of quasars (Crenshaw et al., 2003). Quasars and Seyferts are subdivided into type I and type II by the emission line features found in optical spectra (Khachikyan & Weedman, 1971). Type I AGN show broad emission lines (up to 10^4 km/s) of high ionization species (e.g. C IV, N V, and O VI) with narrow emission lines (several hundred km/s) superimposed on the broad lines while type II AGN show only the narrow lines (Peterson, 1997).

AGN ubiquitously show outflows ($\simeq$ 20–40% of all quasars and $\simeq$ 60% of all Seyfert galaxies; Crenshaw et al. 2003; Hewett & Foltz 2003; Dai et al. 2008), where blueshifted absorption features are attributed to subrelativistic ($\sim 10^4$ km s^{-1}) mass ejection. These outflows are wide, covering 20–60% of the solid angle, thus allowing for efficient interaction with the environment. Narrow absorption lines (NALs) with velocity widths $\lesssim$ 500 km s^{-1} appear

in AGN across the entire range of luminosities, while broad absorption lines (BALs) with velocity widths $\gtrsim 2000$ km s^{-1} appear only in quasars. Whether this indicates that NALs are produced and/or driven by different physical mechanisms than BALs is unknown. The presence of miniBALs, absorption features with velocity widths between NALs and BALs, in some quasar spectra implies a continuum of velocity widths, which indicates similar physics for NALs and BALs.

Due to their large velocity widths, BALs must be connected to the AGN. However, it is less clear in spectra whether NALs detected along the line of sight are connected to the AGN. In a sample of optically bright quasars at redshifts $z = 2$ to $z = 4$, Misawa et al. (2007) find that $\sim 50\%$ contain NAL outflows. Empiracally, NALs are separated into intervening (from systems not physically related to the quasar) and associated absorption lines (AALs) with AALs defined as having widths less than a few hundred km/s and central velocities indicating speeds within 5000 km/s. The frequency per unit velocity of AALs with speeds less than $\sim$5000 km/s increases with decreasing velocity, implying these systems are intrinsic to the quasar (Weymann et al., 1979, 1991; Hamann et al., 2000, 2001). Other indications of the intrinsic nature of an absorption system are time-variability in the troughs and partial coverage of the continuum and/or emission line regions (for others, see Hamann et al. 1997; Barlow et al. 1997).

The potential impact of active galactic nuclei (AGN) on their environment has become widely recognized, including effects on cluster cooling flows [1-26], the growth of super-massive black holes (SMBHs) [27-54], the evolution of their host galaxies [55-81], and the chemical enrichment, entropy and magnetization of the intergalactic medium (IGM) [82-106]. These works (see References, part 2) are only a small representative sample of the rapidly growing field of AGN feedback: Using the energy and mass output of AGN to solve many problems in cosmological structure formation, from the SMBH all the way to a Mpc scale. Even

though relativistic jets are frequently invoked as the main feedback agent, their low mass flux and small opening angle make it hard for narrow jets to couple with their environment (e.g., Omma & Binney 2004; Vernaleo & Reynolds 2006, 2007; Heinz et al. 2006). The wide absorption outflows carry thousands of times more mass flow rate per unit of kinetic power than do relativistic jets, making them a far better agent for AGN feedback (e.g., Ostriker et al. 2010; Ciotti et al. 2010; McCarthy et al. 2010; Soker 2010; Soker & Meiron 2011).

Outflows need kinetic powers that are 0.5% (Hopkins & Elvis, 2010) to 5% (Di Matteo et al., 2005) of the bolometric luminosity to regulate galaxy growth and produce the observed M_{BH}/σ_{bulge} correlation (Ferrarese & Merritt, 2000; Gebhardt et al., 2000). Observations of powerful quasars have revealed outflows that are sufficiently energetic up to kpc scales (e.g., Moe et al. 2009; Borguet et al. 2013). As important as these outflows are to black hole and galactic evolution, we still lack sufficient understanding of their structure, location, and energetics. Nearby AGN provide local analogs illustrating the mechanics, energetics, and chemical enrichment patterns that may play a signicant role in cosmic evolution at high redshift. Large multi-wavelength campaigns aimed at Seyferts have been very successful in broadening our understanding of outflows, and many of these campaigns have recognized the importance of studying variability in order to understand the structure and geometry of outflows. We therefore have spectral coverage over many epochs along with lightcurve monitoring for several AGN.

Photoionization modeling is a key component of determining the physical conditions in outflows. The majority of this thesis involves determining structure, distance, and energetics of AGN outflows through photoionization modeling and analysis of density diagnostics. Usually ionization equilibrium is assumed. Many of the distance determinations for AGN outflows have relied on this assumption (e.g., de Kool et al. 2002; Gabel et al. 2005b; Crenshaw & Kraemer 2007; Korista et al. 2008; Moe et al. 2009; Dunn et al. 2010b; Edmonds et al. 2011;

Borguet et al. 2012). In many of these cases, multi-phase plasma models have been invoked to explain the coexistence of low ionization species (such as Si II) and high ionization species (such as O VI). Due to the very strong kinematic correspondence of high and low ionization lines, this is interpreted as a multi-phase gas with denser clumps embedded in a hotter, lower density medium. We often find the two phases are not in pressure equilibrium and therefore unstable. The timescale for changes in ionic fractions is typically much longer than observed short-term timescales for continuum variations, nullifying the initial assumption of equilibrium. For example, in Mrk 509, we found timescales for ionic fraction changes in C IV $\gtrsim 1$ year for a number density of 10^3 cm^{-3}, while the continuum flux showed variation of $\approx 40\%$ over 40 days.

The structure of this thesis is as follows. In Chapter 2, I first describe our method for photoionization analysis of AGN outflows. Comparison of predicted ionic column densities to measured ones is the key criterion for determining the success of our model. Therefore, I give an overview of our measuring techniques and the grid-model approach we use to compare models to data. In Chapter 3, I discuss density determinations. We mainly use two methods; comparing ionic column densities of excited and ground states of a given ion and analyzing time-variations of absorption features. In each subsection are detailed application of these methods to AGN. Variability is a powerful tool in determining outflow distance and structure. In order to properly interpret the data, we must understand time-dependent photoionization. In Chapter 4, I discuss early steps in understanding non-equilibrium outflows. In Chapter 5, I discuss photoionization modeling of accretion disk winds, a commonly adopted model of AGN outflows, and conclusions are given in Chapter 6.

Chapter 2

Photoionization Modeling

The key features of AGN spectra are due to emission and absorption of photons by different ions of abundant chemical elements such as C IV, N V, and O VI. The relative number of ions for a given element, i.e., the ionization structure of the material, depends on the amount of ionizing radiation emitted by the central source and the distance to the material. By determining the ionization structure of an AGN outflow, we can then determine the distance for a known flux. To determine the ionization structure, we use spectral synthesis codes such as *Cloudy* to numerically solve the photoionization and thermal balance equations. In this chapter, I breifly describe the main ionization equations and how we use *Cloudy* to obtain the physical parameters needed to determine distances and energetics of the outflows.

The abundance of a given element in ionization stage i is given by

$$\frac{dn_i}{dt} = -n_i(I_i + R_{i-1}) + n_{i-1}I_{i-1} + n_{i+1}R_i, \tag{2.1}$$

as a function of the ionization rate per particle, I_i, and the recombination rate per particle

from ionization stage $i+1$ to i, R_i. We have neglected Auger effects, collisional ionization, and charge transfer (e.g., Krolik & Kriss 1995). If the gas at distance r from an ionizing source of monochromatic luminosity L_ν is optically thin, then the ionization rate per particle is given by

$$I_i = \int_{\nu_i}^{\infty} \frac{(L_\nu/h\nu)\sigma_\nu}{4\pi r^2} d\nu, \tag{2.2}$$

where h is Planck's constant and σ_ν is the cross-section for ionization by photons of energy $h\nu$. The recombination rate per particle is given by

$$R_i = \alpha_i(T) n_e. \tag{2.3}$$

The recombination coefficient α depends on the electron temperature T and scales roughly as $T^{-1/2}$ (Osterbrock & Ferland, 2006).

Equation 3.23 forms a set of $n+1$ coupled differential equations for an element with n electrons and $n+1$ ions. In the steady state, these reduce to n equations of the form

$$\frac{n_{i+1}}{n_i} = \frac{I_i}{R_i}. \tag{2.4}$$

Closure of the steady state set of equations is given by $\sum n_i = n_{tot}$, where n_{tot} is the total number density of the element in question. Under these assumptions the level of ionization of the gas in photoionization equilibrium may be characterized by I_i/R_i. In the UV, we typically use the following closely related definition of ionization parameter

$$U = \frac{Q_H}{4\ \pi\ r^2\ n_H}, \tag{2.5}$$

where n_H is the hydrogen number density, and

$$Q_H = \int_{\nu_i}^{\infty} \frac{L_\nu}{h\nu} d\nu \tag{2.6}$$

is the rate of hydrogen ionizing photons emitted by the central source. Therefore, the ionization parameter U is a unitless paramater relating the flux of ionizing photons to the hydrogen number density at the inner face of a spherical outflow. This is the key relationship that allows us to determine distances to AGN outflows.

2.0.1 Measuring Ionic Column Densities

*This sub-section, written mostly by Benoit Borguet, is published in Edmonds et al. (2011) and is reproduced here with permission of AAS.

Our main criterion for the success of a model to fitting the data is how well predicted ionic column densities match the measured ones. Therefore, I briefly describe how we measure ionic column densities before describing our method of photoionization modeling.

A first step in characterizing the physical properties of the absorber is the determinination of ionic column densities associated with the absorption troughs seen in the spectrum. Early studies of intrinsic AGN absorption troughs using UV doublets such as C IV $\lambda\lambda$1549,1551 Å revealed that they rarely follow the expected 1:2 optical depth ratio between the weakest and strongest components of the doublet (e.g. Barlow & Sargent 1997). One interpretation of this observation is that the absorber does not totally cover the emission source (e.g., Hamann et al. 1997; Ganguly et al. 1999; Arav et al. 1999, 2002; Gabel et al. 2003; Arav et al. 2005, 2008). Assuming a partial covering model of a single homogeneous emission source, the residual intensity observed for line j of a given ion as a function of the radial velocity v can

be expressed as:

$$I_j(v) = I_0(v)((1 - C_{ion}(v)) + C_{ion}(v)e^{-\tau_j(v)}) \tag{2.7}$$

where C_{ion} is the fraction of the emission source covered by an absorber having an optical depth τ_j, and I_0 is the unabsorbed emission. While Equation (2.7) is underconstrained for singlets (unless assumptions are made about C_{ion}), multiple lines of a given ion sharing the same lower energy level allow us to derive a velocity dependent solution for both C_{ion} and τ_j by forcing their optical depth ratio $R = \tau_i/\tau_j$ to be identical to the one observed in the laboratory $R = \lambda_i f_i/\lambda_j f_j$. Variations of this technique, including the allowance of different covering fractions for each emission source, have been investigated in the literature (Ganguly et al., 1999; Gabel et al., 2005b). However, the methods described in those papers cannot be applied to doublet lines unless one makes assumptions about the emission source/absorber model (generally assuming the same individual emission source covering for all ions in order to get enough constraints on the model). Note that not properly taking into account this partial covering usually results in an underestimation of the actual column densities (e.g. Arav et al. 1999), thus hampering the interpretation of the physical properties of the intrinsic absorber.

While the partial covering model easily accounts for the departure from an optical depth ratio of 1:2 between the lines of typical doublets, the physical validity of an absorber model displaying a step-function distribution of material accross the emission source is questionable. The fact that we typically find different covering fractions for different ions implies that the actual distribution of absorber material deviates from this simple absorber model. Alternative models in which the emission source is fully covered by a smooth distribution of absorbing material accross its spatial extension were studied in de Kool et al. (2002), Arav et al. (2005), and Arav et al. (2008). Here we use the power law absorber model in which the distribution of optical depth accross the source is characterized by $\tau(x) = \tau_{max}x^a$. In

this case, the normalized residual intensity observed for line j of a given ion as function of the radial velocity v can be expressed as

$$I_j(v) = \int_0^1 e^{-\tau_{max,j}(v)x^{a_{ion}(v)}} dx \tag{2.8}$$

Like Equation (2.7), this equation is underconstrained for singlets (unless assumptions are made about the shape of the absorbing material distribution parametrized by a_{ion}) while a velocity dependent solution can be derived for both a_{ion} and $\tau_{max,j}$ for multiple lines of a given ion sharing the same lower energy level by forcing their optical depth ratio $R = \tau_i/\tau_j$ to be identical to the one observed in the laboratory.

Once an optical depth solution is obtained from either model, the velocity dependent column density is computed using the relation (adapted from Savage & Sembach 1991):

$$N_{ion}(v) = \frac{3.8 \times 10^{14}}{f_j \lambda_j} \langle \tau_j(v) \rangle \ \ (\mathrm{cm}^{-2}\ \mathrm{km}^{-1}\ \mathrm{s}) \tag{2.9}$$

where λ_j is the wavelength of the line (in Å), f_j is its oscillator strength, and $\langle \tau_j(v) \rangle$ is the spatially averaged optical depth across the emission source: For the partial covering model, $\langle \tau_j(v) \rangle = C_{ion}(v)\tau_j(v)$, and for the power law distribution, $\langle \tau_j(v) \rangle = \tau_{max,j}(v)/(a_{ion}(v)+1)$.

2.0.2 The Grid-Model Approach

For determining the distances and energetics of an AGN outflow with known hydrogen number density, the main physical parameters we are interested in are the dimensionless ionization parameter U_H, given in Equation 2.5, and the total hydrogen column density N_H. We use the spectral synthesis code *Cloudy* to simulate the outflow. For a description of *Cloudy*, see Ferland et al. (1998), and for a complete description of the phyical principles

behind the numerical code, see Osterbrock & Ferland (2006). In our method, *Cloudy* takes as input the spectral energy distribution (SED) impinging upon the face of the outflow, the hydrogen number density, the hydrogen column density, and the ionization parameter. We often adjust the chemical abundances as well, but for first runs, the abundances are assumed to be solar. The outflow is typically assumed to be plane-parallel and homogeneous. To determine N_H and U_H, we generate grids of models varying these parameters in 0.1 dex steps (similar to the approach of Arav et al. 2001). For a given SED, $\sim$4500 models are computed to investigate a parameter space with 15 cm^{-2} $\leq$ log N_H $\leq$ 24.5 cm^{-2} and -5 $\leq$ log U_H $\leq$ 2. This range covers the solution space for photoionized AGN outflows. For $U_H \lesssim 10^{-5}$, collisional ionization dominates, while values $\gtrsim 10^2$, lithium-like ions are destroyed. As for total column densities, outflows typically have values of $N_H \gtrsim 10^{18}$ cm^{-2}. If there is evidence of components with column densities less than the 10^{15} cm^{-2} cut-off, models can be run with lower column densities. When $N_H \gtrsim 10^{24}$ cm^{-2}, Thomson scattering dominates. At each point in a grid, we tabulate the predicted column densities of all relavent ions and then compare the measured column densities to those predicted by the models.

A visual representation of the solution space is given in grid-model plots. We plot lines of constant ionic column densities in the $N_H - U_H$ plane. Each line in the plane represents the set of photoionization models that accurately predicts the measured ionic column density for a given ion. Figure 2.1 shows an example of a grid-model plot. If all the lines were to cross at a single point, the values of N_H and U_H for that particular point in the plane would provide a viable model. In reality, the lines should not cross at a single point due to photon statistics, but instead, there should be a solution that falls within one standard deviation of all measured values. To determine the best-fit parameters, we minimize the function

$$\chi^2 = \sum_i \left(\frac{\log N_{i,mod} - \log N_{i,obs}}{\log N_{i,obs} - \log \left(N_{i,obs} \pm \sigma_i \right)} \right)^2 , \tag{2.10}$$

where N_i is the ionic column density, and σ is the uncertainty in the measured value. As shown in Figure 2.1, we allow multiple ionization solutions if the reduced χ^2 is significantly improved.

Figure 2.1 Grid-model plot example. Each line depicts the set of models that predicts the observed ionic column density for the given ion. A single-ionization solution is marked with a cross, and a double-ionization solution is marked with squares. The double-ionization solution is a vast improvement over the single-ionization model.

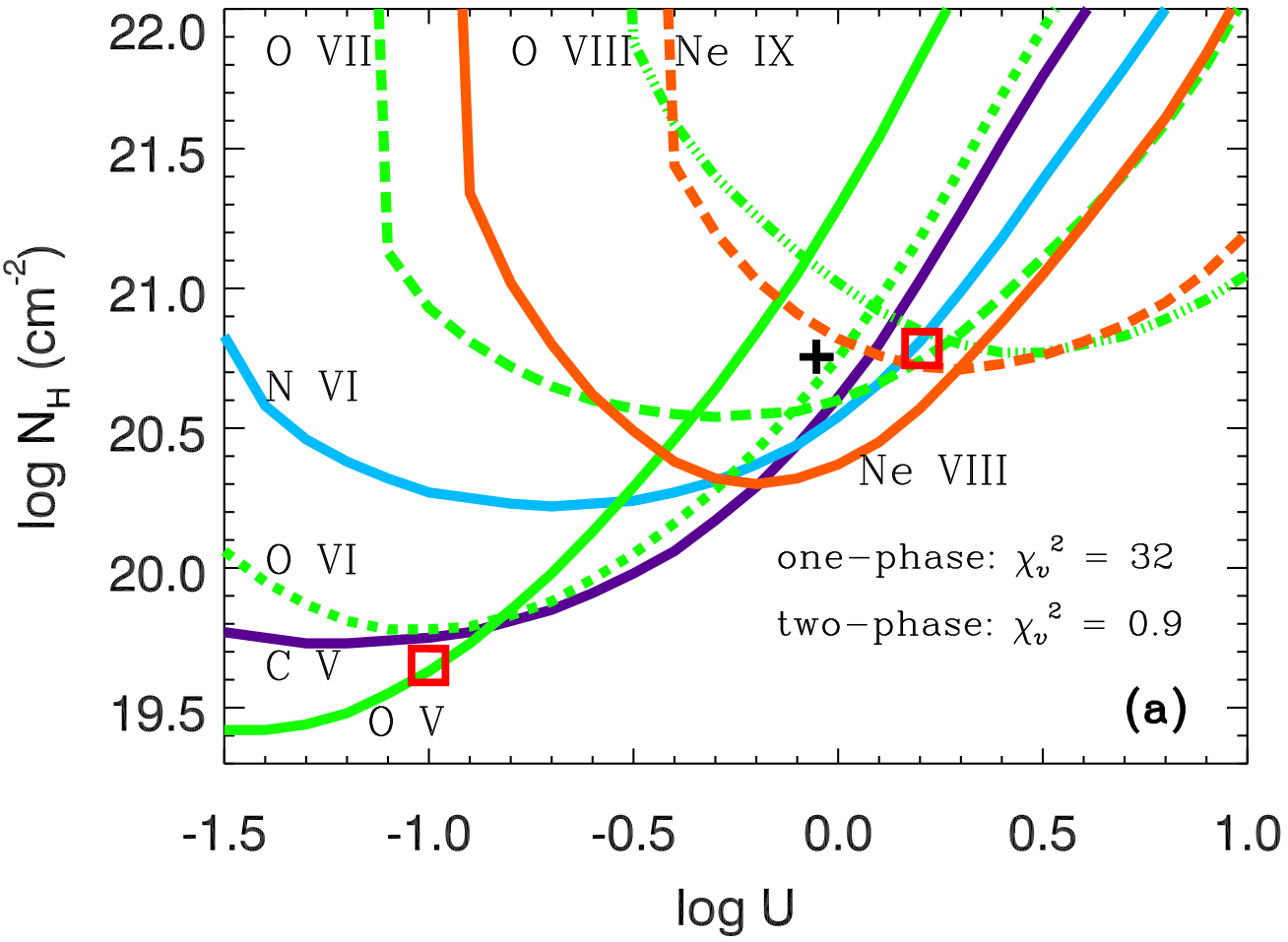

Chapter 3

Determining Distance and Energetics in Observed Outflows

The structure, location, and energetics of AGN outflows are poorly known. We need robust observational constraints on theoretical models of outflows and their interaction with the host galaxies and surrounding IGM. Most Seyfert galaxies and all quasars are observed as unresolved point sources. Therefore, distances must be determined indirectly. As mentioned in the introduction, this is done through photoionization modeling once the hydrogen number density of the outflow is known. There are two main methods for determining the number density; comparison of absorption features from metastable and ground levels of an ion and analysis of time-variability of absorption features. In sections 3.1 and 3.2, I describe the methods for distance determination from metastable levels and time-varibility of troughs, respectively. In each section are detailed descriptions of the application of these methods by our group to AGN.

3.1 Density from Metastable Levels

Metastable levels in ions are long-lived enough to absorb a significant amount of photons emitted from the central source. We see absorption features in AGN spectra due to excited states of C II, C III, O I, O IV, Si II, S IV, and Fe IIas well as others. The critical density for level j of an ion is given by

$$n_c = \frac{\sum_{i<j} A_{ji}}{\sum_{i \neq j} q_{ji}}, \tag{3.1}$$

where A_{ji} gives the transition rate from excited state j to state i (also known as the Einstein A coefficient), and q_{ji} is the collisional de-population rate from state j to state i (Tennyson, 2005). The collisional partners are electrons. Figure 3.1 shows an example of population levels as a function of electron number density, n_e, for C II, Si II, and Fe II. The function is given by balancing the population and de-population rates for the excited state:

$$n_e \, N_i \, q_{ij} = n_e \, N_j \, q_{ji} + N_j \, A_{ji}, \tag{3.2}$$

where N_j is the column density of ions in state j (Osterbrock & Ferland, 2006). The critical density is roughly the electron number density where the ratio of level populations is approximately half the maximum. For n_e much less than n_c, we do not expect to see absorption features from the excited state, and we can place an upper limit on n_e, which corresponds to a lower limit on distance. For n_e much greater than n_c, the ratio of level populations is independent of n_e, and we can place a lower limit on n_e, which gives an upper limit on distance. In the region $n_e \sim n_c$, we can determine a density and, thereby, a distance.

The rest of this section is devoted to detailing the use of this method in several AGN.

Figure 3.1 Electron number density from level population ratios. The lines are ratios of ionic column densities from excited states and ground levels for C II, Si II, and Fe II. The excited states have energies of 63 cm^{-1}, 287 cm^{-1}, and 384 cm^{-1}, respectively.

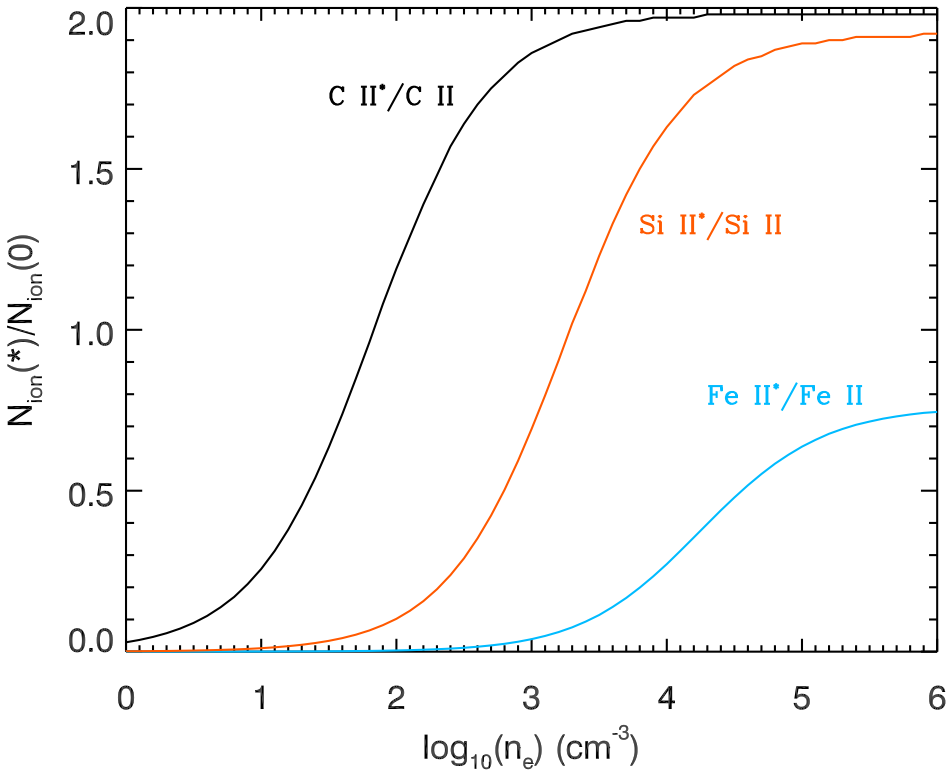

3.1.1 IRAS F04250-5718

*All sections pertaining to IRAS F04250-5718 are published in Edmonds et al. (2011) and are reproduced here with permission of AAS.

Present in the UV spectra of ∼50% of Seyfert I galaxies are strong absorption troughs (Dunn et al., 2007) with full-width at half-maximum ∼ 20 to 400 km s^{-1} (Crenshaw et al., 2003) that are blue-shifted with respect to their emission line counterparts indicating material that is outflowing from the central source. These absorption spectra show lines of C IV $\lambda\lambda$1548,1551; N V $\lambda\lambda$1239,1243; O VI $\lambda\lambda$1032,1038; and H I λ1216 with lower ionization species such as Si IV $\lambda\lambda$1394,1403; and Mg II $\lambda\lambda$2796,2804 seen less often (Crenshaw et al., 1999). Narrow absorption lines (NALs), defined as having FWHM $<$ 500 km s^{-1}, are also found in quasar spectra. For example, Misawa et al. (2007) find intrinsic NALs in spectra of ∼50% of their sample of optically selected quasars at redshifts $z = 2 - 4$. Most studies of NAL quasars have focused on very luminous objects (e.g., Ganguly et al. 1999, 2001; Hamann et al. 2001, 2011; Misawa et al. 2007, 2008). NALs provide important diagnostics of outflows in active galactic nuclei (AGNs). For example, we can learn about chemical abundances in outflows (e.g., Hamann 1997; Gabel et al. 2006; Arav et al. 2007) and provide estimates of their mass flow rates and kinetic luminosities, which are relevent to AGN feedback models (e.g., de Kool et al. 2001; Hamann et al. 2001; Moe et al. 2009; Dunn et al. 2010b,a; Arav et al. 2011).

Most likely, the ionization structure of the outflowing gas is due to photoionization rather than collisional ionization (e.g., Hamann & Ferland 1999). Therefore, photoionization studies are integral to understanding the outflow phenomenon. Computer codes such as Cloudy (Ferland et al., 1998) have been developed to self-consistently solve the ionization and thermal equilibrium equations (Osterbrock & Ferland, 2006). Two parameters of particular interest are the total hydrogen column density (N_H) of the absorbing material and the ion-

ization parameter (U_H), which is proportional to $(R^2 n_H)^{-1}$ where R is the distance to the absorber from the central source, and n_H is the total hydrogen number density. Thus, determining U_H and measuring n_H yield the distance of the outflow. Previous studies have found outflows from AGN on scales of ~ 0.1 pc to tens of kpc from the central source (e.g., Arav et al. 1999; Hamann et al. 2001; Kraemer et al. 2001; Moe et al. 2009; Dunn et al. 2010b).

IRAS F04250-5718 is the first of six objects we observed with the Cosmic Origins Spectrograph (COS, Osterman et al. 2010) onboard the Hubble Space Telescope (HST), as part of our program aiming at determining the cosmological impact of AGN outflows (PID: 11686, PI: Arav). IRAS F04250-5718 was chosen for observation because it shows little or no blending of absorption features, is bright enough to acquire high S/N in several orbits with the high throughput of COS, and has a redshift ($z = 0.104$; Thomas et al. 1998) that allows us to cover Lyα and Lyβ as well as C IV, N V, and O VI doublets with the COS far-ultraviolet (FUV) gratings. Observation of Lyα and Lyβ is necessary for absolute abundance determinations (Arav et al., 2007), which will be presented in a future paper. Connected with our program, simultaneous XMM-Newton data were acquired (Costantini et al., in preparation).

IRAS F04250-5718 is a radio-quiet, low luminosity quasar (with absolute blue magnitude $M_B \approx -24.7$; Véron-Cetty & Véron 2006). Due to the low luminosity and redshift ($z = 0.104$), IRAS F04250-5718 is on the quasar/Seyfert borderline and is spectrally classified as a type 1.5 Seyfert (Véron-Cetty & Véron, 2006). After some confusion due to erroneous positions recorded in some finding charts it was confirmed that the position of this galaxy is consistent with that of the faint blue star LB 1727 (see Halpern et al. 1998; Turner et al. 1999). Observational history: IRAS F04250-5718 was discovered as an X-ray source (1H 0419-577) in the First HEAO survey (Wood et al., 1984) and, later, in the *Einstein* Slew Survey (Elvis et al., 1992) and the *Swift* BAT Survey (Tueller et al., 2008). In a study identifying optical counterparts to HEAO X-ray sources, IRAS F04250-5718 was identified

with a Seyfert galaxy (Brissenden et al., 1987). Observations using the Extreme Ultraviolet Explorer (EUVE) revealed that this object is extremely bright in the 50-180 Å range (Marshall et al., 1995). Most of the work on IRAS F04250-5718 to date has focused on properties of the X-ray spectral energy distribution (e.g., Guainazzi et al. 1998; Turner et al. 1999, 2009; Pounds et al. 2004a,b). Using Suzaku observations, Turner et al. (2009) found evidence of a Compton-thick partial-covering absorber with inferred distances closer to the source than the Broad Line Region (BLR). Data in the far UV were obtained with the Far Ultraviolet Spectroscopic Explorer (FUSE) (Dunn et al., 2007; Wakker & Savage, 2009). Optical spectra were obtained using the Australian National University (ANU) telescope and the Anglo-Australian Telescope (AAT) as well as from the European Southern Observatory (ESO) (Turner et al. 1999 and references therein). To date, no detailed absorption line studies in the UV have been reported.

Photoionization analysis of IRAS F04250

The photoionization and thermal structure of an outflow depends on the spectral energy distribution (SED) incident upon the outflow. A standard SED (hereafter MF87) used in photoionization modeling of AGN was developed in Mathews & Ferland (1987). This SED contains a prominent "big blue bump," which came under scrutiny in later works. For example, Laor et al. (1997) dispute the existence of an X-ray-to-ultraviolet (XUV) bump in AGN based on ROSAT data. However, X-ray data of IRAS F04250-5718 seem to require an XUV bump (Turner et al., 1999). Since this object's SED is unobservable in the UV ionizing region, we analyze models with different XUV bumps. Studies of the SED in the X-ray regime have shown extreme variability (e.g. Guainazzi et al. 1998). Pounds et al. (2004a) showed that the variability could be explained by absorption of a relatively constant SED by cold dense matter. In order to ameliorate this issue, we use the *simultaneous* observations

from HST/COS and XMM-Newton to constrain the SED of IRAS F04250-5718: HST/COS data constrain the SED in the frequency range 2×10^{15} Hz $\lesssim \nu \lesssim 3 \times 10^{15}$ Hz, while data from XMM-Newton (Costantini et al. 2011, in preparation) constrain the high energy portion ($\nu \gtrsim 10^{17}$ Hz) of the SED incident upon the UV absorber. While the FUSE data were taken four years earlier, they agree with the COS data in the overlap region. The co-added COS and FUSE data can be fit with a single power law (see section 3.1) extending the far UV constraints to $\sim$1 Ry.

We consider two families of SEDs in the analysis of IRAS F04250-5718 for a total of three SEDs. Figure 3.2 shows the three SEDs along with the MF87 SED for comparison. For two of our SEDs, we use piecewise power law models. The blue line in Figure 3.2 (hereafter BPL1) is the softest SED we consider physically reasonable given the constraints imposed by the data. It has a spectral break at $\sim$1 Ry, very near the edge of detection in the far UV. The red line in Figure 3.2 (hereafter BPL2) represents the broken power law model that best fits the data while containing an blue-bump that is no more prominent than that in MF87.

For our final SED (hereafter AGN-UVbump), we generate the sum of two continua using the `agn` command in Cloudy. This command produces the continuum given by

$$f_\nu = a\nu^{\alpha_{uv}} \exp\left(\frac{-h\nu}{kT_{BBB}}\right) + b\nu^{\alpha_x}, \tag{3.3}$$

where ν is the frequency, k is Boltzmann's constant, and h is Planck's constant. The spectral index α_{uv} gives the low-energy slope of the optical/UV component, α_x gives the X-ray slope, and T_{BBB} is the temperature of the "big blue bump." The coefficient mutliplying the optical/UV power law component provides an exponential cutoff for energies $\lesssim 0.01$ Ry, and the coefficient multiplying the X-ray power law component is adjusted to produce the optical to X-ray slope (α_{ox}) provided by the user. The X-ray component is set to zero for

Table 3.1 SED Emission Properties

SED	L_{bol} (10^{45} erg/s)	Q_H (10^{55} s^{-1})
MF87	6.4	5.2
AGN-UVbump	8.8	5.0
BPL1	6.6	3.6
BPL2	7.3	5.0

energies ≤ 0.1 Ry and falls off as ν^{-2} for energies $\gtrsim$ 100 keV. Generated by the CLOUDY command `agn 2.8e6 -1.30 -0.80 -0.63` (where the numbers are T_{BBB}, α_{ox}, α_{uv}, and α_x, respectively), the SED AGN-UVbump is similar to the one used by Arav et al. (2007) for Markarian 279 with the main differences being the frequency at which the spectral break of the big blue bump occurs and the hard X-ray excess seen in the XMM-Newton data (also observed in *Suzaku* data by Turner et al. 2009).

Table 3.1 shows the bolometric luminosity (L_{bol}) and the number of hydrogen ionizing photons emitted by the source per second (Q_H) for each SED.

The total hydrogen column density N_H and ionization parameter

$$U_H \equiv \frac{Q_H}{4\pi R^2 n_H c}, \tag{3.4}$$

for the absorber are determined by self-consistent photoionization modeling (where c is the speed of light, Q_H is the rate of hydrogen ionizing photons emitted by the AGN, R is the distance to the absorber from the central source, and n_H is the total hydrogen number density). For this, we use version c08.00 of the spectral synthesis code CLOUDY, last described by Ferland et al. (1998). In these models, we assume solar abundances as given in CLOUDY and a plane-parallel geometry for a gas of constant hydrogen number density. In §3.1.1, we discuss the effects of supersolar metallicities on our results. In determining the ionization

Figure 3.2 SEDs used in the analysis of IRAS F04250-5718. Ionization potentials of H I and O VI are marked with dotted black lines to mark the UV ionizing region of the SEDs. The MF87 SED drops to a minimum of about $10^{43.5}$ erg s^{-1} at E $\approx$ 365 eV.

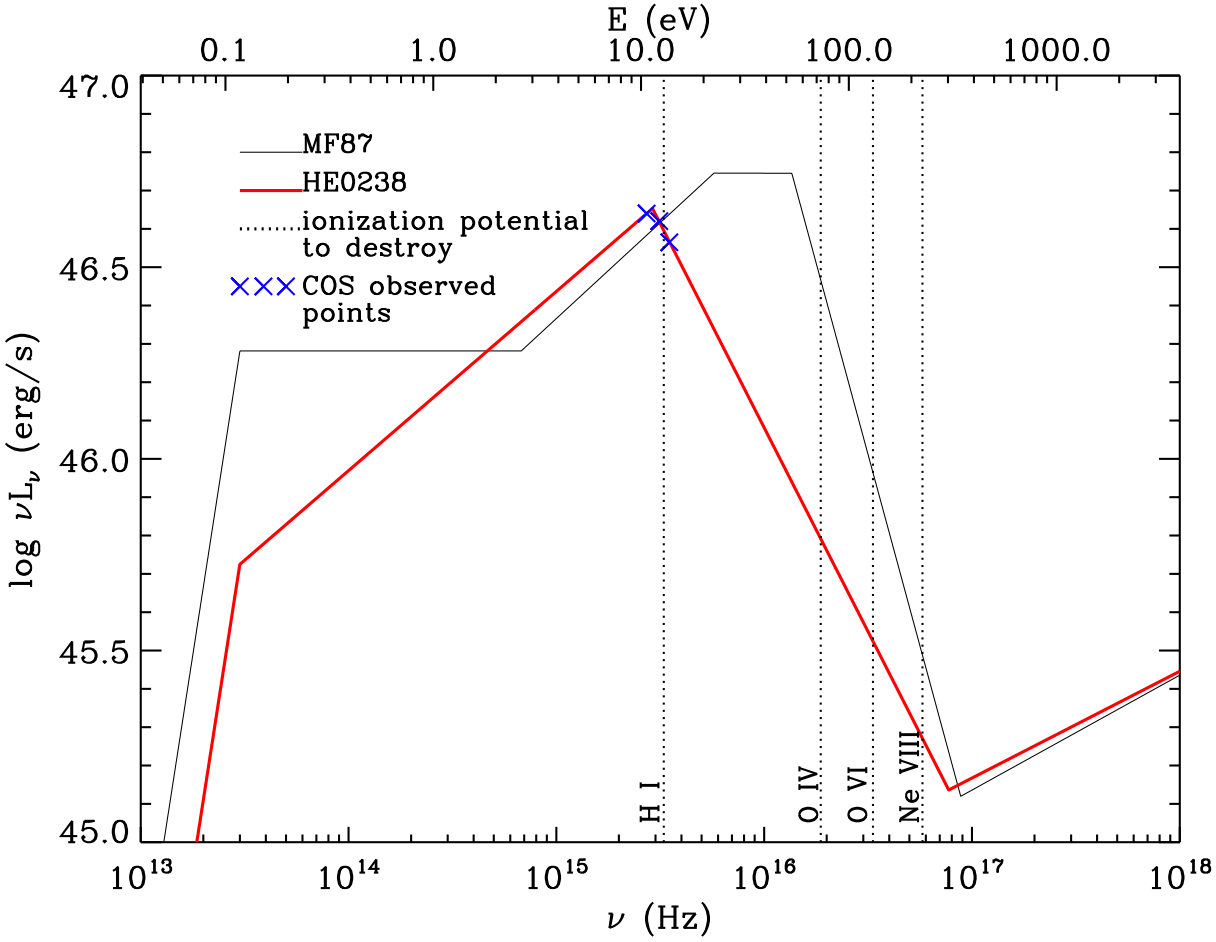

parameter that leads to our distance determination, we assume that the high ionization features (C IV, N V, O VI) come from the same gas as the lower ionization species (C II, Si III, Si IV, S IV). This is supported by the kinematic correspondence for all of the ions in detected in the outflow.

To determine N_H and U_H, we generate grids of models varying these parameters in 0.1 dex steps (similar to the approach of Arav et al. 2001). For a given SED, ~4500 models are computed to investigate a parameter space with 15 $\leq$ log N_H $\leq$ 24.5 and -5 $\leq$ log U_H $\leq$ 2.

Table 3.2 Column densities for component 1 of IRAS F04250-5718

Ion	N_{ion} (AOD)	N_{ion} (PC)	N_{ion} (PL)
H I	442^{+16}_{-15}	532^{+25}_{-20}	1340^{+530}_{-5}
C IV	$79.5^{+1.2}_{-1.2}$	113^{+34}_{-11}	304^{+206}_{-2}
N V	$59.7^{+1.6}_{-1.6}$	$73.2^{+10.4}_{-3.7}$	135^{+43}_{-26}
O VI	634^{+5}_{-5}	1220^{+60}_{-30}	2660^{+1090}_{-0}

Notes. Column densities are given as linear values in units of 10^{12} cm^{-2}. Asymmetrical errors are from photon statistics only and are derived using the technique outlined in Gabel et al. (2005b).

At each point in a grid, we tabulate the predicted column densities of all relavent ions and then compare the measured column densities (given in Tables 3.2 and 3.3) to those predicted by the models. Figures 3.3 and 3.4 show results of this analysis for kinematic components 1 and 2+3 of the outflow, respectively, using the SED AGN-UVbump developed in §3.1.1. In these figures, lines where a linear interpolation of the tabulated N_{ion} matches the measured N_{ion} are plotted in the N_H-U_H plane.

In spectra with absorption features from three or more lines from the same energy level of the same ion, it is possible to test the different absorber models (de Kool et al., 2002; Arav et al., 2005). However, in IRAS F04250-5718, we have no observational constraints on the spatial distribution of absorbing material across the emission source. Therefore, we use the average value of N_{ion} determined by partial covering and power law methods for C IV, N V, ,O VI, H I, and Si IV. For the remaining ions (C II, Si III, and S IV), we have ionic column densities determined by the AOD method only. The fact that all three measurement methods give similar results for the column density of Si IV indicates the AOD method yields a reliable estimate of the actual column density for this ion. We assume this is the case for the other ions with shallower troughs since the line profiles are similar.

Table 3.3 Column densities for component 2+3 of IRAS F04250-5718

Ion	N_{ion} (AOD)	N_{ion} (PC)	N_{ion} (PL)
H I	1730^{+60}_{-50}	2100^{+530}_{-80}	3070^{+990}_{-5}
C II	$11.1^{+1.2}_{-1.3}$	···	···
C IV	$472\ ^{+3}_{-3}$	610^{+25}_{-8}	1160^{+290}_{-7}
N V	637^{+4}_{-4}	834^{+9}_{-8}	1360^{+540}_{-5}
O VI	2700^{+20}_{-20}	3390^{+1040}_{-20}	4170^{+1330}_{-4}
Si III	$2.44^{+0.06}_{-0.06}$	···	···
Si IV	$11.9^{+0.7}_{-0.6}$	$14.1^{+0.6}_{-0.6}$	$15.1^{+0.6}_{-0.6}$
S IV	101^{+4}_{-4}	···	···

Notes. Column densities are given as linear values in units of 10^{12} cm^{-2}. Asymmetrical errors are from photon statistics only and are derived using the technique outlined in Gabel et al. (2005b).

The first kinematic component has only four constraints since none of the low-ionization species are detected there. An approximate solution is determined by visual inspection of the graph and plotted as a solid square in Figure 3.3 at log $U_H \sim$ -1.4 and log $N_H \sim$ 18.9. The error bars span the values of N_H and U_H that yield N_{ion} to within a factor of ~ 2. The parameters are correlated such that increasing U_H requires an increase in N_H resulting in a line of solutions that runs roughly parallel to the curve plotted for N V from the center of the solid square. Table 3.4 details the results of models using different SEDs for component 1 of the outflow.

Figure 3.4 shows the results for kinematic component 2+3 using the SED AGN-UVbump. Four different solutions are given: The solution marked with a plus is approximately equidistant from the C II, C IV, and O VI curves and encompasses all lines to within a factor of ~ 2.5. The crossing point of Si III and Si IV is marked with a square, and the crossing point of C II and C IV is marked with a diamond. Finally, our best by-eye fit to the data is marked with a triangle at log $U_H \sim -1.8$ and log $N_H \sim 19.6$. The "equidistant fit" and the "best by-eye

Table 3.4 Photoionization models for component 1 (-90km s^{-1} $\leq$ v $\leq$ 30 km s^{-1})

Ion	$\log(N_{ion})$ (cm^{-2})	$\log\left(\frac{N_{mod}}{N_{obs}}\right)$		
	observed †	AGN-UVbump	BPL1	BPL2
log U_H	···	-1.40	-1.23	-1.21
log N_H	···	18.85	18.90	18.87
H I	$14.97^{+0.16}_{-0.24}$	+0.02	-0.21	-0.19
C IV	$14.32^{+0.16}_{-0.27}$	-0.21	-0.21	-0.21
N V	$14.02^{+0.11}_{-0.16}$	+0.18	+0.20	+0.20
O VI	$15.29^{+0.13}_{-0.20}$	-0.20	-0.17	-0.19

† Average of column densities derived from the partial covering and power law methods. Uncertainties reflect the range of column densities with the higher given by the power law method and the lower given by the partial covering method.

fit" both provide reasonably good fits to the data. We prefer the best by-eye fit since it obeys the firm lower limit determined by N(O VI) while fitting all of the ions except C II to within a factor of ~ 2.2 as well as improving the fits to N V and Si IV, while giving results for C IV, Si III, S IV, and H I that are similar to those given for the equidistant fit. The disadvantage of the best by-eye fit is that N(C II) is underpredicted by a factor of ~ 5 while for the equidistant fit, N(C II) is underpredicted by a factor of ~ 2.2. Table 3.5 details the results of models using different SEDs for component 2+3 of the outflow.

Solutions for all three SEDs are compared in Figure 3.5. A dashed box encloses the solution space that gives reasonable fits to the data while allowing for changes in SED shape and chemical abundances. Solutions determined by the crossing of C II and C IV in the N_H-U_H plane are omitted because they severely underpredict O VI, for which we have a firm lower limit. Less severe underpredictions may be alleviated by supersolar metallicities, which we investigate in the next section.

Table 3.5 Photoionization models for component 2+3 (-290 km s^{-1} $\leq$ v ≤ -90 km s^{-1})

Ion	$\log(N_{ion})$ (cm^{-2})	$\log\left(\frac{N_{mod}}{N_{obs}}\right)$		
	observed †	AGN-UVbump	BPL1	BPL2
log U_H	···	-1.75	-1.60	-1.57
log N_H	···	19.58	19.59	19.57
H I *	15.41-15.82	+0.31	+0.06	+0.08
C II ‡	$13.05^{+0.04}_{-0.05}$	-0.42	-0.50	-0.67
C IV †	$14.95^{+0.11}_{-0.16}$	+0.29	+0.29	+0.28
N V †	$15.04^{+0.09}_{-0.12}$	+0.02	+0.01	+0.01
O VI †	$15.58^{+0.04}_{-0.05}$	+0.01	-0.01	-0.03
Si III ‡	$12.39^{+0.01}_{-0.01}$	+0.03	+0.04	+0.03
Si IV †	$13.16^{+0.02}_{-0.01}$	+0.05	-0.03	+0.06
S IV ‡	$14.00^{+0.02}_{-0.01}$	-0.10	-0.14	-0.11

* Upper limit determined from the non-detection of a Lyman break in FUSE data. The range of values for H I is shown as a gray strip in Figure 3.4.

‡ Column densities derived from the AOD method. Uncertainties are due to photon statistics only and are thereby underestimated.

† Average of column densities derived from the partial covering and power law methods. Uncertainties reflect the range of column densities with the higher given by the power law method and the lower given by the partial covering method.

Supersolar Metallicity Models

The ionization parameters for the outflow were determined under the assumption of solar abundances. The grids of models support this assumption for kinematic component 1 of the outflow since the metal lines have crossing points very close to the H I line, but kinematic compononent 2+3 shows signs of supersolar metallicities. In particular, the equidistant solution and the best by-eye fit solution both overpredict H I: In Figure 3.4, these solutions lay above the line marking the H I upper limit. In order to investigate the effects of changes in metallicity (Z) on our determination of N_H and U_H, we use the abundances given by Ballero et al. (2008) for $Z/Z_\odot$=4.23 and 6.11. They also list abundances for $Z/Z_\odot$=7.22, but these do not yield a good solution for any of our SEDs. The results are plotted in Figure 3.5. For each SED, there is an increase in U_H of $\sim$0.1 dex and a decrease in N_H of up to $\sim$0.4 dex. We note that the solutions for $Z/Z_\odot$=4.23 were generally better than those for $Z/Z_\odot$=6.11, which underpredicted H I for both of the broken power law SEDs. For the AGN-UVbump SED, the solution found using $Z/Z_\odot$=6.11 is plotted but left out of the box of reasonable solutions since the fit was so poor. The C IV was fit better in the supersolar models than in the solar ones due to a relative increase in abundance of silicon and nitrogen with respect to carbon, but this resulted in an underprediction of C II that is more severe than in the solar models. In fact, for the AGN-UVbump SED, using $Z/Z_\odot$=4.23, all lines are fit to within a factor of ~ 1.1 except for C II whose column density is underpredicted by a factor of ~ 10. We defer the full determination of chemical abundances for the outflow in IRAS F04250-5718 to a future paper.

Figure 3.3 Component 1: Plots of constant N_{ion} in the N_H-U_H plane. The plotted lines trace models whose predicted N_{ion} matches the observed values. The solid black square marks the model that best fits all of the given constraints. The horizontal dashed line at log $N_H = 24$ is the boundary above which an absorber becomes optically thick due to electron scattering. The slanted dashed line is the approximate location of the hydrogen ionization front. The error bars mark solutions that are within a factor of ~ 2 for all ions. N_H and U_H are correlated such that increasing U_H requires an increase in N_H with the line of solutions running roughly parallel to the N V line from the center of the filled square.

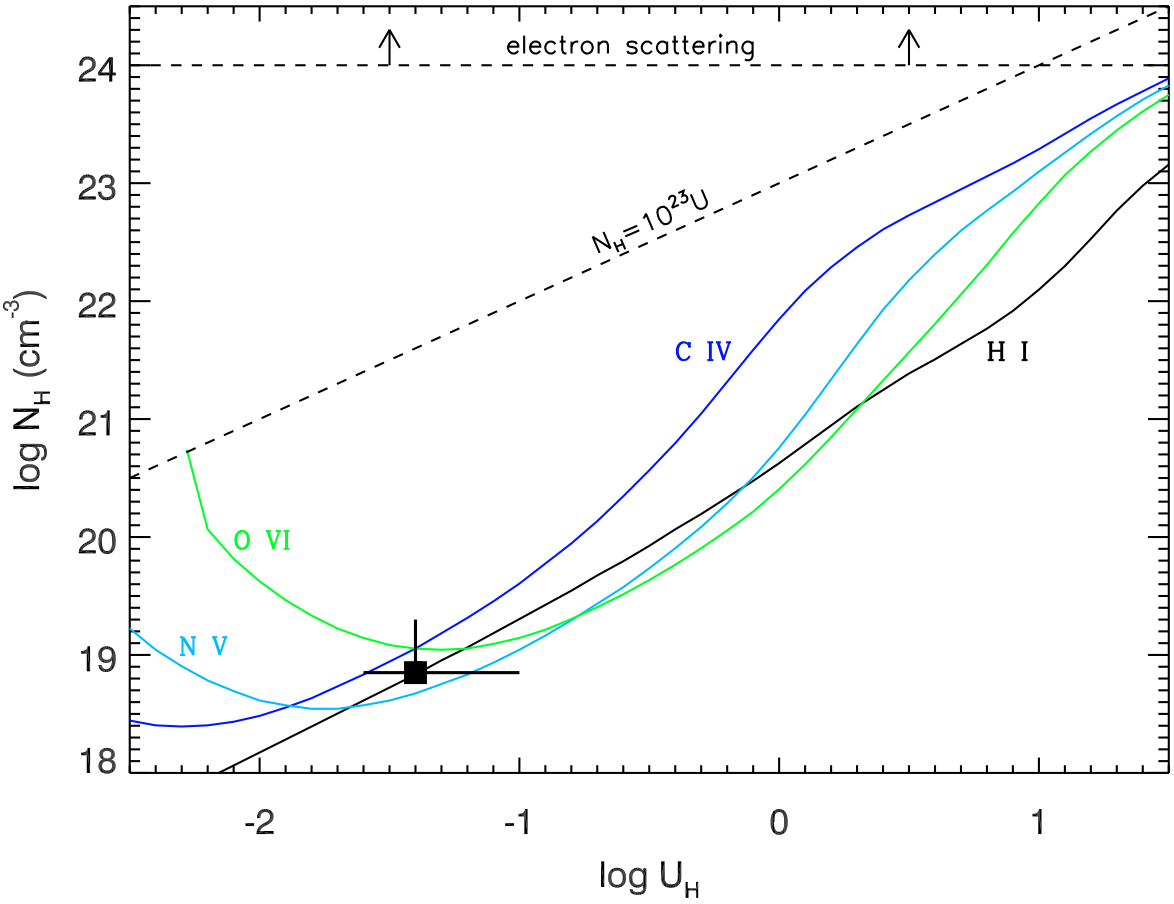

Figure 3.4 Component 2+3: Plots of constant N_{ion} in the N_H-U_H plane. The plotted lines trace models whose predicted N_{ion} matches the observed values. Symbols mark the models that fit certain constraints. The plus is equidistant from C II, C IV, and O VI. The square and diamond mark the crossing points of silicon ions and carbon ions, respectively. The best by-eye fit is marked with a triangle. The lower limit on H I is due to the fact that Lyβ may be saturated, and the upper limit is determined from non-detection of a Lyman break. The shaded band therefore represents values of H I consistent with the data.

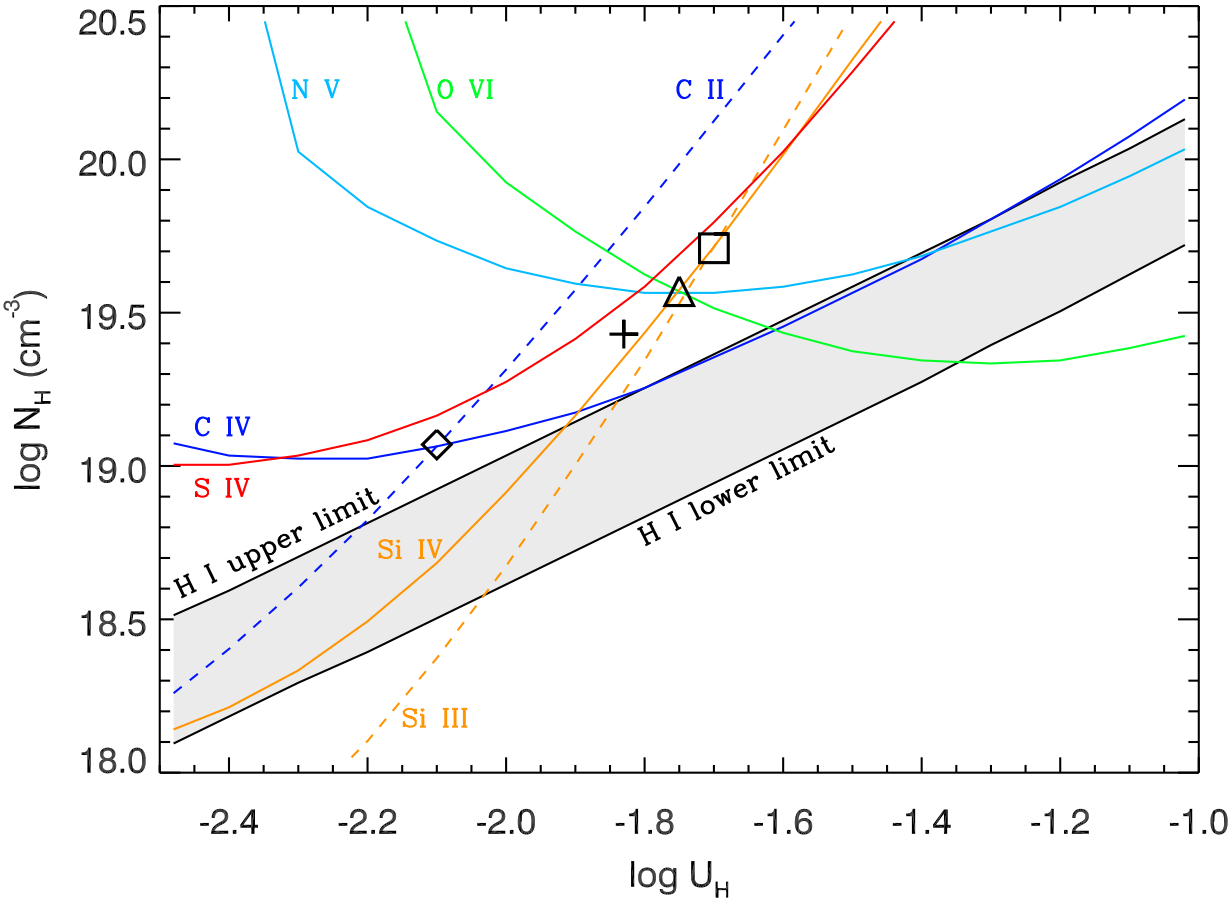

Figure 3.5 Photoionization solutions for component 2+3 of the outflow for different SEDs and metallicities. The colors match those of the SEDs in Figure 3.2 in the online version: Green is the AGN-UVbump SED, blue is BPL1, and red is BPL2. Abundances are solar unless noted otherwise: Solar abundances are from CLOUDY, and supersolar abundances are from Ballero et al. (2008). Only the best by-eye fits are shown for supersolar metalllicites. The dashed box shows the range of plausible solutions.

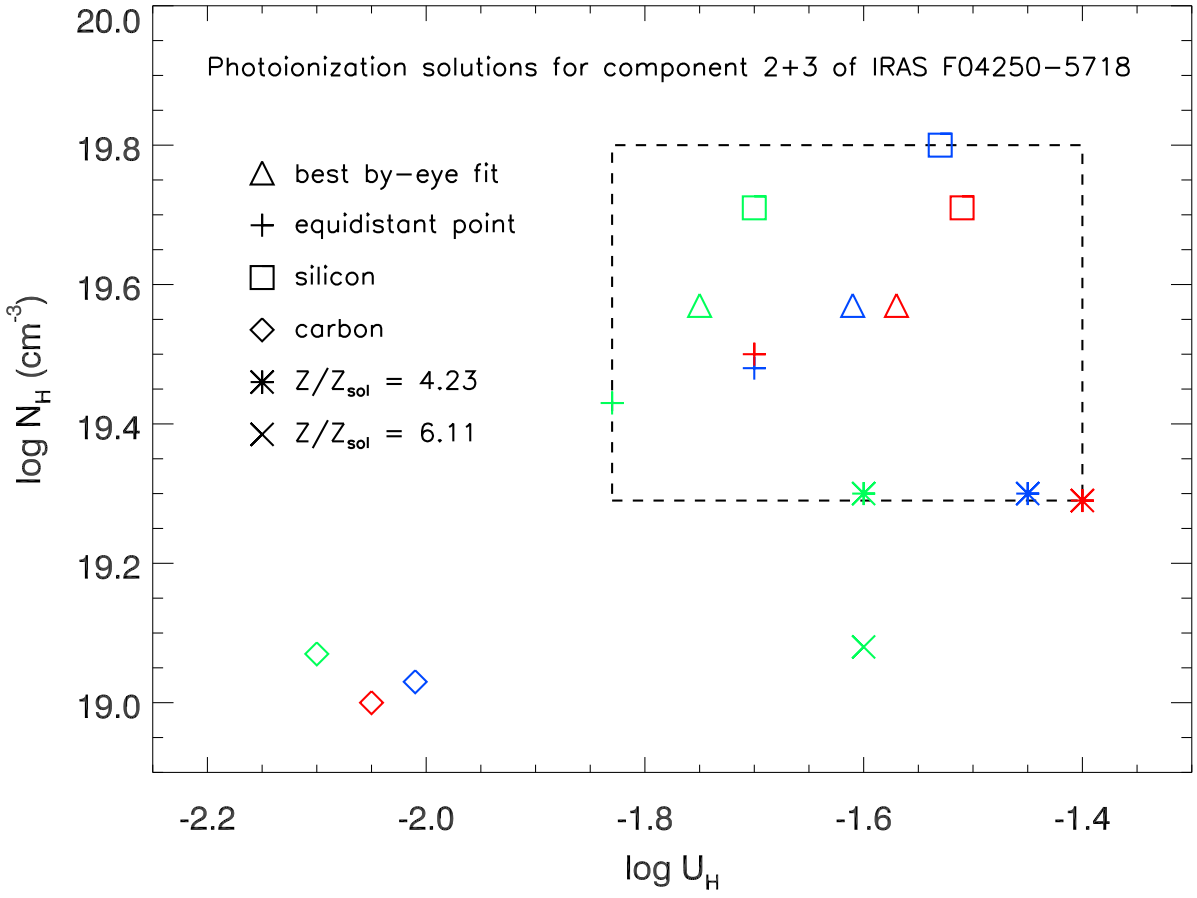

Multiple Ionization Parameter Models

For optically thin models, multiple ions from the same chemical species offer (approximately) metallicity independent solutions for N_H and U_H. In the COS spectrum of IRAS F04250-5718, we have C II, C IV, Si III, and Si IV. The results obtained using just the ratios of $N(\mathrm{C\,II})/N(\mathrm{C\,IV})$ and $N(\mathrm{Si\,III})/N(\mathrm{Si\,IV})$ are shown in Figure 3.5: The diamonds mark the results from carbon and the squares mark the results from silicon. While the values of N_H agree very well, there is a discrepancy in the determination of U_H of ~ 0.4 dex. Furthermore, the ratio $N(\mathrm{C\,IV})/N(\mathrm{C\,II})$ is substantially overpredicted by the models that give reasonable fits to the other ions. We therefore investigate the possibility of two ionization parameters improving on the photoionization solutions for kinematic component 2+3.

For all three SEDs, the by-eye best fits (marked with triangles in Figure 3.5) underpredict the column densities of C II and Si III. By choosing a second ionization parameter that is near the crossing point ($\log U_H \sim -3.5$) of C II and Si III in the N_H-U_H plane, we improve the fits to these two low ionization ions while leaving essentially unchanged the predicted column densities of the other ions when values from the two models are summed. However, low ionization parameter models predict a substantial amount of Si II, which we do not detect in the data. Using an upper limit of $\log N(\mathrm{Si\,II}) \sim 11.9$ cm^{-2}, the two ionization parameter solutions overpredict $N(\mathrm{Si\,II})$ by ~ 0.6 dex. We conclude that the two ionization parameter does not significantly improve our results, simply trading the underprediction of $N(\mathrm{C\,II})$ for the overprediction of $N(\mathrm{Si\,II})$.

Absorber Distance and Energetics

The distance to the absorber can be computed from the ionization parameter (see Equation (3.22)) if the total hydrogen number density n_H is known. To estimate n_H in kinematic component 3 (the high velocity component) we consider the ratio of populations of the first excited metastable and ground levels of C II. The rebinned line profiles of C II λ1335 and C II* λ1336 are shown in Figure 3.6. Integrating the flux in the region where a C II* trough should be according to the detected C II trough yields a column density for C II* of $2.81^{+1.31}_{-1.07} \times 10^{12}$ cm^{-2} where the errors are 1-σ photon statistics. Due to non-detection of the excited state of C II, we place a conservative upper limit on the column density of C II* of 6.74×10^{12} cm^{-2} by assuming the noise could hide up to a 3-σ detection. Comparing collisional excitation models with the ratio of the column density measurement of C II ($11.1 \pm 1.3 \times 10^{12}$ cm^{-2}) and the upper limit on the column density of C II* ($\lesssim 6.74 \times 10^{12}$ cm^{-2}), we place an upper limit on the free electron number density $n_e \lesssim$ 30 cm^{-3} (see Figure 3.7). Since our photoionization modeling implies we are within the He III region, $n_e \approx 1.2 n_H$. In order to place robust lower limits on the distance, mass flow rate, and kinetic luminosity of the absorber, we adopt the model with the SED BPL2 and a metallicity of $Z = 4.23$ which yields the maximum U_H ($10^{-1.4}$) and minimum N_H ($10^{19.3}$) of all our models. These results imply a distance of

$$R = \left(\frac{Q_H}{4\pi c U n_H} \right)^{1/2} \gtrsim 3 \text{ kpc} \tag{3.5}$$

for kinematic component 2+3. We note that the data hint at a detection of C II*. Since the C II* trough that appears in Figure 3.6 is too shallow to clearly distinguish from the noise, we do not claim we have a measurement of the column density of C II*, but state that the lower limit on the distance may be an estimation of the actual distance. We cannot

determine the distance to kinematic component 1, since we have no density diagnostics for this component.

In order to estimate the mass, mass flow rate, and kinetic luminosity of the outflow, we must assume a geometry. For a full discussion of the geometry used here, see Arav et al. (2011). Assuming that the outflow has the geometry of a thin, partially-filled shell, the mass is given by

$$M_{out} = 4\pi\mu m_p R^2 N_H \Omega \gtrsim 2 \times 10^7 \Omega_{0.5} M_\odot, \tag{3.6}$$

where $\mu = 1.4$ is the mean atomic mass per proton, m_p is the mass of the proton, and Ω is the covering fraction of the outflow as seen from the central source. We adopt the value $\Omega = 0.5$ due to the fact that outflows are seen in about 50% of observed Seyfert galaxies (Dunn et al., 2007) and the luminosity of IRAS F04250-5718 is just above that of a Seyfert galaxy. A comprehensive discussion of covering fraction for quasar outflows is given in Dunn et al. (2010b). In order to reflect the uncertainty in Ω, we provide our results in units of $\Omega_{0.5} = \Omega/0.5$. The average mass flow rate is just the total mass divided by the dynamical timescale R/v:

$$\dot{M}_{out} = 4\pi\mu m_p R N_H v \Omega \gtrsim 1\ \Omega_{0.5}\ M_\odot \mathrm{yr}^{-1}. \tag{3.7}$$

This value is similar to the mass accretion rate we find under the assumption that the black hole is accreting mass at the Eddington rate (Salpeter, 1964):

$$\dot{M}_{acc} = \frac{L_{bol}}{\epsilon c^2} \sim 2\ M_\odot \mathrm{yr}^{-1}, \tag{3.8}$$

where we have assumed an efficiency $\epsilon = 0.1$. Finally, the kinetic luminosity is given by

$$\dot{E}_k = \frac{\dot{M}_{out} v^2}{2} \gtrsim 1 \times 10^{40}\ \Omega_{0.5}\ \mathrm{erg\ s}^{-1}. \tag{3.9}$$

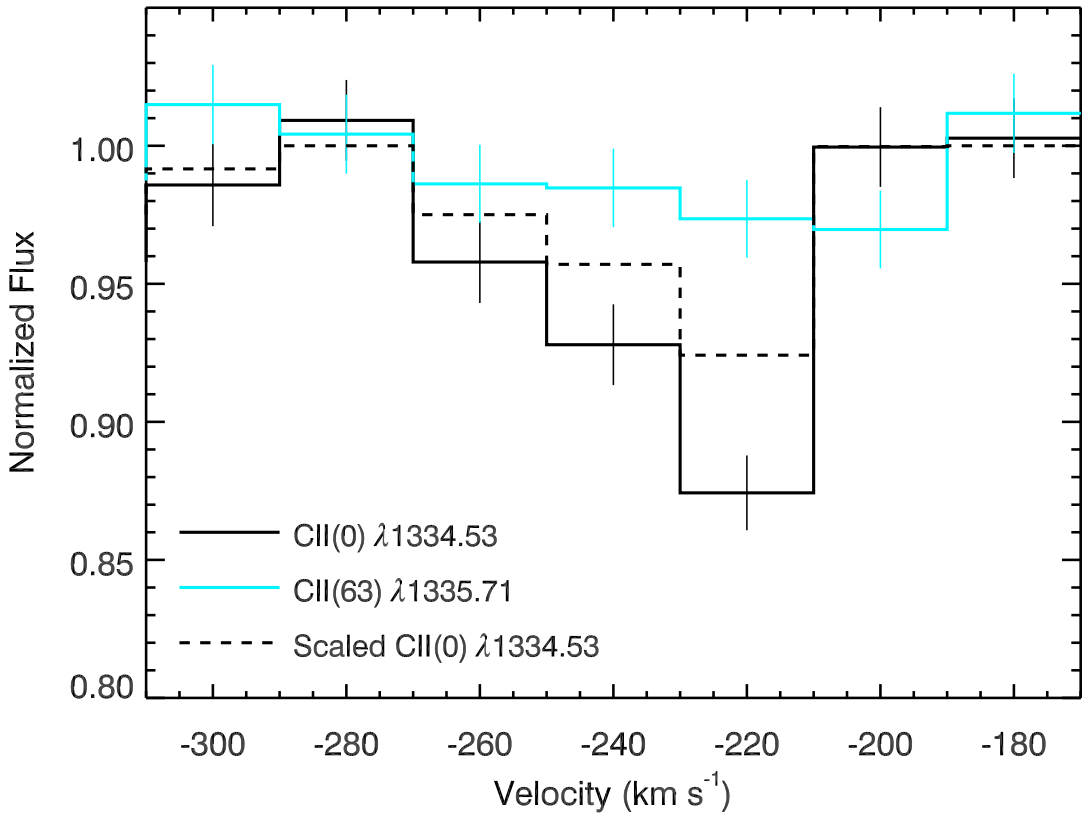

Figure 3.6 Line profiles for C II and C II* rebinned to 20 km/s. We place an upper limit on C II* by assuming the noise could hide up to a 3-σ detection. The dashed line shows the C II trough scaled to the 3-σ noise in the region where C II* would be.

Given that the bolometric luminosity is $L_{bol} \sim 9{\times}10^{45}$ erg s^{-1}, this outflow is not energetically significant in AGN feedback scenarios, which typically require $\dot{E}_k$ to be a few percent of L_{bol} (e.g., Scannapieco & Oh 2004). The mass flow rate is also rather small for the purpose of chemically enriching the environment. Assuming a duty cycle of 10^8 for the active phase of this AGN, Hellman and Arav (2011, in preparation) find that a mass flow rate of 1 solar mass per year is only enough to enrich a small galactic halo of $\sim 10^{10} M_{\odot}$ to the observed Intra-Cluster values, or alternatively 1 Mpc^3 of the Inter-Galactic Medium.

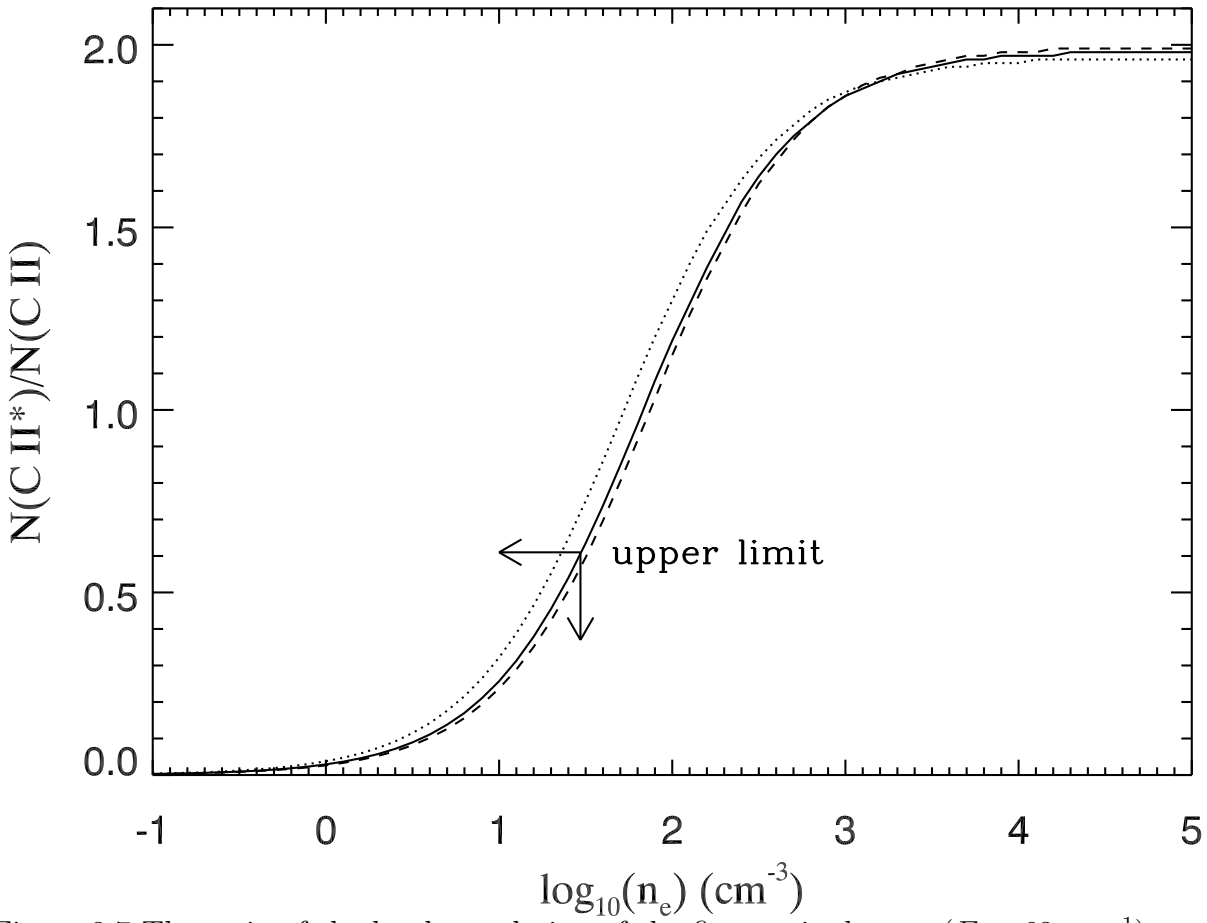

Figure 3.7 The ratio of the level population of the first excited state ($E = 63$ cm^{-1}) to the level population of the ground state for C II versus electron number density (n_e) for T = 10000 K (dotted line), T = 15000 K (solid line), and T = 30000 K (dashed line). Non-detection of C II* implies a level population ratio of $\sim 0.25 \pm 0.12$. For a conservative upper limit, we use the 3-σ value of 0.61 yielding $n_e < 30$ cm^{-3}.

Discussion of results for IRAS F04250

While it is clear that outflows at distances of $\lesssim$ 10 pc and/or with velocities $\gtrsim$ 500 km s^{-1} (Martin, 2005) are AGN driven, outflows at distances $\gtrsim$ 1 kpc with lower velocities, such as the one we find in IRAS F04250-5718, are difficult to distinguish from galactic winds. Galactic winds are ubiquitous in starburst galaxies: Studies show $\gtrsim$ 75% of ultra-luminous infrared galaxies (ULIRGs) have winds (Veilleux et al. 2005 and references therein). An optical study of edge-on Seyfert galaxies by Colbert et al. (1996) revealed large-scale outflows in $\sim$25% of these AGN. However, since evidence of starburst activity is found in about half of optically selected Seyfert 2 galaxies (González Delgado & Pérez, 2000), it is difficult to determine whether the galactic-scale outflows in Seyferts are driven by the AGN or starbursts. In a sample of ultra-luminous infra-red galaxies (ULIRGs) containing both an AGN and a high star formation rate, Rupke et al. (2005) found that the velocity distributions in outflows observed in Seyfert 2 galaxies differed from those found in starburst galaxies with no observable AGN activity, suggesting the AGNs play a role in driving the galactic-scale outflows in these objects.

Much of the work on galactic winds has focused on optical emission lines produced by the warm gas (e.g., Colbert et al. 1996; Lehnert & Heckman 1996), and X-ray emission lines produced by the hot gas (e.g., Dahlem et al. 1998). Emission line techniques favor edge-on galaxies where it is easier to separate the wind emission from background emission. Complementary studies of absorption lines (e.g., Heckman et al. 2000; Martin 2005; Martin & Bouché 2009) favor face-on galaxies. Absorption line studies of galactic winds afford the advantage that the whole range of gas densities in outflows can be probed unlike emission line studies where the densest gases are favored (Heckman et al., 2000). Much of this work has relied on Na I $\lambda\lambda$5892,5898 lines and find they do not completely cover the source. Martin &

Bouché (2009) found they could better constrain the kinematics of the outflow using Mg II $\lambda\lambda$2796,2803 since the absorption features are well separated allowing for better analysis than the heavily blended Na I doublet.

The distance and speed we find for kinematic component 2+3 is typical for a galactic wind (Veilleux et al., 2005). We are unable to determine whether this outflow is AGN or starburst driven, but partial-covering of the emission sources implies the outflow is intrinsic to the host galaxy so photoionization of the outflow is likely dominated by AGN emission. In this case, regardless of outflow's origin, photoionization analysis, along with the upper limit on the electron number density provided by a detection of C II with no detection of C II*, yields a lower limit on distance to the absorber from the central source.

Summary of results for IRAS F04250

The HST/COS spectrum of the low luminosity quasar IRAS F04250-5718 reveals an outflow with both high and low ionization species. The lines are narrow (FWHM $\lesssim 200$ km s^{-1}), and similar redshifts for corresponding emission and absorption features implies the outlflow is intrinsic to the AGN. Further evidence of the intrinsic nature of this outflow is partial covering of the emission source evident in C IV, N V, O VI, and H I.

Using the measured column density of C II along with an upper limit on the column density of C II*, we found a conservative upper limit on the electron number density in the outflow of ~ 30 cm^{-3}. Photoionization modeling yielded a range in ionization parameter $\log U_H \sim -1.8 \pm 0.2$ and total hydrogen column density $\log N_H \sim 19.55 \pm 0.25$ cm^{-2}. Using model assumptions that minimize the distance to the outflow, we determined a conservative lower limit of $R \gtrsim 3$ kpc. Assuming a thin-shell geometry, lower limits on the mass flow rate and kinetic luminosity were found to be $\gtrsim 1\ M_{\odot}$yr^{-1} and $\gtrsim 1 \times 10^{40}$ erg s^{-1}, respectively.

In determining limits on the distance, mass flow rate, and kinetic luminosity of the outflow, we investigated the effects on our results of changing the SED incident upon the absorber and the metallicity of the gas as well as differences in column density determinations when different absorber models (i.e. partial-covering versus power-law models) were assumed. The ionization parameters found for the three different SEDs are within ~ 0.2 dex of each other, while increasing the metallicity resulted in ionization parameters ~ 0.2 dex higher for each SED and lowered N_H by ~ 0.3 dex from the best-fit solar models. Changing the SED had little effect on the total hydrogen column density, while differences in the absorber model had little effect on ionization parameter and changed N_H by < 0.1 dex.

3.1.2 IRAS F22456-5125

*All sections pertaining to IRAS F22456-5125 are published in Borguet et al. (2012) and are reproduced here with permission of AAS.

IRAS F22456-5125 is the second of six objects we observed with the Cosmic Origins Spectrograph (COS, Osterman et al. 2010) onboard the Hubble Space Telescope (HST), as part of our program aiming at determining the cosmological impact of AGN outflows (PID: 11686, PI: Arav). IRAS F224565125 (z = 0.1016; Dunn et al. 2010b) is a luminous Seyfert I galaxy. With a bolometric luminosity of Lbol = 1045.6 erg s1, this object is at the borderline between Seyfert galaxies and quasars, defined to be 1012 L, where L is the luminosity of the Sun (Soifer et al. 1987).

In Table 3.6, we provide ionic column density measurements for the different kinematic components identified in the HST/COS spectrum. We find absorption features from high ionization species, C iv, N v, O vi, Si iv, and S iv, and low ionization species, Si ii, Si iii, C ii. Absorption features from metastable levels of Si ii and C ii are observed in two kinematic components allowing us to constrain the denisties, and thereby the distances. Previous analysis of spectra obtained from the Far Ultraviolet Spectroscopic Explorer (FUSE) was published in Dunn et al. (2010b). Comparing FUSE spectra from different epochs, they determined a lower limit of 20 kpc from timescale arguments. Here, we use metastable levels as an independent distance determination using high signal-to-noise spectra with more constraints than were available from the FUSE data.

Table 3.6 Computed Column Densities for IRAS F22456-5125

Trough	v_i (km s^{-1})	Ion	AOD[a] (10^{12} cm^{-2})	PC[a] (10^{12} cm^{-2})	PL[a] (10^{12} cm^{-2})	Adopted[e] (10^{12} cm^{-2})
T1	−800	H I	$73.9^{+0.4}_{-0.4}$	< 900[b]	···	$\in [73.5, 900]$
		C IV	$20.9^{+1.1}_{-1.0}$	···	···	$20.9^{+1.1}_{-1.0}$
		N V	$13.9^{+1.6}_{-1.6}$	$18.1^{+1.8}_{-1.6}$	$20.2^{+1.6}_{-1.2}$	$18.1^{+3.7}_{-1.6}$
		O VI	474^{+9}_{-9}	745^{+137}_{-28}	···	745^{+137}_{-28}
		Si III	$< 0.32^{+0.04}_{-0.04}$	···	···	< 0.36
T2	−610	H I	436^{+56}_{-1}	4400^{+660b}_{-660}	···	$\in [9400, 15800]$[f]
		C II	$51.0^{+2.4}_{-2.2}$	$59.7^{+3.3c}_{-2.9}$	···	> 48.8
		C II*	$43.2^{+2.3}_{-2.1}$	$49.5^{+3.2c}_{-2.8}$	···	$\gtrsim 41.1$
		C IV	251^{+27}_{-5}	···	···	> 251
		N V	$109^{+2.6}_{-2.5}$	118^{+15}_{-2}	$142^{+6.4}_{-3.4}$	$118^{+30.4}_{-2}$
		O VI	604^{+11}_{-10}	816^{+127}_{-28}	1199^{+272}_{-11}	816^{+655}_{-28}
		Si II	$10.5^{+0.6}_{-0.6}$	$13.7^{+1.2}_{-0.9}$	$33.3^{+3.5}_{-2.8}$	$13.7^{+23.1}_{-0.9}$
		Si II*	$1.04^{+0.13}_{-0.12}$	$1.18^{+0.18}_{-0.15}$	$1.59^{+0.20}_{-0.17}$	$1.18^{+0.61}_{-0.15}$
		Si III	$> 9.24^{+0.16}_{-0.15}$	···	···	> 9.08
		Si IV	$36.3^{+0.2}_{-0.2}$	$49.4^{+3.7}_{-2.6}$	···	> 46.8
		S IV	$54.0^{+4.5}_{-4.5}$	···	···	$\gtrsim 49.5$
T3	−440	H I	275^{+2}_{-2}	4230^{+790b}_{-790}	···	4230^{+790}_{-790}
		C II	$19.9^{+2.4}_{-2.0}$	···	···	> 17.9
		C II*	$7.66^{+1.55}_{-1.27}$	···	···	> 6.39
		C IV	301^{+5}_{-5}	336^{+8}_{-6}	432^{+73}_{-8}	336^{+169}_{-6}
		N V	143^{+3}_{-3}	167^{+78}_{-5}	···	167^{+78}_{-5}
		O VI	552^{+11}_{-9}	644^{+17}_{-13}	···	644^{+17}_{-13}
		Si II	< 0.66	···	···	< 0.66
		Si III	$3.88^{+0.09}_{-0.08}$	···	···	> 3.80
		Si IV	$13.2^{+1.1}_{-1.0}$	$15.9^{+1.8}_{-1.0}$	$17.3^{+1.5}_{-1.0}$	$15.9^{+2.9}_{-1.0}$
		S IV	< 24.2	···	···	< 24.2
T4	−320	H I	$87.0^{+0.4}_{-0.4}$	550^{+180b}_{-180}	···	550^{+180}_{-180}
		C IV	$62.7^{+2.0}_{-1.9}$	···	···	$62.7^{+2.0}_{-1.9}$
		N V	$46.0^{+2.2}_{-2.1}$	$57.5^{+4.2}_{-2.8}$	$67.9^{+4.8}_{-3.6}$	$57.5^{+15.2}_{-2.8}$
		O VI	335^{+7}_{-7}	400^{+10}_{-8}	···	400^{+10}_{-8}
T5B	−130	H I	399^{+50}_{-1}	6010^{+1200b}_{-1200}	···	6010^{+1200}_{-1200}
		C IV	795^{+104}_{-11}	···	···	> 784
		N V	935^{+80}_{-14}	1035^{+137}_{-14}	1469^{+284}_{-7}	1035^{+718}_{-14}
		O VI	$> 2608_{-22}$	···	···	> 2586
		Si III	$1.78^{+0.08}_{-0.08}$	···	···	> 1.70
		Si IV	$8.49^{+1.13}_{-1.01}$	$13.7^{+11.7}_{-1.9}$	···	$13.7^{+11.7}_{-1.9}$
T5A	−40	H I	$88.2^{+0.5}_{-0.5}$	6010^{+1200d}_{-1200}	···	$\in [87.7, 7210]$
		C IV	$97.4^{+2.4}_{-2.3}$	···	···	> 95.1
		N V	$34.7^{+1.8}_{-1.7}$	$36.7^{+1.3}_{-1.3}$	$40.2^{+1.1}_{-1.1}$	$36.7^{+4.6}_{-1.3}$
		O VI	$> 109_{-4}$	···	···	> 105
		Si III	$2.25^{+0.06}_{-0.06}$	···	···	> 2.19
		S IV	$5.55^{+0.72}_{-0.69}$	$13.7^{+176.8}_{-2.6}$	···	> 13.7

Notes. Table provided by Benoit Borguet and published in Borguet et al. (2012). Reproduced with permission of AAS.

[a] The integrated column densities for the three absorber models. The quoted error arises from photon statistics only and is computed using the technique outlined in Gabel et al. (2005a).

[b] Estimates from Dunn et al. (2010b).

[c] Using the covering solution of Si IV(see the text).

[d] Dunn et al. (2010b) do not make the distinction between the two sub-components in trough T5, so we report an identical PC value in the shallower trough T5A to be considered as a conservative upper limit since the bulk of the column density is coming from T5B.

[e] Adopted values for the photoionization study (see the text).

[f] The lower is fixed by the detection of Ly 10 associated with that component (see the text), and the upper limit is given by the absence of an H I bound-free edge.

Photoionization analysis of the absorbers

In order to derive the physical properties of each kinematic component of the outflow, we solve the ionization equilibrium equations using version c08.00 of the spectral synthesis code Cloudy (last described by Ferland et al. 1998). We model each absorber by a plane-parallel slab of gas of constant hydrogen number density (n_H) and assume solar elemental abundances as given in Cloudy. The spectral energy distribution (SED) we use was described in Dunn et al. (2010a). Using the grid-model approach described in Edmonds et al. (2011), we find a combination of total hydrogen column density (N_H) and ionization parameter given by

$$U_H = \frac{Q_H}{4\pi R^2 n_H c} \tag{3.10}$$

(where Q_H is the rate of hydrogen ionizing photons, R is the distance from the central source to the absorber, c is the speed of light and n_H is the total hydrogen number density) that best reproduces the observed ionic column densities reported in Table 3.6.

The COS observations show a wealth of absorption lines compared to the earlier FUSE observations discussed in Dunn et al. (2010a). This allows us to derive more accurate physical properties of the absorbing clouds associated with the UV outflow. In the following subsections, we describe the photoionization solution derived for each kinematic component. The physical properties of the absorber do not appear to change between the FUSE and COS epochs. Therefore, we use the column densities of H I and C III derived in Dunn et al. (2010a) from FUSE data.

Troughs $T2$ and $T3$

The physical parameters of component $T2$ are constrained by ten ionic column densities, eight from COS data along with H I and C III from FUSE data. The ions span from low-ionization species such as C II and Si II to high-ionization species such as N V and O VI. A plot of the results for a grid of photoionization models for trough T2 is presented in Figure 3.8. The least-squares single-ionization parameter solution is marked with a square in the $N_H - U_H$ plane, and predicted values for ionic column densities are given in Table 3.7. The Si II and C II column densities predicted by that model are underestimating the observed column densities by more than an order of magnitude and almost two order of magnitude for Si II. Due to the poor fit of this model to the data, we use a two-ionization component model, which is depicted by diamonds in Figure 3.8. All of the ions from the COS data are fit well with the two-component model, while H I is over-predicted a factor of ~ 3, indicating super-solar metallicity for the plasma. In order to investigate the effects of changes in metallicity (Z) on our determination of N_H and U_H, we use the abundances given by Ballero et al. (2008) for $Z/Z_\odot = 4.23$ and 6.11. We find U_H changes by less than a factor of ~ 2, and N_H decreases by a factor of ~ 4 for both sets of abundances. Full determination of the chemical abundances for the outflow in IRAS F22456-5125 is deferred to a future paper.

For component $T3$, we have column density measurements for seven ions the COS spectrum, along with H I and C III from FUSE data and an upper limit on Si II due to non-detection of the stronger lines in the COS spectrum. A grid-model for trough $T3$ is plotted in Figure 3.9. A single-ionization parameter solution is marked with a square in the $N_H - U_H$ plane. This solution fits all the lines within a factor of ~ 3 (see Table 3.8). An improvement to the fit for most lines is provided by the two-ionization parameter solution marked with diamonds in Figure 3.9, with the exceptions being an over-prediction of Si II by a factor $\gtrsim 4$ (see

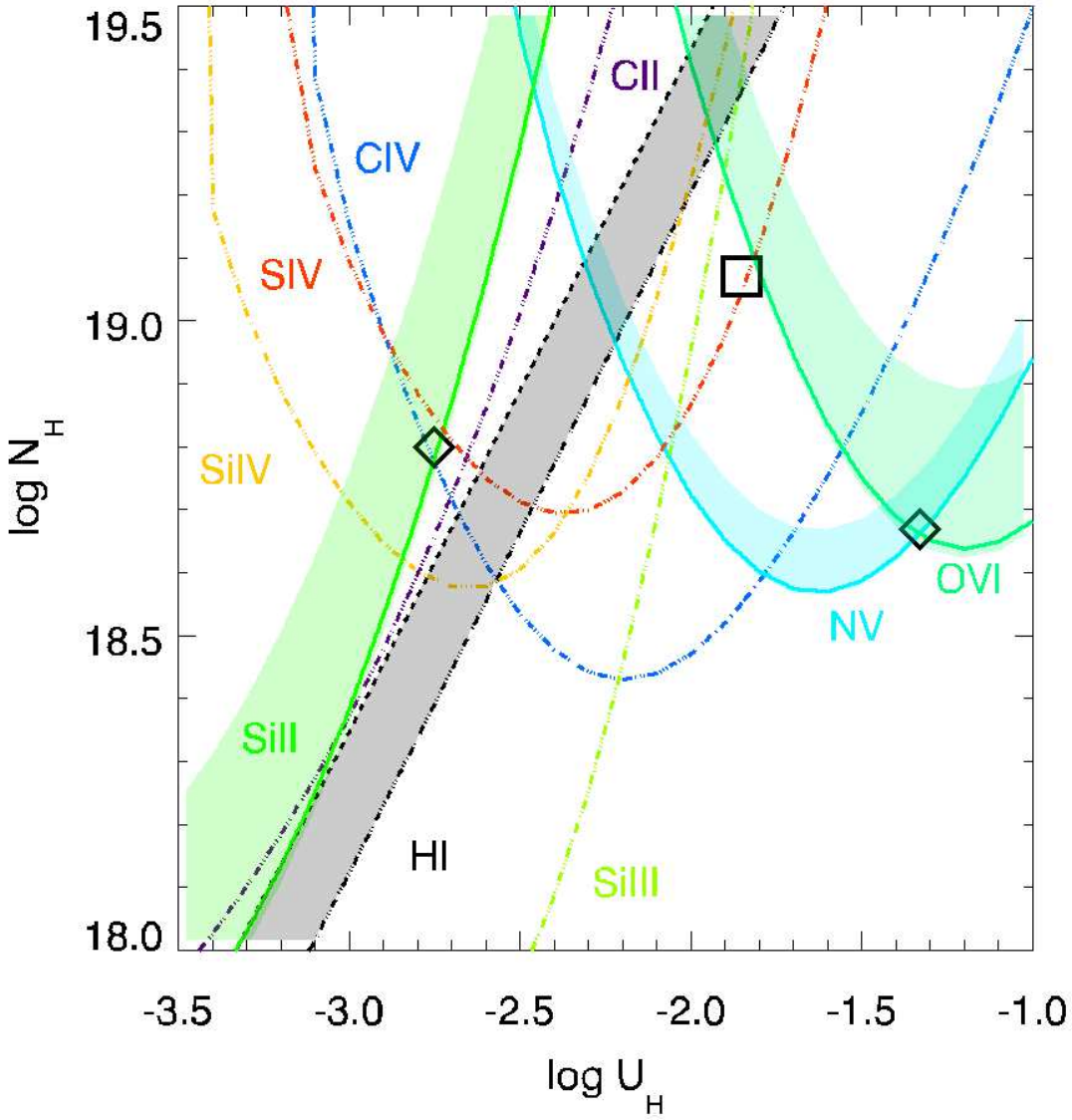

Figure 3.8 Photoionization modeling of kinematic component $T2$. The plotted lines represent slab models whose predicted N_{ion} matches the estimated values. Solid lines indicate a measured column density, dotted dashed lines a lower limit on the column density and dotted lines an upper limit on the column density. The error bars due to the photon noise as well as the systematic uncertainties in the absorber model are represented as a shaded area for each ions when an estimate is available. The black diamonds marks the two ionization component model that best fits the estimated N_{ion} while the black square marks our best single ionization model.

Table 3.7 Photoionization models for component $T2$ of IRAS F22456-5125

Ion	$\log(N_{ion})$ (cm^{-2})	$\log\left(\frac{N_{mod}}{N_{obs}}\right)$	$\log N_{mod}$		$\log\left(\frac{N_{mod}}{N_{obs}}\right)$
	Adopted[a]	SI[b]	TI_{lo}[b]	TI_{hi}[b]	TI_{lo}+TI_{hi}
$\log U_H$	$\cdots$	-1.9	-2.8	-1.3	
$\log N_H$	$\cdots$	19.1	18.8	18.7	19.05
H I	$\in$ [15.97, 16.19]	-0.25	16.38	14.66	+0.20
C II	$\gtrsim$ 13.95	-1.16	14.13	10.76	+0.18
C IV	> 14.40	+0.54	14.32	13.96	+0.08
N V	$14.07^{+0.10}_{-0.01}$	+0.40	12.80	14.05	0.00
O VI	$14.91^{+0.25}_{-0.02}$	-0.18	12.18	14.91	0.00
Si II	$13.17^{+0.37}_{-0.03}$	-1.91	13.23	8.45	+0.06
Si III	> 12.96	-0.18	14.01	10.25	+1.05
Si IV	> 13.67	-0.37	13.85	11.14	+0.18
S IV	$\gtrsim$ 13.69	+0.11	13.59	12.05	-0.09

[a] Adopted column densities reported in Table 3.6.

[b] The label SI corresponds to the single ionization model while TI_{lo} and TI_{hi} are the low and high ionization phases of the two ionization model of the absorber.

Table 3.8 Photoionization models for component $T3$ of IRAS F22456-5125

Ion	$\log(N_{ion})$ (cm^{-2})	$\log\left(\frac{N_{mod}}{N_{obs}}\right)$	$\log N_{mod}$		$\log\left(\frac{N_{mod}}{N_{obs}}\right)$
	Adopted[a]	SI[b]	TI_{lo}[b]	TI_{hi}[b]	TI_{lo}+TI_{hi}
$\log U_H$	···	-2.0	-2.7	-1.7	
$\log N_H$	···	19.0	18.2	18.8	18.90
H I	$15.63^{+0.08}_{-0.08}$	+0.10	15.69	15.20	+0.19
C II	> 13.39	-0.45	13.42	11.97	+0.05
C IV	$14.53^{+0.17}_{-0.01}$	+0.36	13.85	14.49	+0.05
N V	$14.22^{+0.27}_{-0.02}$	+0.08	12.44	14.25	+0.04
O VI	$14.81^{+0.01}_{-0.01}$	-0.35	11.93	14.72	-0.09
Si II	< 11.80[c]	-0.29	12.47	10.23	+0.67
Si III	> 12.58	+0.38	13.36	11.84	+0.79
Si IV	$13.67^{+0.07}_{-0.03}$	+0.21	13.27	12.49	+0.13
S IV	< 13.38	+0.44	13.06	13.18	-0.04

[a] Adopted column densities reported in Table 3.6.

[b] The label SI corresponds to the single ionization model while TI_{lo} and TI_{hi} are the low and high ionization phase of the two ionization model of the absorber.

[c] Upper limit set by the non detection of the stronger Si II and Si II* in that component.

Table 3.9 Ionization solution for each kinematic component of IRAS F22456-5125

Component	$\log(U_H)$		$\log(N_H)$ (cm^{-2})	
	This work	Dunn10[a]	This work	Dunn10[a]
$T1$	-0.8	-1.15	18.6	18.6
$T2$ SI	-1.9	-1.30	19.1	19.7
$T2$ TI_{lo}	-2.8		18.8	
$T2$ TI_{hi}	-1.3		18.7	
$T3$ SI	-2.0	-1.27	19.0	19.7
$T3$ TI_{lo}	-2.7		18.2	
$T3$ TI_{hi}	-1.7		18.8	
$T4$	-1.4	-1.54	18.4	18.5
$T5B$	-1.6	-1.05	19.5	20.1
$T5A$	-2.0		18.6	

[a] From Dunn et al. (2010a).

Table 3.8).

Troughs $T1$, $T4$, $T5A$ and $T5B$

For kinematic component $T1$, we essentially have five constraints (C IV, N V, O VI, Si III and H I) defining the region of the (N_H,U_H) parameter space able to reproduce the estimated ionic column densities. Visual inspection of Figure 3.10 suggests a solution around $\log U_H \sim -0.8$ and $\log N_H \sim 18.6$, consistent with the upper limits on C III from Dunn et al. (2010a). This solution accounts for every constraint to within 0.25 dex. A better solution can be found by relaxing the constraint of solar metalicity. Considering the scaling of elemental abundances of C, N and O as a function of the metalicity Z (Hamann et al., 2002), an improved solution is found for a gas of subsolar metalicity ($Z/\mathrm{Z}_\odot \sim$ -0.4) using an identical $\log U_H$ and total hydrogen column of $\log N_H \sim 19.1$ for the slab.

The constraints on the (N_H,U_H) parameter space for trough $T4$ are presented in Figure 3.11.

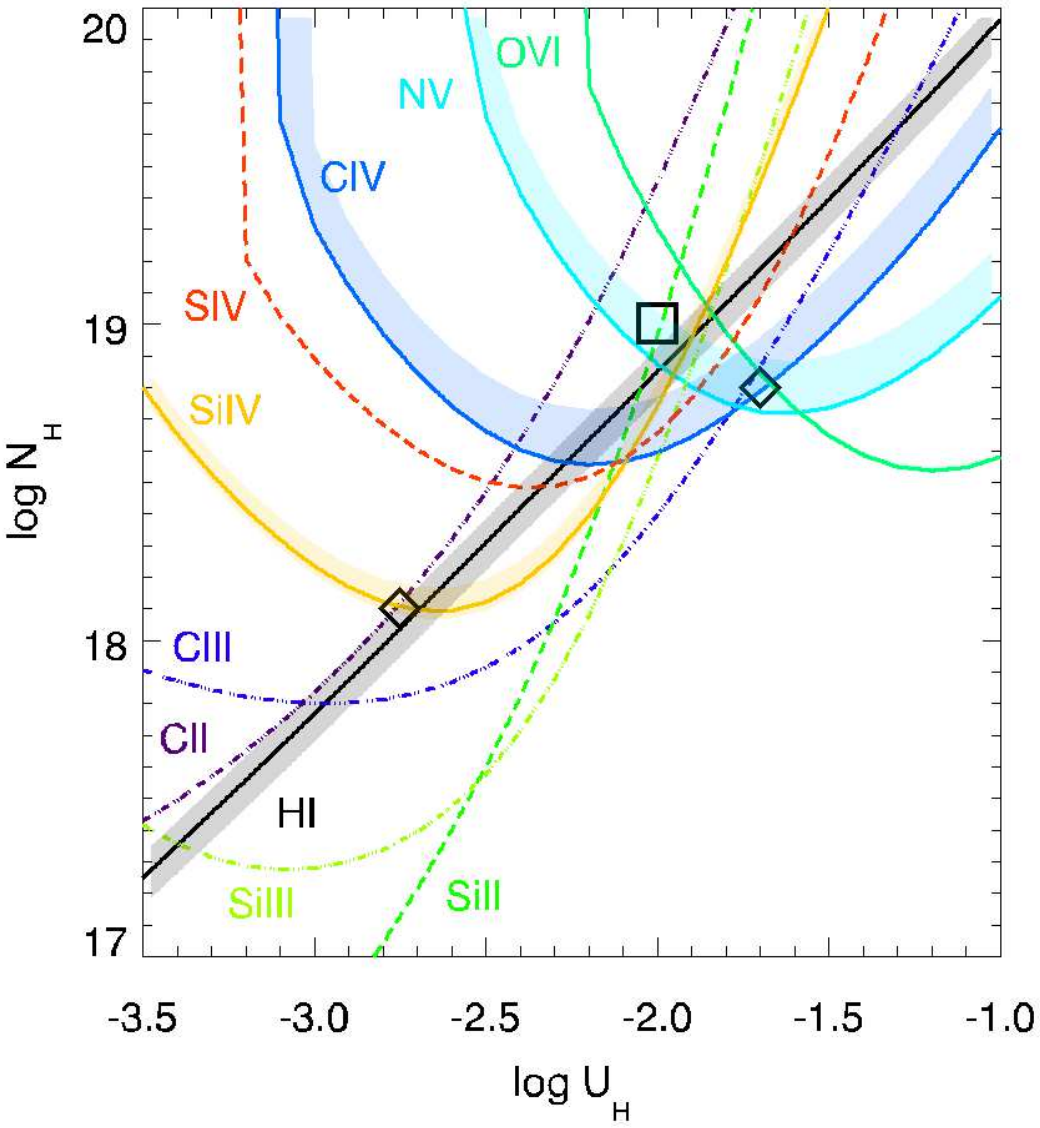

Figure 3.9 Photoionization solutions to trough $T3$. Similar presentation as Figure 3.8. Reproduced with permission of AAS (Borguet et al., 2012).

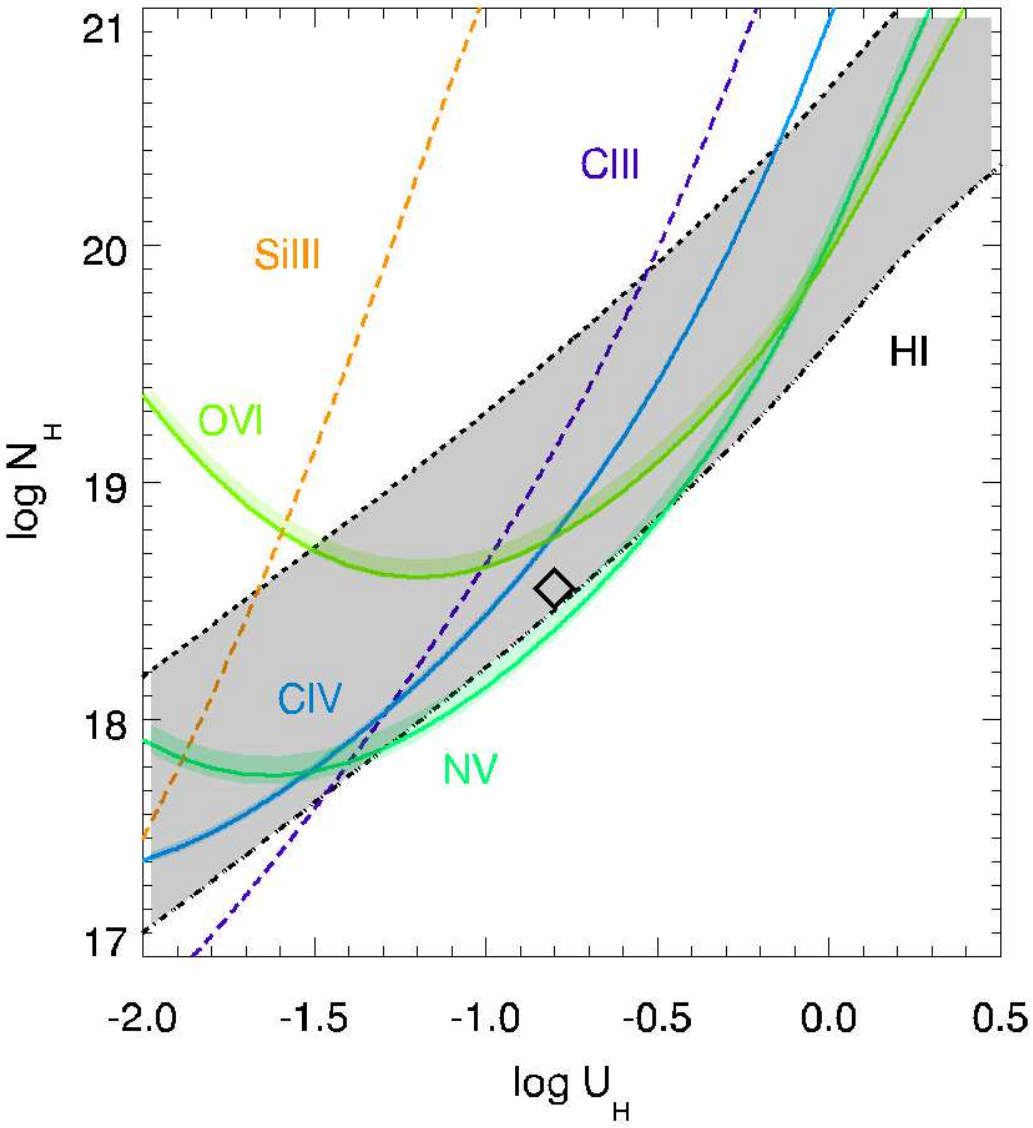

Figure 3.10 Photoionization modeling of kinematic component $T1$. Identical description to Figure 3.8. Reproduced with permission of AAS (Borguet et al., 2012).

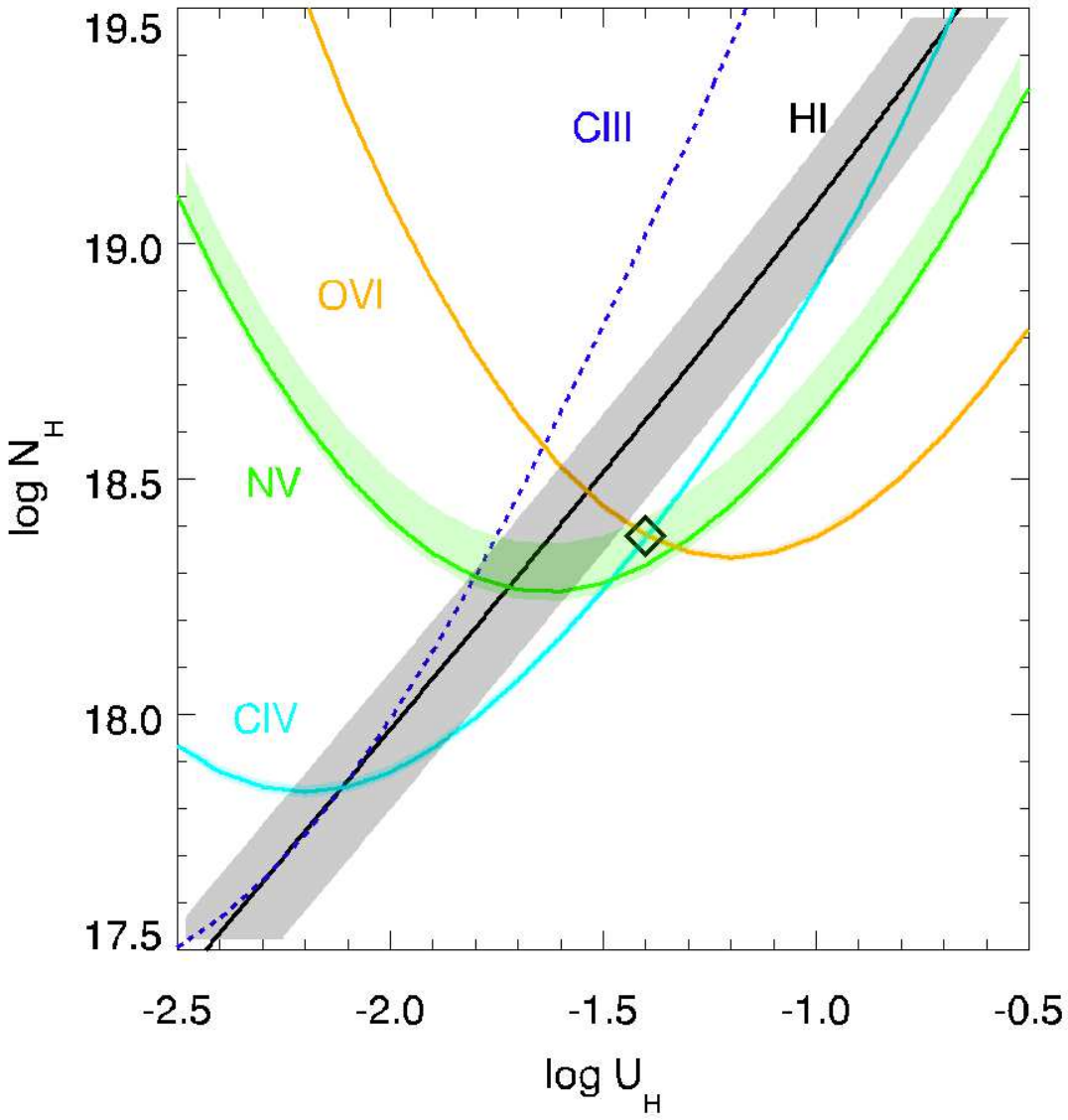

Figure 3.11 Photoionization modeling of kinematic component $T4$. Identical description to Figure 3.8. Reproduced with permission of AAS (Borguet et al., 2012).

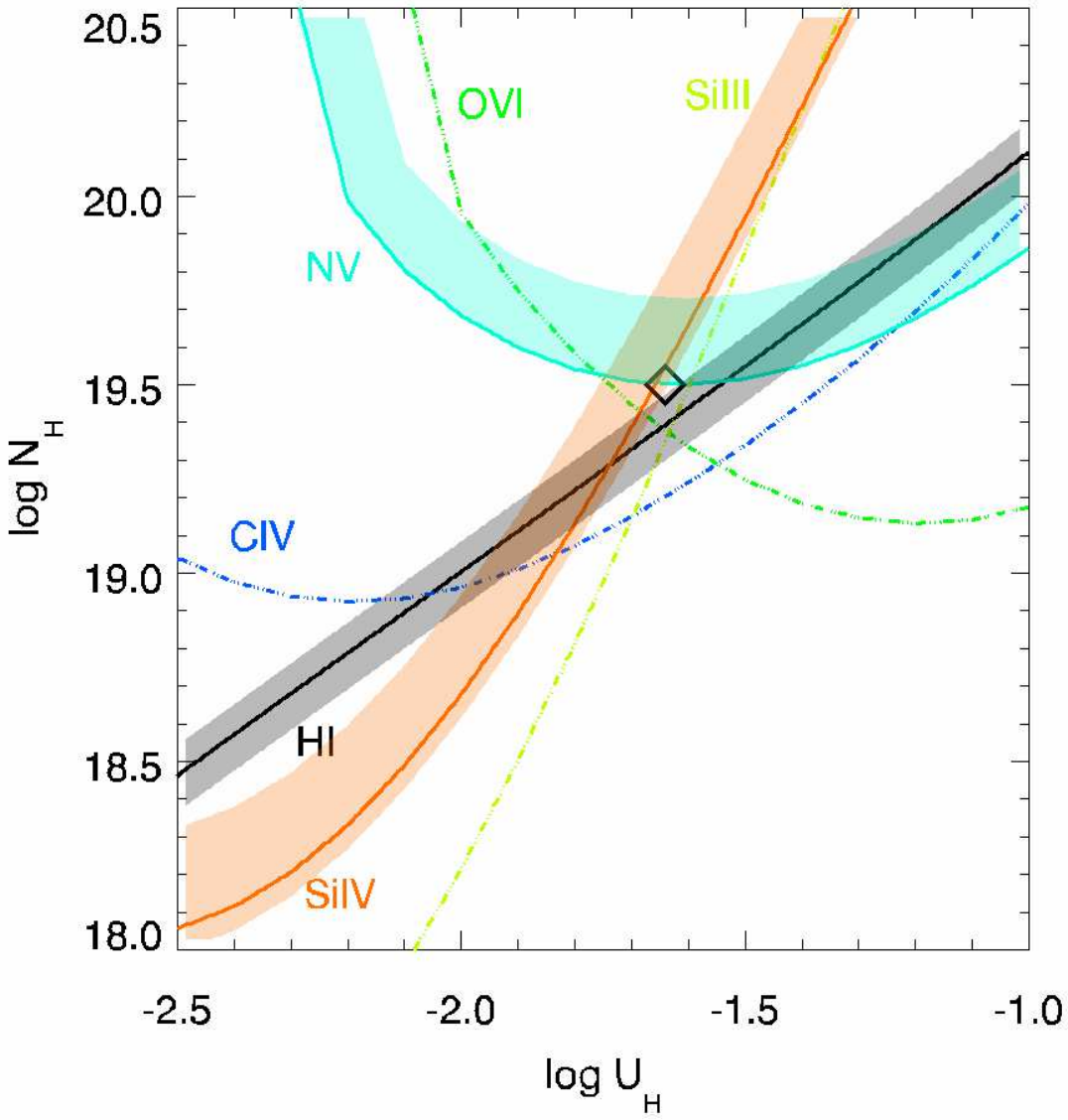

Figure 3.12 Photoionization modeling of kinematic component $T5B$. Identical description to Figure 3.8. Reproduced with permission of AAS (Borguet et al., 2012).

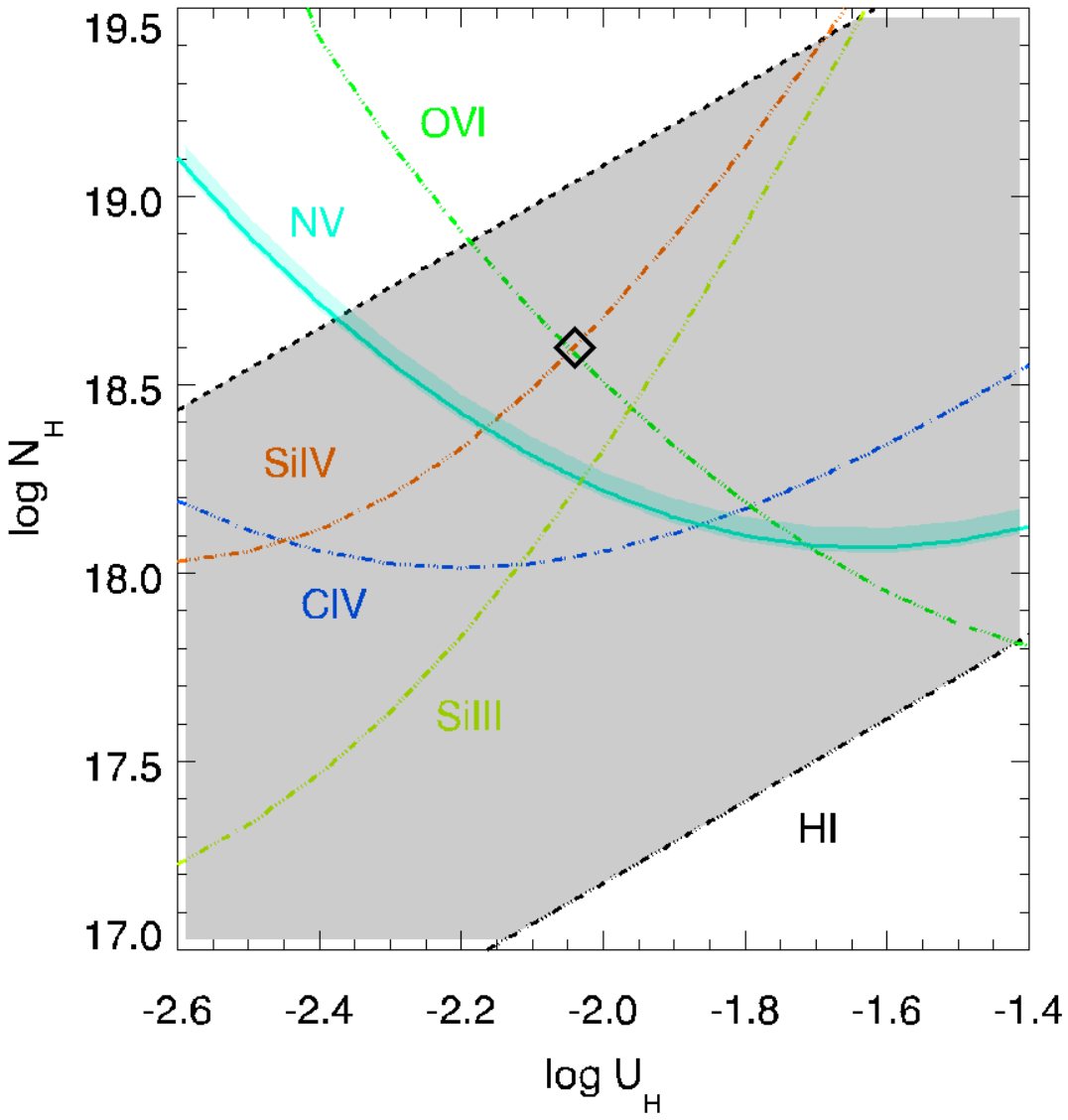

Figure 3.13 Photoionization modeling of kinematic component $T5A$. Identical description to Figure 3.8. Reproduced with permission of AAS (Borguet et al., 2012).

A solution consistent with the measured ionic column densitiese is found near $\log U_H \simeq -1.4$ and $\log N_H \simeq 18.4$. The solution is suggesting roughly solar abundances of the gas though the slight discrepancy between the measured H I column density and that predicted by the solution may suggest a subsolar metalicity medium.

The photoionization solution derived for trough $T5B$ and $T5A$ are presented in Figures 3.12 and 3.13, respectively. Inspection of Figure 3.12 suggests a solution around $\log U_H \sim -1.6$ and $\log N_H \sim 19.5$ for component $T5B$. A least-square fit to the constraints available for trough $T5A$ (Figure 3.13) provides a solution near $\log U_H \simeq -2.0$ and $\log N_H \simeq 18.6$. While the saturation observed in the troughs of several ions limits the analysis of the physical properties of the gas, the estimated (N_H,U_H) solution is able to reproduce most of the ionic columns to within a factor of 2.

Absorber distance and energetics

Detection of resonance and excited state transitions from Si II and C II in troughs $T2$ and $T3$ allows us to determine the distance to these two kinematic components from the central source. As can be seen from the definition of the ionization parameter U_H (Equation 3.10), knowledge of the hydrogen number density n_H for a given U_H and Q_H allows us to derive the distance R. When an excited state is populated by collisional excitation[1], the population of that state compared to the resonance level depends on the electron number density n_e (Osterbrock & Ferland, 2006), which is $\sim 1.2\ n_H$ in highly ionized plasma. Note that photoexcitation could also populate the metastable levels; however, with an IR flux 0.1 Jy, population of the metastable levels of C ii and Si ii is negligible in IRAS F224565125.

[1]With an IR flux $\sim$ 0.1 Jy, population of the metastable levels of C II and Si II by photoexcitation is negligible in IRAS F22456-5125.

Table 3.10 Physical properties of components $T2$ and $T3$

Component	$\log U_H$	$\log N_H$ cm^{-2}	$\log n_e$ cm^{-3}	R kpc	$\dot{M}_T$ M$\odot$/yr	$\log \dot{E}_k$ ergs/s
$T2$	-2.8	18.8	$1.70^{+0.30}_{-0.15}$	$9.2^{+4.6}_{-1.3}$	4.55	41.73
	-1.3	18.7				
$T3$	-2.7	18.2	$1.20^{+0.12}_{-0.10}$	$14.6^{+2.3}_{-1.5}$	3.65	41.35
	-1.7	18.8				

In trough $T2$ we observe resonance and excited states from C II and Si II for which column densities have been reported in Table 3.6. In Figure 3.14 we compare computed collisional excitation models for C II and Si II to the measured ratio of the column density between the excited and ground state of these two ions. For the Si II*/S II ratio, the large uncertainty comes from using PC and PL measurements of the column density associated with Si II* and S II. The C II*/C II ratio is consistent with the Si II*/S II ratio. Given the similar but still significantly different residual flux observed in the C II* and C II line profile, while the value of the column density associated with C II* and C II can change with the different absorber model, their ratio is less affected since both column densities will scale with a similar factor. For this reason we use the C II*/C II ratio to derive the electron number density of $\log n_e \simeq 1.7$ for component $T2$. This result implies a distance of $R \simeq 9.2^{+4.6}_{-1.3}$ kpc where the errors are conservatively computed from the n_e range allowed by the Si II*/Si II ratio. We note that the density derived for this component is consistent with the non detection of S IV*, only expected to be observed at higher densities.

In trough $T3$, the only excited state we observe is associated with the C II* transitions. Comparing the computed collisional excitation models for C II to the measured ratio of the column density between the excited and ground states of this ion (see Figure 3.15) we find $\log n_e \simeq 1.2$. Given the photoionization solution quoted in Section 3.1.2 the derived electron number density imply a distance of $R \simeq 14.6^{+2.3}_{-1.5}$ kpc where once again the errors on R only

reflect the uncertainty in n_e. Using the single ionization for component $T3$ (see Table 3.9) leads to a distance estimate reduced by a factor of $\sim$2 to $R \simeq 6.5^{+1.0}_{-0.7}$ kpc. Note that in the case of $T3$, we consider the AOD determination of the column densities of C II* and C II given the absence of multiple lines allowing to test for the absorber model. Similarly to what is observed for the Si II transitions in kinematic component $T2$, the net difference in residual flux between the excited and resonance troughs could lead an inhomogeneous absorber model to predict a smaller ratio (a factor of two in the case of the Si II*/Si II ratio of trough $T2$). The C II*/C II ratio derived here could then be viewed as an upper limit on the true ratio, the latter being possibly overestimated by up to a factor of $\sim$ 2, leading to an underestimation of the distance R by a factor of $\sim \sqrt{2}$.

Assuming the geometry for the outflowing material to be in the form of a thin ($\Delta R < 1/2R$), partially-filled shell, we derive the total mass M_{T_i} in each kinematic component i by $M_{T_i} = 4\pi\mu m_p R_i^2 N_{H_i} \Omega$ where $\mu = 1.4$ is the mean atomic mass per proton, m_p is the mass of the proton, and Ω is the global covering fraction of the outflow. N_{H_i} is the total hydrogen column density for the kinematic component. In the case of a two-ionization component model we simply have $N_{H_i} = N_{H_{i,lo}} + N_{H_{i,hi}}$. In this work we use $\Omega = 0.5$ since outflows are detected in about 50% of the observed Seyfert galaxies (e.g. Crenshaw et al. 2003). The average mass flow rate $\dot{M}_{T_i}$ is obtained by dividing the total mass of the shell by the dynamical timescale R_i/v_i. The kinetic luminosity is finally given by $\dot{E}_{k_i} = 1/2\dot{M}_{T_i} v_i^2$. We list the computed values of R, $\dot{M}_T$ and $\dot{E}_k$ for troughs $T2$ and $T3$ in Table 3.10.

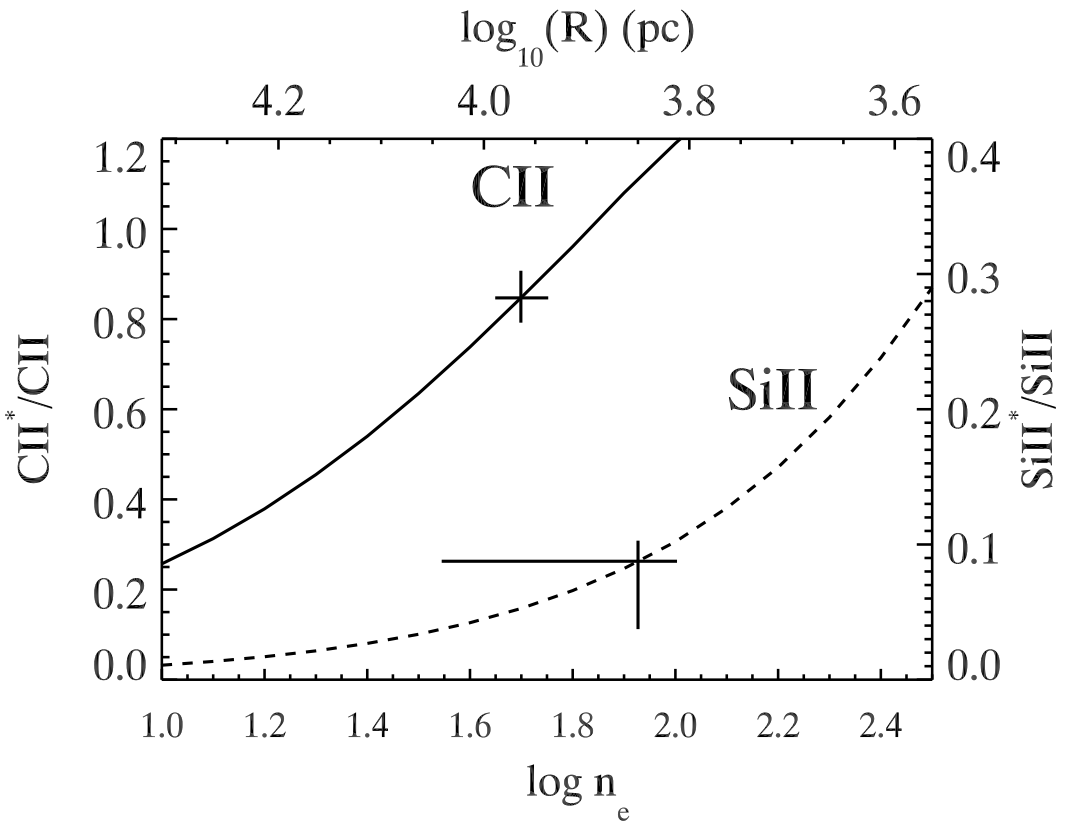

Figure 3.14 Density diagnostic for kinematic component $T2$. In this figure we plot the theoretical ratio of the level population of the first excited states of C II ($E = 63$ cm^{-1}) and of Si II ($E = 287$ cm^{-1}) to the level population of the ground state versus the electron number density n_e for a temperature of 10000 K. The ratios derived from C II and Si II (black crosses) imply an electron number density $\log n_e \simeq 1.7$. The uncertainty on the derived n_e only accounts for the error on the ratio N_{ion*}/N_{ion}. On the top axis, we report the corresponding distance as a function of n_e considering the ionization parameter of the low ionization phase ($\log U_H = -2.8$).

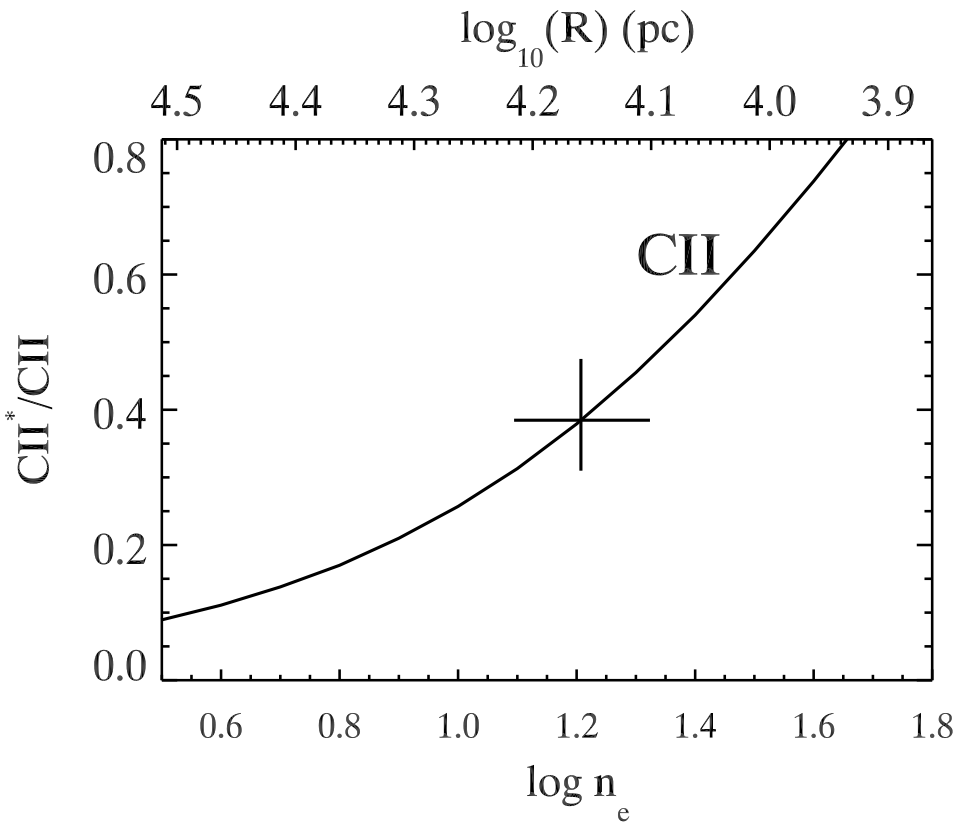

Figure 3.15 Density diagnostic for kinematic component $T3$. We plot the theoretical ratio of the level population of the first excited states of C II ($E = 63$ cm^{-1}) to the level population of the ground state versus the electron number density n_e for a temperature of 10000 K. The ratio derived from C II and C II* lines is implying an electron number density $\log n_e \simeq 1.2$. On the top axis, we report the corresponding distance as a function of n_e considering the ionization parameter of the low ionization phase ($\log U_H = -2.7$).

3.1.3 QSO 1044+3656

*All sections pertaining to QSO 1044+3656 were written with Jay Dunn. Ionic column density measurements were provided by Jay Dunn.

One of the first BALQSOs for which estimates of Ek and M were determined is QSO FIRST J104459.6+365605 (hereafter QSO 1044+3656). de Kool et al. (2001, hereafter dK01) measured Nion of absorption troughs from Fe ii (E=0, as well as from several excited state levels), Mg i, and Mg ii in their Keck High Resolution Echelle Spectrometer (HIRES) observation of this object. Using photoionization analysis, their determinations of Nion constrained the ionization parameter (UH) and NH of the outflow, to 3 and 2 orders of magnitude, respectively, inadequate for an accurate determination of Ek and M . To better constrain UH and NH we need Nion measurements from either higher ionization species (Moe et al. 2009; Dunn et al. 2010a) or those arising from excited-state He i (metastable 23 S with energy 159859 cm1 ; hereafter He i*) (Arav et al. 2001; Korista et al. 2008). The low redshift of the object (z 0.7) precluded the first approach, as none of the higher ionization lines are redshifted into the optical region. However, the He i* lines at 3890 and 3188 A are well situated for ground-based optical observations. Upon noticing that the SDSS spectrum of QSO 1044+3656 shows He i* absorption troughs arising within the outflow, we targeted that spectral region (which was not observed with Keck/HIRES) for high quality observations using the 4.2-m William Herschel Telescope (WHT). The ionic column densities measured in the WHT spectrum are given in Table 3.11.

As explained by Korista et al. (2008), the combination of the ionic column densities of Fe II and He I* yields tight constraints on the two fundamental photoionization parameters; the

Table 3.11 Column Density Determinations for QSO 1044+3656

Ion	E_{low}[a] cm^{-1}	N_{ion} 10^{12} cm^{-2}	error[b] 10^{12} cm^{-2}
He I*	159859	220	34(51)
Mg I	0	9.5	0.2(0.9)
Fe II	0	650	34(48)
Fe II	385	120	5(19)
Fe II	1783	310	13(65)
Fe II	7955	5.4	0.8(5.0)

[a] Energy of lower level of transition.
[b] Statistical errors of the column densities. The value in parentheses is the systematic uncertainty due to continuum placement.

total hydrogen column density (N_H) and the ionization parameter

$$U_H \equiv \frac{Q_H}{4\pi R^2 n_H c}, \tag{3.11}$$

where n_H is the total hydrogen number density, c is the speed of light, and Q_H is the number of hydrogen ionizing photons emitted per second by the central source.

To estimate Q_H, we use the flux calibrated spectrum of QSO 1044+3656 from the Sloan Digital Sky Survey (SDSS). We begin by correcting the spectrum for Galactic extinction with a Milky Way reddening curve. The sightline through the Milky Way to QSO 1044+3656 has E(B-V) = 0.062 (Schlegel et al., 1998). Next, we correct for dust extinction intrinsic to the quasar. The rest-frame UV spectra of low-ionization BALQSOs are almost always redder than any other major class of AGN, and as such are likely observed through a dust screen within the host galaxy (Dunn et al., 2010b; Reichard et al., 2003; Urrutia et al., 2009). To that end, we use a Small Magellanic Cloud reddening curve to adjust the rest-frame SDSS spectrum to match the shape of the FIRST Bright Quasar Survey composite

spectrum (Brotherton et al., 2001). We find the best fit occurs for an E(B-V) = 0.054. Using the reddening corrected SDSS spectrum, we match it to a standard AGN spectral energy distribution (SED, Mathews & Ferland, 1987)) between 3300 and 4000 Å and find a resulting bolometric luminosity of $L_{Bol} = 6.9 \times 10^{46}$ ergs s^{-1} cm^{-2} Å^{-1}, and $Q_H = 7.0 \times 10^{56}$ photons s^{-1}.

Mass flux and kinetic luminosity determinations rely on the total hydrogen column density in the absorber and the distance to the absorber. We constrain these parameters by modeling the ionization structure of a single slab of constant density gas irradiated by an ionizing source. Using version c08.00 of the spectral synthesis code Cloudy (Ferland et al., 1998), we first consider photoionization models with solar abundances and the MF87 SED[2]. We search the parameter space to find values of U_H, N_H, and n_H that match simultaneously the measured column densities of He I*, Fe II ($E_{low} = 0$ cm^{-1}), and Fe II ($E_{low} = 385$ cm^{-1}). As in dK01, the ratios of Fe II excited-state level populations to the ground level (in particular E_{low} = 385 cm^{-1} to E_{low} = 0 cm^{-1}) provide the most important constraint on the gas density. We find that the best fitting model with solar abundances has the following parameters; log n_H (cm^{-3}) = 4.0, log U_H = −2.27, and log N_H (cm^{-2}) = 20.76. The Fe II-weighted mean electron number density is log n_e (cm^{-3}) = 3.8, and the n_e weighted mean electron temperature within the Fe II zone is 10,500 K. We note that while the solution is just past the hydrogen ionization front, the temperature never drops below 6900 K. This model matches the column density of He I* to within 0.1 dex and the column densities of Fe II ground state and Fe II from the 385 cm^{-1} energy state to within 0.04 dex of the measured values. It also matches the measurements of the Fe II column densities from the 1783 cm^{-1} energy level to ∼0.05 dex, and the column density of the 7955 cm^{-1} energy level to 0.3 dex. The last of these determinations is consistent with the large measurement uncertainty in the continuum

[2]We use the SED as implemented in Cloudy as table AGN, which differs from the Mathews-Ferland SED by the addition of a sub-millimeter break at 10 μm.

placement, given the shallow trough of a single transition. The total Fe II column density in the model is log (N_{ion}) = 15.1; lower than the value determined by dK01 of 15.3, but consistent within the uncertainty of their determination.

To get an idea of the errors for U_H, N_H, and n_H, we run a grid of models around our best fitting model varying these parameters. We find that N_H and U_H are strongly correlated and the allowed solutions are on a narrow strip centered around the line $N_H = 10^{23} U_H + 2.8 \times 10^{19}$ in the range log U_H = -2.28 to -2.09 for $3.9 \leq \log n_H \leq 4.1$. This narrow band allows for smaller errors on kinetic luminosity and mass flux determinations than would otherwise be allowed.

Inspection of the grid of models reveals how small changes in N_H and U affect He I* and Fe II for a given n_H. He I* is only mildly affected by 0.01 dex changes in N_H and U_H, while Fe II changes significantly. In the case where N_H was increased by 0.01 dex, we see a 50% increase in the column density of Fe II (0) and only a 0.4% increase in the column density of He I*. Changing U_H yields similar results for Fe II while N_{HeI*} scales with U_H. The sensitivity of Fe II to small changes in hydrogen ionization parameter and column density results in the very tight correlation of N_H and U_H described above.

The models discussed so far have assumed solar abundances, but metallicities of gas near quasars can be supersolar (e.g., Hamann et al., 2002). In particular, BAL outflows are known to have supersolar metallicities (e.g., Gabel et al., 2006; Dunn et al., 2010b). To see how increased metallicity of the gas affects our determination of U_H, N_H, and n_H, we consider photoionization models with Z=2 and Z=4. We find valid solutions for both metallicities. Comparisons of these two models with our solution for Z=1 are also shown in Table 3.12. We note that using 4 times solar metallicity results in changes of less than $\sim$30% in both N_H and U_H. Thus our photoionization solutions are only mildly sensitive to large metallicity

Table 3.12 Photoionization Models for QSO 1044+3656

Z[a]	log N_H	log U_H	log n_H	N_{HeI*}[b]	$N_{FeII(0)}$[b]	$N_{FeII(385)}$[b]
Measured Values						
-	-	-	-	220 ±51	650 ±48	120 ±19
Best Fit Model for Z=1 and MF87 SED						
1	20.76	-2.27	4.00	174	613	108
Models with Supersolar Abundances and MF87 SED						
2	20.80	-2.13	3.85	235	634	123
4	20.68	-2.15	3.80	246	623	128
Model with UV-soft SED and Solar Abundances						
1	20.76	-2.26	4.00	176	636	105

[a] metallicity compared to solar
[b] in units of 10^{12} cm^{-2}

enhancements.

In order to test the sensitivity of the derived parameters to the shape of the SED, we compare the best model found for Z=1 using the MF87 SED to a similar model using the UV-soft SED of Dunn et al. (2010a; see their Figure 11 for a comparison of the two SEDs). The results are presented in Table 3.12. We find that there is little change in model predictions for column densities of He I* and Fe II.

We see from the values in Table 3.12 that the total hydrogen column density and ionization parameter change very little with changes in gas metallicity or shape of the ionizing continuum. We also see that Fe II is very sensitive to small changes in N_H and U_H. Photoionization models indicate that all of the Fe II comes from a thin layer at the outer edge of the slab. This phenomenon was discussed for QSO 1044+3656 in dK01, for Q0059-2735 in Wampler et al. (1995), and for QSO 2359−1241 in Arav et al. (2001) and Korista et al. (2008). For slabs that are thick enough for a hydrogen ionization front to form, the position of the front is proportional to U_H ($N_H \approx 10^{23} U_H$). Since Fe II is the dominant species behind the ioniza-

tion front, due to shielding by neutral hydrogen, its column density is very sensitive to the thickness of the slab relative to the position of the ionization front resulting in a very tight correlation of N_H and U_H. Even small departures from the narrow strip of values determined above results in predictions for Fe II that are inconsistent with the measurements. In all of our models with solar metallicities, He I*, populated by recombination of He II, drops off due to the formation of a He I front. Therefore, He I*, the majority of which is found between the He II and He I ionization fronts, is largely insensitive to changes in N_H. Changing the SED has little effect on these results since the ionization parameter determines the position of the hydrogen ionization front and the He II front changes very little. For the UV-soft SED, the He II ionization front is 0.1 dex closer to the illuminated face of the slab than for the MF87 SED resulting in a 1% increase in the column density of He I*. However, choice of SED will affect the distance to the absorber since a change in Q_H requires a corresponding change in distance in order to keep U_H constant.

Due to the sensitivity of the Fe II column density to the U_H and N_H position of the hydrogen ionization front, it is difficult to affect He I* while keeping Fe II within the constraints using solar metallicity. Increasing metallicity results in a somewhat larger He I* column density that is still within the measured errors since the models with solar metallicity predict He I* on the low side of the constraints. We then adjust the position of the hydrogen ionization front relative to the slab thickness by changing N_H and U_H until the Fe II column density is matched. In order to keep the Fe II(385) to Fe II(0) ratio constant, the hydrogen number density changes. We investigate how the uncertainties in the ionizing SED and metallicity of the gas affect mass flux and kinetic luminosity determinations in the next section.

Kinetic Luminosity and Mass Flux of the Outflow

Using the photoionization properties of the outflow derived in the previous section, we can estimate its energetics. Assuming the outflow is in the form of a partial thin, spherical shell (see § 6.1) moving with a constant radial velocity of v and a distance R from the source, the mass flux of the flow is (see Dunn et al. 2010a, Equations 8-11):

$$\dot{M} = 4\pi\mu m_p \Omega R N_H v, \tag{3.12}$$

where N_H is the total column density of hydrogen, m_p is the mass of a proton, μ=1.4 is the plasma's mean molecular weight per proton, and Ω is the fraction of the shell occupied by the outflow. The resulting kinetic luminosity is:

$$\dot{E}_k = 2\pi\mu m_p \Omega R N_H v^3. \tag{3.13}$$

The median radial velocity of cluster 2 is straightforwardly measured from the spectrum to be ~ -4030 km s^{-1}. Our photoionization models determine N_H (as well as U_H and $n_{_H}$, which will yield the distance). For the solid angle covered by the outflow, we use the canonical BAL value of $\Omega = 0.2$ (see discussion in Dunn et al., 2010b). To find the distance we insert $n_{_H}$ and U_H into Equation 1, and solve for R.

For the allowed solar metalicity and MF87 SED models, we find $1.4 < R < 2.0$ kpc. The tight correlation between N_H and U_H in the acceptable models, combined with the $R \propto (U_H n_{_H})^{-0.5}$ dependency inferred from equation (1) reduces the uncertainty in the inferred $\dot{M}$ and $\dot{E}_k$ considerably. For the allowed range of N_H, U_H and $n_{_H}$, equations 2 and 3 yield $\dot{M}$ = (125–145) M$_\odot$ yr^{-1} and $\dot{E}_k$ = (1.2–1.3) $\times 10^{45}$ ergs s^{-1}. This kinetic luminosity is $\sim$1% of its bolometric luminosity, where L$_{Bol} \approx 6.9 \times 10^{46}$ ergs s^{-1} from the MF87 SED.

We also explore the effects of supersolar abundances and choice of SED on the energetics. In section 5.1, we showed that increasing the metalicity (Z) to 2 and 4 times the solar value, yield only modest changes in U_H, N_H and n_H. For the $Z = 4$ model we obtain: $R = 2.1$ kpc, $\dot{M} = 115$ M$_\odot$ yr^{-1}, and $\dot{E}_k = 0.6 \times 10^{45}$ ergs s^{-1}. To examine the effect of a different SED on the energetics, we used the UV-soft SED model (see Table 2). We find that the model matches the ionic column density measurements without appreciable change in U_H and N_H. Thus, the major effect of the new SED is the drop in Q_H, which decreases the distance of the outflow determined from the best fit model in Table 2 from 1.9 to 1.7 kpc and therefore $\dot{M}$ and $\dot{E}_k$ to 95 M$_\odot$ yr^{-1} and 0.5×10^{45} ergs s^{-1}. We note that while this drops the total $\dot{E}_k$, the bolometric luminosity derived from this SED is also smaller. Due to this, the ratio of $\dot{E}_k/L_{Bol}$ only decreases by less 0.1%.

Allowing for a metalicity range $1 < Z < 4$ and taking into account both the hard MF87 and a soft SED, we derive the following range in outflow properties: R=1.7 $\pm$ 0.4 kpc, $\dot{M} = 120$ $\pm$ 50 $\Omega_{0.2}$ M$_\odot$ yr^{-1}, and $\dot{E}_k = 0.7 \pm 0.3 \times 10^{45}$ $\Omega_{0.2}$ ergs s^{-1}, where $\Omega_{0.2} \equiv \Omega/0.2$.

Comparisons with the Results of dK01

dK01 also to used photoionization models to constrain N_H and U_H. Their models relied on the values of total Fe II and Mg I column densities, and the limit placed on the Fe I column density due to a lack of detection. Because they only had a limit on the Fe I column density and the fact that the column density of Mg I is relatively insensitive to the U_H and N_H location of the ionization front, they ran models spanning ranges in log U_H from -1 to -6 and log n_H (cm^{-3}) from 3.9 to 5.0. The resulting ranges in N_H and distance from these models were log N_H (cm^{-2}) between 20 and 22 and a range in distance from 0.1 to 94 kpc. We note that several of their models were unable to find a satisfactory N_H. Considering

only those models with solutions of N_H their range in the distance of the outflow is 0.1 to 4.2 kpc.

We are able to better constrain U_H, N_H, and n_H (we note that this is regardless of the systematic uncertainties in abundances and SED, which we discuss above). This is due to the combination of He I* and Fe II column densities, which are very sensitive to the U_H and N_H values of the ionization front (Korista et al. 2008). Further, we tightly constrain the number density from the ratios of Fe II* state to ground state column densities. The distances derived from our solar models span 1.4 to 2.0 kpc, which is a factor of ∼30 improvement compared to the factor of 42 uncertainty derived from the models of dK01.

The final energetic results of dK01, despite the wide range in U_H and N_H for their models, span only an order of magnitude in both $\dot{E}_k$ and $\dot{M}$ when calculated for each model individually (including only those models with N_H solutions). This is due to the correlation between U_H and N_H in photoionization models as we have discussed in §5.1 (also see Moe et al. 2009). This correlation is similarly seen in the ranges of $\dot{E}_k$ and $\dot{M}$ for our full set of acceptable models, which is a factor of ∼14 improvement over the uncertainty in the dK01 models. Therefore, by including the column density of He I*, we have improved the determination of the physical properties of the outflow in two ways; 1) we provide a much tighter uncertainty on the distance (and therefore $\dot{E}_k$ and $\dot{M}$), and 2) we have shown that the energetics are relatively insensitive to changes in SED or chemical abundances.

3.1.4 AKARI J1757+5907

*All sections pertaining to AKARI J1757+5907 are published in Aoki et al. (2011) and are reproduced here with permission of PASJ.

AKARI-IRC-V1 J1757000+590759 (hereafter AKARI J1757+5907) is discovered during the follow-up observations of AKARI mid-infrared (MIR) All-Sky Survey. The infrared satellite AKARI performed an all-sky survey at 9 and 18μm as well as at four far-infrared bands (Murakami et al., 2007; Ishihara et al., 2010). The initial identification of the AKARI MIR All-Sky Survey sources involved association with Two Micron All Sky Survey (2MASS) catalog (Skrutskie et al., 2006). This search highlights some AKARI MIR sources with $F(9\mu\mathrm{m})/F(Ks) > 2$ in the high galactic latitude $|b| > 20$ after excluding the sample in the Large and Small Magellanic Clouds. AKARI J1757+5907 has a large ratio of mid-IR to near-IR flux density ($F(9\mu\mathrm{m})/F(Ks) = 11.1$). This mid-IR source is also coincident with a bright near-UV and optical source. The high brightness of this QSO permits us to do high resolution spectroscopy of He I* absorption lines and search for Fe II resonance and excited absorption lines. Thus, we chose this QSO as our next target for determination of $\dot{E}_k$ and $\dot{M}_{out}$.

Photoionization Modeling

Through photoionization modeling, reliable measurements of He I* and Fe II column densities provide powerful constraints on the total hydrogen column density, N_H, and the hydrogen ionization parameter,

$$U_H \equiv \frac{Q_H}{4\pi R^2 n_H c}, \tag{3.14}$$

where n_H is the total hydrogen number density, and c is the speed of light. We use version c08.00 of the spectral synthesis code Cloudy, last described by Ferland et al. (1998), to model a plane-parallel slab of gas with constant hydrogen density irradiated by a source continuum. We focus on the kinematic components spanning a velocity range from -800 km s^{-1} to -1050 km s^{-1} since we detect Fe II(0). In this velocity range, measurements of upper limits on the sextet D level Fe II(385) and the quartet D level Fe II(7955) yield upper limits of electron number density n_e, $10^{3.6}$ and $10^{3.8}$ cm^{-3}, respectively. We adopt the conservative value of an upper limit of $n_e \leq 10^{3.8}$ cm^{-3}. While the electron number density is well constrained from above, there are no diagnostics for a lower limit on n_e in the data.

We begin investigation of the parameter space by using Cloudy's optimization mode to determine N_H and U_H for $\log n_H = 3.8$. The parameters N_H and U_H are varied and ionic column densities are computed for each set of parameters. Best fit values are determined by χ^2 minimization for given tolerances in the measured ionic column densities. For solar abundances and the MF87 SED, as implemented by Cloudy[3], we find $\log U_H = -2.15$ and $\log N_H = 20.82$ yield good fits to the column densities of He I* and Fe II while $N_{Mg\,II}$ is overpredicted. However, as discussed in section 4, the Mg II troughs may be more saturated than the partial covering model suggests. A hydrogen ionization front, which we define as the position at which half of the total hydrogen is neutral (approximated by $N_H = 10^{23} U_H$), does not form in this solution although we are very close to it with $\log(N_H/U_H) = 22.96$.

Since the data do not provide a lower limit to the electron number density, we find other valid solutions by reducing n_H. When the hydrogen number density is reduced, the He I* population drops. This is due to the fact that He I* is populated by recombination of He II and the number of recombinations per unit time depends linearly on n_e. The ionization parameter must increase in order to replenish the He I* population. Fe II becomes dominant

[3]This SED differs from the MF87 SED by the addition of a sub-millimeter break at 10 μm.

near the hydrogen ionization front, while He I* drops off drastically at the front. Thus, solutions in this region of the slab have U_H fixed by $N_{He\,i*}$ and the ratio N_H/U_H fixed by $N_{Fe\,ii}$. Due to the tight correlation of N_H and U_H, all valid solutions have a similar ratio laying (nearly) on a straight line in the N_H-U_H plane for number densities greater than ~ 100 cm^{-3}. At these densities, the slabs do not form a hydrogen ionization front. As we go to densities lower than ~ 100 cm^{-3}, a front forms, behind which Fe II and Mg II increase linearly with N_H.

In order to determine what effects choice of SED may have on N_H and U_H, we compare results of the MF87 SED with results of a softer SED. The soft SED has an optical to X-ray spectral index $\alpha_{ox} = -1.5$ compared to the MF87 SED with $\alpha_{ox} = -1.4$ (with the convention $\nu F_\nu = \nu^\alpha$) and was generated using the Cloudy command agn 375000 -1.50 -0.125 -1.00, where the numbers are the temperature of the UV bump, α_{ox}, α_{uv}, α_x, respectively. We find the resulting N_H and U_H are nearly identical and conclude that changing the SED only affects the energetics through Q_H, a finding consistent with the analysis of QSO 1044+3656 reported in Arav (2010).

Another assumption in our models is solar abundances and metallicity. To check the sensitivity of our results to metallicity changes, we use the abundances in table 2 of Ballero et al. (2008) for metallicity Z=4.23 with the MF87 SED and $\log n_H = 3.8$. While helium abundances are expected to increase with oxygen abundances (e.g., Olive & Scully (1996)), the amount of increase varies for different galaxies. Therefore, we arbitrarily increase the helium abundance by 15% from solar. We find that $\log U_H$ is approximately 0.02 dex lower and $\log N_H$ is approximately 0.15 dex lower for the increased metallicity model with $\log(N_H/U_H) = 22.83$. We discuss the effect of these changes on the energetics of the outflow in the next section.

Table 3.13 Column Densities for the Outflow in AKARI J1757+5907

SED	Z ($Z_\odot$)	log N_H (cm^{-2})	log U_H	log n_H (cm^{-3})	Measurement Method	$N_{He\,i*}$ (10^{12} cm^{-2})	$N_{Fe\,ii(0)}$ 10^{12} cm^{-2}	$N_{Mg\,ii}$ 10^{12} cm^{-2}
					Measurements			
-	-	-	-	-	Apparent Optical Depth	156.9 ±0.8	24.9 ±0.6	160.9 ±0.7
-	-	-	-	-	Partial Covering	179.3 ±8.0	29.1 ±3.0	226.7 ±6.7
-	-	-	-	-	Power Law	180.2 ±3.2	30.4 ±3.7	602 ±246
					Models			
MF87	1.00	20.82	-2.15	3.8	-	176.5	30.9	1341.5
Soft	1.00	20.81	-2.15	3.8	-	180.5	32.4	1364.6
MF87	4.23	20.66	-2.17	3.8	-	172.3	31.2	1815.5

Energetics of the Outflow

Of particular interest for any outflow is the mass flow rate $\dot{M}_{out}$ and mechanical work output or kinetic luminosity ($\dot{E}_k$). When considering a thin partial shell moving with a constant radial velocity (v) and at a distance R from the source, the mass flow rate is defined as (see Dunn et al. (2010b) and Arav (2010)):

$$\dot{M}_{out} = 4\pi\mu m_p \Omega R N_H v, \tag{3.15}$$

where N_H is the total column density of hydrogen, m_p is the mass of a proton, μ=1.4 is the plasma's mean molecular weight per proton, and Ω is the fraction of the shell occupied by the outflow. This gives a kinetic luminosity:

$$\dot{E}_k = 2\pi\mu m_p \Omega R N_H v^3. \tag{3.16}$$

For the troughs we consider in AKARI J1757+5908, the median velocity of the system is -970 km s^{-1}. We assume that $\Omega = 0.2$ from the canonical detection rate of C IV BALs (see discussion in Dunn et al. (2010b)). To determine the distance, we can solve Equation (1) for R, which depends on U_H and n_H. Due to lack of excited state lines, we are only

able to determine an upper limit for the density from the noise (see Section 3.1.4) of log n_H (cm^{-3}) $<$ 3.8. This sets a lower limit on the mass flow rate, and thereby the kinetic luminosity, due to the fact that the ratio important these quantities from photoionization modeling, $N_H/\sqrt{U_H n_H}$, monotonically increases as number density decreases. Also, we are able to determine a lower limit of log U_H = -2.15 for our upper limit n_H model (see previous section for full explanation). The combination of these two parameters, and the value of Q_H from Section 5 (using the reddened value as a lower limit), provides a lower limit on the distance, $R > 3.7$ kpc. This limit in R in turn provides lower limits for both $\dot{M}_{out}$ and $\dot{E}_k$. The last required parameter needed to determine the energetics of the outflow we derived in the previous section, N_H (cm^2) = 20.82. Including this value of N_H, we find lower limits of $\dot{M}_{out} > 68\ \Omega_{0.2}\ M_\odot$ yr^{-1} and $\dot{E}_k > 2.0 \times 10^{43}\ \Omega_{0.2}$ ergs s^{-1}, where $\Omega_{0.2} \equiv \Omega/0.2$.

The mass of the black hole (M_{BH}) of AKARI J1757+5907 is derived to be $4.0 \times 10^9 M_\odot$ based on the width of the Hβ emission line of σ = 2160 km s^{-1} and the optical luminosity λL(5100Å) of 3.8×10^{46} erg s^{-1}. We use the formula in Bennert et al. (2010) based on the calibrations of broad-line region size-luminosity relation (Bentz et al., 2006) and the virial coefficient taken from Onken et al. (2004). The derived $\log L_{bol}/L_{Edd} = -0.13$ is used for calculation of mass accretion rate ($\dot{M}_{acc}$) based on the accretion disk model by Kawaguchi (2003). The $\dot{M}_{acc}$ is 110 $M_\odot$, and very close to the lower limit of $\dot{M}_{out}$.

This limit is derived from our determination of n_e that is primarily dependant upon our non-detection of the Fe II* λ2612 line. With 5$\times$ higher S/N spectrum, we would potentially find a number density of log n_H (cm^{-3}) $<$ 2.9 (assuming the line is still not detected). For this value of n_H and our best model at that density (U_H = -1.66 and N_H = 21.32), we find $R > 5.9$ kpc, $\dot{E}_k > 10.2 \times 10^{43}\ \Omega_{0.2}$ ergs s^{-1} and $\dot{M}_{out} > 342\ \Omega_{0.2}\ M_\odot$ yr$^-$1.

3.1.5 HE0238-1904

*This section on observations and column density measurements provided by Nahum Arav and Benoit Borguet.

The quasar HE0238-1904 was observed with HST/COS (see Osterman et al. 2010, for on-orbit performance) on 2009 December 31. Spectra of the target were obtained using the Primary Science Aperture (PSA) in both the G130M ($1135\mathring{A} < \lambda < 1480\mathring{A}$) and G160M ($1400\mathring{A} < \lambda < 1795\mathring{A}$) medium-resolution gratings as part of the COS Guaranteed Time Observations (GTO) program (PI: Green, PID: 11541) and totaled 6451 s and 7487 s in the G130M and G160M gratings, respectively. Both sets of observations used multiple grating central settings in order to provide a continuous spectral coverage across the entire COS far-UV band as well as dither instrumental features in wavelength space.

The COS FUV spectrum of HE0238-1904 (z= 0.6309) displays a variety of absorption features in part due to the interstellar medium in our galaxy (ISM); to a collection of intervening Lyman-alpha systems (IGM); and absorption features that are directly related to an intrinsic outflow from the quasar. Details of identification of absorption features and extraction of ionic column densities is detailed in Arav et al. (2013). Table 3.14 lists the measured ionic column densities.

Photoionization Analysis

The photoionization and thermal structure of an outflow depends on the spectral energy distribution (SED) incident upon the outflow. We developed an SED appropriate for HE 0238-1904 by matching the far-UV shape to the COS data and largely mimicking the standard MF87 SED (Mathews & Ferland, 1987) at other energies. Figure 3.16 shows this SED along

Table 3.14 Column densities for HE0238-1904

Ions	v_{A3} (10^{12} cm^{-2})	v_A (10^{12} cm^{-2})	v_A M12[a] (10^{12} cm^{-2})	v_B (10^{12} cm^{-2})	v_B M12[a] (10^{12} cm^{-2})
H I	$\in [50.9, 183]$	$\in [92.5, 225]$	≤ 315	$\in [165, 506]$	$\in [188, 612]$
N IV	$6.82^{+1.20}_{-1.13}$	$19.9^{+2.1}_{-2.1}$	21	$12.2^{+1.5}_{-1.4}$	20
O IV	$64.2^{+6.1}_{-5.9}$	$98.7^{+8.7}_{-8.2}$	147	$34.4^{+5.7}_{-5.1}$	≤ 28
O IV *	$49.5^{+7.0}_{-6.8}$	$94.0^{+10.4}_{-9.6}$	–	$28.0^{+6.3}_{-5.8}$	–
O VI (AOD)	161^{+7}_{-7}	$> 661^{+20}_{-19}$	695	748^{+23}_{-22}	877
O VI (PC)	309^{+46}_{-28}	$> 995^{+173}_{-41}$	–	1480^{+680}_{-83}	–
O VI (PL)	543^{+118}_{-83}	$> 2980^{+910}_{-140}$	–	4500^{+1190}_{-140}	–
Ne VIII (AOD)	420^{+15}_{-14}	1790^{+30}_{-30}	1830	1990^{+20}_{-20}	2520
Ne VIII (PC)	551^{+32}_{-26}	2560^{+1480}_{-80}	–	2940^{+100}_{-80}	–
Ne VIII (PL)	830^{+74}_{-62}	5330^{+1350}_{-110}	–	6220^{+1360}_{-140}	–
C III	< 6.96	< 27.4	–	< 12.3	–
N III	< 31.7	< 125	37	< 144	≤ 97
O III	< 33.6	< 94.7	–	< 66.3	–
S VI	< 5.69	< 13.5	–	< 27.1	–
Mg X	–	> 1690	773	> 2150	1250
O V	–	> 200	64	> 170	141

[a] Column densities reported in the analysis of the absorber in Muzahid et al. (2012).

with the MF87 SED for comparison. The bolometric luminosity for HE0238 BPL1 is $L_{bol} = 1.57 \times 10^{47}$ erg s^{-1}, and the emission rate of hydrogen ionizing photons is $Q_H = 8.75 \times 10^{56}$ s^{-1}.

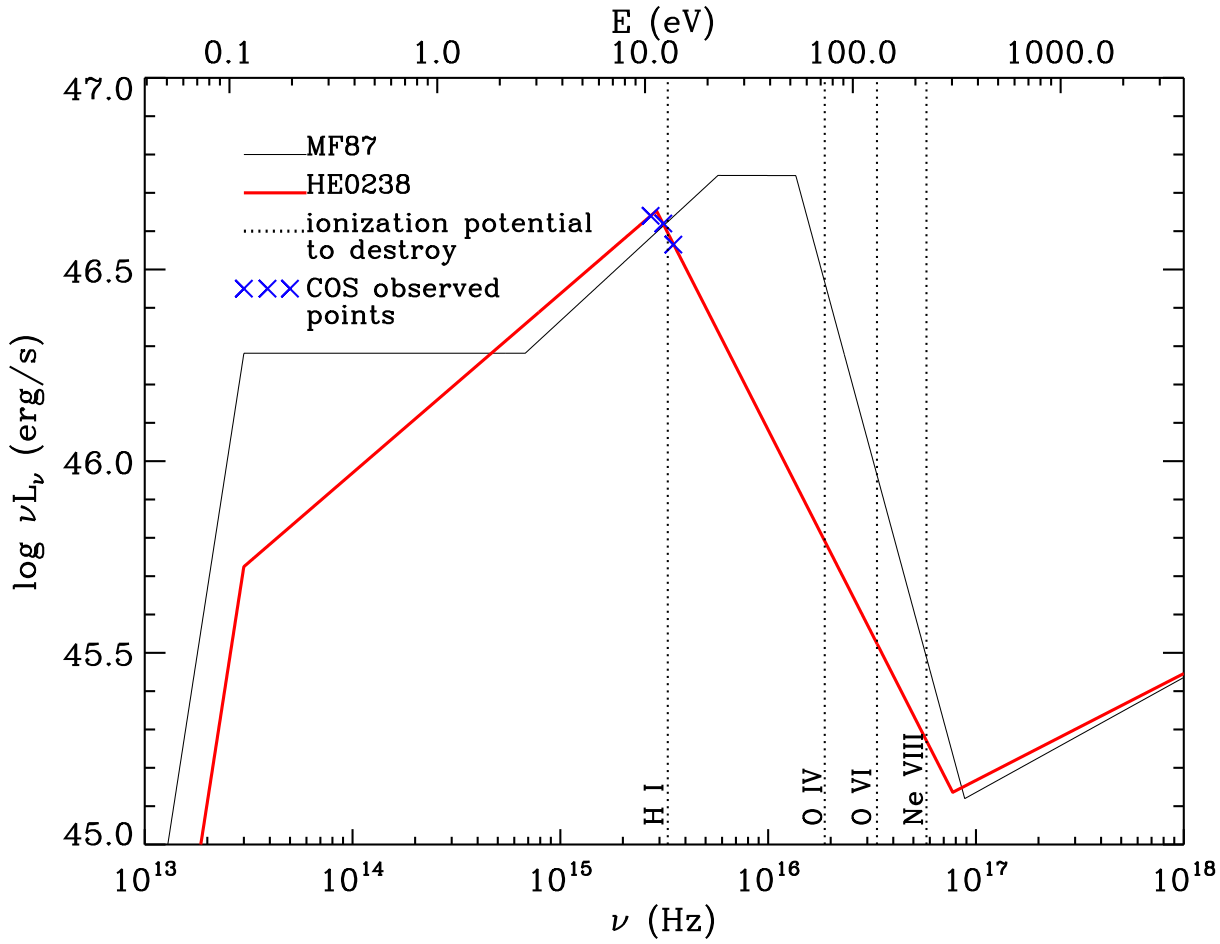

Figure 3.16 SED for HE 0238-1904. We developed this SED by matching the far-UV shape to the COS data and largely mimicking the MF87 SED at other energies.

We use version c08.00 of the spectral synthesis code CLOUDY (the code is described in Ferland et al. 1998), to determine the total hydrogen column density (N_H) and ionization parameter

$$U_H \equiv \frac{Q_H}{4\pi R^2 n_H c}, \tag{3.17}$$

for the absorber (where c is the speed of light, R is the distance to the absorber from the

central source, and n_H is the total hydrogen number density). We assume solar abundances as given in CLOUDY and a plane-parallel geometry for a gas of constant hydrogen number density and generate grids of models to investigate the parameter space (see Edmonds et al. 2011 for details). Figures 3.17, shows the results of this analysis for kinematic component A3. In this figure, lines where the tabulated ionic column densities (N_{ion}) match the measured values are plotted in the N_H-U_H plane. The bands reflect uncertainties in the measurements, and the dotted lines depict upper limits due to non-detection of the ions in the COS data.

We model three physically distinct components in trough A. In component A3, we identify O IV and O IV* allowing us to determine the electron number density in this component of the absorber. Part of the O IV* trough is blended with Lyϵ. Therefore, we first solve for the photoionization structure of the region of trough A3 that is not contaminated by Lyϵ. Once N_H and U_H are determined for this region, we solve the balance equations using column densities derived from the entire trough A and compare results. Finally, we model trough B using column densities derived from integrating over the entire trough.

To determine the maximum likelihood values for our model parameters, we minimize the function

$$\chi^2 = \sum_i \left(\frac{\log N_{i,mod} - \log N_{i,obs}}{\log N_{i,obs} - \log \left(N_{i,obs} \pm \sigma_i \right)} \right)^2 \tag{3.18}$$

where, for ion i, $N_{obs,i}$ and $N_{mod,i}$ are the observed and modeled column densities, respectively, and σ_i is the error in the measured column density. This formalism is preferable to the traditional χ^2 formalism since it preserves the multiplicative nature of the errors: For example, an overprediction of N_{ion} by a factor of 2 is on equal footing with an underprediction of N_{ion} by a factor of 2 (the traditional formalism considers a factor of 2 overprediction on equal footing with a prediction of zero). We note that in the limit that $\sigma << N_{obs}$ and $\left| \frac{N_{obs}}{N_{mod}} - 1 \right| << 1$, the formula above reduces to the traditional form of χ^2.

Photoionization structure of trough A

Figure 3.17 shows the results of photoionization modeling for component A. We use N_{ion} determined by the partial-covering method for O VI and Ne VIII. For N IV and O IV, we use AOD measurements. The upper and lower limits on H I are given by an upper limit on Lyγ and the AOD measurement of Lyβ, respectively, and the gray band depicts the region consistent with these limits. Since the uncertainties in column density determinations are asymmetric, the errors used in computing χ^2 are determined in part by the ratio of predicted N_{ion} to the measured value: For a ratio less/greater than unity, the lower/upper errors are used, except in the case of H I where models within the gray band do not contribute to χ^2. Upper limits are treated in the following way: Models below an upper limit do not contribute to χ^2, while the AOD uncertainties are used as errors for those above the upper limit.

We first attempt to fit the data with a single ionization parameter. The best-fit solution ($\chi^2_\nu \sim 360$) is marked in Figure 3.17 with box at $U_H \sim 1$ and $N_H \sim 10^{19.6}$. This model underpredicts O IV by a factor of ~ 4 and overpredicts O VI by a factor of ~ 6. More importantly, there is a separation O IV and O VI lines of ~ 1.4 dex, a separation unsupportable by the derived uncertainties as evidenced by the high value of χ^2_ν. Chemical abundances that deviate from solar values can often fix disparities between ions of different elements, but the ratio of O IV and O VI column densities is insensitive to changes in chemical abundances. Changes in SED can also cause changes in ionic column density ratios, especially for ions whose destruction potentials are appreciably different. However, the SED for HE0238-1904 is relatively well constrained in the UV ionizing region. We conclude that models with a single ionization parameter do not yield a physically acceptable fit the data.

The next simplest model to consider is one with two ionization parameters, in which we sum the contributions to the column denisity of each ion from two homogenous slabs with

independent N_H and U_H. This approach is similar to one used routinely in X-ray warm absorber studies (e.g., Detmers et al. 2011) In components A and A3, lines of constant N_{ion} for N IV and O IV are nearly parallel across the entire range of ionization parameters implying there may be deviations from solar abundances. Therefore, N IV is ignored in the computation of χ^2. We then have four constraints and four free parameters, so we cannot formally rely on χ^2 values (which tend toward zero) to tell us the most likely solution. However, we can use the formal method as a guide to determine a range of plausible solutions that minimize deviations from the observed values. To this end, we plot fifty solution pairs with the lowest values of χ^2. Figure 3.17 shows the results for trough A3, where we see that the all of the O IV comes from the low-ionization component (U1), all of the Ne VIII comes from the high-ionization component (U2), and both ionization components contribute to H I and O VI, although most of the O VI comes from component U2 when component U1 has $\log U_H \lesssim -1$. Ionization component U1 solutions follow O IV, since all of the O IV comes from the low-ionization absorber, and are constrained on the low end by the upper limit found for the column density of C III and on the high end by O VI: $-1.3 \lesssim \log U_H(1) \lesssim -0.8$; $17.7 \lesssim \log N_H(1) \lesssim 18.3$. Ionization component U2 solutions follow Ne VIII, since all of the Ne VIII comes from the high-ionization absorber. The column density of O VI constrains solutions from below, while an upper limit on the column density of H I constrains them from above: $0.5 \lesssim \log U_H(2) \lesssim 1.4$; $19.5 \lesssim \log N_H(2) \lesssim 22.1$.

In the above analysis, AOD column density measurements were used for O IV as well as the other lines from singlet transitions. In order to determine the effects on our solutions of a non-unity covering fraction for O IV, we solve for N_H and U_H after scaling the observed column density of O IV by the ratio of column denities of O VI determined by partial-covering and AOD methods. This affects only the low-ionization component (U1) since the line for O IV will move up in the $N_H - U_H$ plot while H I, O VI, and Ne VIII will stay in the same position.

We increase the column densities of the upper limits given by non-detection of C III and S VI by the same fraction. We find that the lower limit on $N_H(1)$ increases by ~ 0.3 dex, and the upper limit on $U_H(1)$ decreases by ~ 0.1 dex while the other values remain unchanged. Similarly, when N IV is allowed to contribute to χ^2, only component U1 is affected, with $N_H(1)$ decreasing by $\lesssim 0.2$ dex and the range in $U_H(1)$ increasing $-1.5 \lesssim \log U_H \lesssim -0.7$. Results of photoionization analysis for troughs A and B are given in Table 3.15.

Photoionization structure of trough B

As for trough A, we first attempt to fit the data with a single ionization parameter. The solution with the lowest value of χ^2 has $\log U_H \sim 0.2$ and $\log N_H \sim 20.2$. Four of the five detected ions have lines of solution in the N_H-U_H plane that cross near this point. The exception is O VI, which is overpredicted by a factor ~ 3. The separation between O IV and O VI can again be ameliorated by the use of two ionization parameters. We find the following range of solutions; $-0.4 \lesssim \log U_H(1) \lesssim -0.2, 18.9 \lesssim \log N_H(1) \lesssim 19.2$ and $1.0 \lesssim \log U_H(2) \lesssim 1.4, 21.0 \lesssim \log N_H(2) \lesssim 22.6$. Just as for trough A, we determine U_H and N_H using observed values integrated only over the part of the trough containing O IV*. The high-ionization component (U2) changed very little (less than 0.1 dex in either parameter), while the ionization parameter $U_H(1)$ decreased by 0.2 dex, and the total hydrogen column density $N_H(1)$ decreased by 0.5 dex.

Absorber Distance and Energetics

The distance to the absorber can be computed from the ionization parameter (see Equation (3.22)) if the total hydrogen number density n_H is known. In highly ionized plasma the hydrogen number density is related to the electron number density through $n_e \approx 1.2 n_H$. To

Table 3.15 Modeling Results for HE0238-1904

Metalicity (Z)	log U_H	log N_H (cm^{-2})	R (kpc)	$\dot{M}$ ($M_\odot$)	$\dot{E}_k$ (10^{45} erg s^{-1})	$\dot{E}_k/L_{bol}$ (%)
			Trough A			
$Z = 1Z_\odot$	$-1.4^{+0.7}_{-0.1}$	$20.6^{+0.1}_{-0.1}$	$1.0^{+0.3}_{-0.6}$	27^{+10}_{-15}	$0.52^{+0.20}_{-0.30}$	$0.35^{+0.10}_{-0.20}$
$Z = 4Z_\odot$	$-2.0^{+0.1}_{-0.4}$	$19.8^{+0.2}_{-0.1}$	$2.0^{+1.2}_{-0.3}$	$9.3^{+8.0}_{-2.0}$	$0.18^{+0.10}_{-0.04}$	$0.12^{+0.10}_{-0.02}$
			Trough B			
$Z = 1Z_\odot$	$-2.4^{+2.0}_{-0.1}$	$20.8^{+0.1}_{-0.2}$	$3.0^{+0.9}_{-2.8}$	160^{+80}_{-150}	$5.3^{+3.0}_{-5.0}$	$3.5^{+1.7}_{-3.0}$
$Z = 4Z_\odot$	$-2.5^{+0.1}_{-0.4}$	$20.0^{+0.1}_{-0.1}$	$3.4^{+2.0}_{-0.5}$	31^{+20}_{-9}	$1.0^{+0.7}_{-0.3}$	$0.7^{+0.5}_{-0.2}$

Notes. Ionization paramters (U_H) are from the low-ionization component. Since the high-ionization and low-ionization components are cospatial, N_H is from the high-ionization component.

determine n_e for trough A, we use the measured $N(O\,iv*)/N(O\,iv)$ ratio in trough A3 (the portion of trough A where the excited state appears) and similarly for trough B. We find a number density of log (n_H)= 3.75±0.10 cm^{-3} for trough A and log (n_H)= 3.79±0.17 cm^3 for trough B. We note that both troughs have the same number density within the measurement error.

In order to estimate the mass, mass flow rate, and kinetic luminosity of the outflow, we must assume a geometry. Given the large distance to the outflow, it is reasonable to assume it has the geometry of a thin, partially-filled shell (see Arav et al. 2011) with the mass then given by

$$M_{out} = 4\pi\mu m_p R^2 N_H \Omega \tag{3.19}$$

where $\mu = 1.4$ is the mean atomic mass per proton, m_p is the mass of the proton, and Ω is the covering fraction of the outflow as seen from the central source. We adopt the value $\Omega = 0.5$ based on the estimated intrinsic fraction of BAL quasars given by Hewett & Foltz (2003) for their sample. A comprehensive discussion of covering fraction for quasar outflows is given in Dunn et al. (2010b). The average mass flow rate is just the total mass divided by

the dynamical timescale R/v:

$$\dot{M}_{out} = 4\pi\mu m_p R N_H v \Omega \tag{3.20}$$

and the kinetic luminosity is given by

$$\dot{E}_k = \frac{\dot{M}_{out} v^2}{2} \tag{3.21}$$

Computed values are given in Table 3.15.

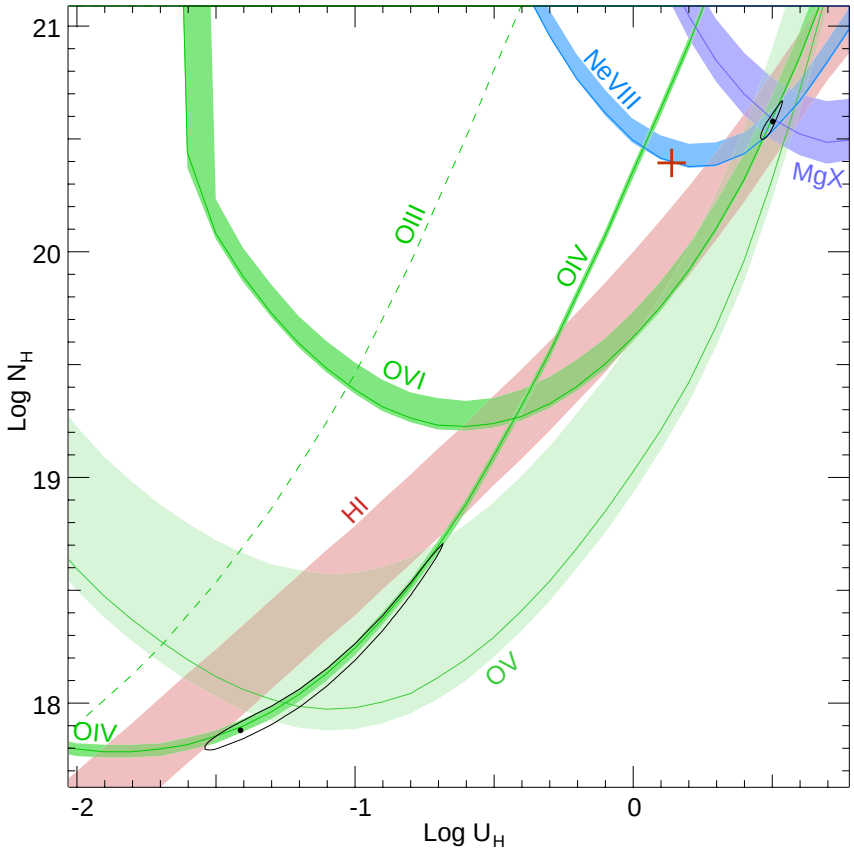

Figure 3.17 Phase Plot showing the ionization solutions for trough A assuming solar metallicity. Each colored contour represents the locus of models (U_H, N_H) that predict a column density consistent with the observed column density for that ion. The bands which span the contours are the 1-σ errors in the measurements. The dashed line indicates the O III upper limit. The red cross is the single-phase solution, while the black dots are the two-phase solutions and are surrounded by χ^2 contours.

3.2 Density from Time-varibility

3.2.1 Markarian 509

*All sections pertaining to Markarian 509 are published in Arav et al. (2012) and are reproduced here with permission of ESO.

Photoionization Solutions for the Different Outflow Components of Mrk 509

Our distance determinations rely on knowledge of the ionization parameter, which we find by solving the photoionization and thermal equilibrium equations self-consistently using version c08.00 of the spectral synthesis code CLOUDY (last described by Ferland et al. 1998). We use the spectral energy distribution (SED) described in Paper I and assume a plane-parallel geometry, a constant hydrogen number density, and solar abundances as given in CLOUDY. These abundances differ from those of Lodders & Palme (2009) (see Table 3.16) used in Paper VIII, but the differences do not significantly affect our results. Grids of models are generated where the total hydrogen column density (N_H) and the ionization parameter (U_H) are varied in 0.1 dex steps (similar to the approach of Arav et al. 2001; Edmonds et al. 2011) for a total of ∼4500 grid points covering a parameter space with $15 \leq \log N_H \leq 24.5$ and $-5 \leq \log U_H \leq 2$. Intermediate values are estimated by a log interpolation. At each point of the grid, we tabulate the predicted column densities (N_{ion}) of all relevant ions and compare them with the measured column densities (see Table 3.17). Our solutions are based only on C IV and N V (except for trough T5 discussed below). These lines cross at a single point in the N_H, U_H plane yielding a unique solution. The results for both COS and STIS data are given in Table 3.18. For most components, the differences in $\log N_H$ and $\log U_H$ between the four determinations (AOD and PC for both COS and STIS) are around 0.1–0.2 dex,

Table 3.16 Chemical Abundances used in Mrk 509

Element	CLOUDY[a]	LODDERS 2009[b]
He	-1.00	-1.07
C	-3.61	-3.61
N	-4.07	-4.14
O	-3.31	-3.27
Ne	-4.00	-3.95
Mg	-4.46	-4.46
Si	-4.46	-4.47
S	-4.74	-4.84
Fe	-4.55	-4.54

Notes. Abundances are given in log relative to hydrogen with log[A(H)]=0.00.
[a] Abundances as given in CLOUDY used in this paper.
[b] Lodders & Palme (2009) abundances used in Paper VIII.

and therefore do not affect our distance limits. The exception is component T1 where the AOD and PC determinations are significantly different due to the saturation of C IV. We obtain a photoionization solution for T1 by determining the upper limit on N(Si IV) along with the lower limit on N(C IV) and the measurement of N(N V). In the last two columns of Table 3.18, we give the fractional difference in column densities expected if the number density were high enough for the absorber to be in photoionization equilibrium at the time of the COS observations.

In trough T5, Si IV is detected in addition to C IV and N V. Kraemer et al. (2003) concluded that two ionization parameters are needed to match the observational constraints for this trough (their component 4) under the assumption of solar abundances. Two models are presented in Table 3.18 for trough T5, one for each ionization component. The high ionization model fitting C IV and N V underpredicts Si IV by a factor of ~ 10 which is ameliorated by

Table 3.17 Computed Column Densities

		AOD				PC			
Trough	Ion	C[a]	S[b]	C-S	(C-S)/C	C	S	C-S	(C-S)/C
T1	N(C IV)	> 47.1	> 39.0	···	···	> 135	> 101	···	···
T1	N(N V)	64.8±0.8	48.6±5.0	16.2	0.25±0.08	86.4±1.5	$70.7^{+18}_{-8.7}$	15.8	$0.18^{+0.21}_{-0.10}$
T2	N(C IV)	227±1	252±8	-25	-0.11±0.03	264±1	288^{+54}_{-13}	-24.0	$-0.09^{+0.20}_{-0.05}$
T2	N(N V)	201±1	215±10	-14	-0.07±0.05	225±1	254^{+480}_{-13}	-28.4	$-0.13^{+2.1}_{-0.06}$
T3	N(C IV)	56.0±0.4	61.4±3.4	-5.4	-0.10±0.06	68.9±0.7	67.9±3.9	1.0	0.01±0.06
T3	N(N V)	62.2±0.8	64.6±5.6	-2.5	-0.04±0.09	78.0±1.2	$84.5^{+670}_{-8.9}$	-6.5	$-0.08^{+8.6}_{-0.16}$
T4	N(C IV)	64.1±0.5	71.4±3.4	-7.3	-0.11±0.05	72.7±0.5	76.5±3.1	-3.8	-0.05±0.04
T4	N(N V)	84.7±0.9	78.5±5.4	6.1	0.07±0.06	$92.7^{+38}_{-0.8}$	$91.2^{+8.4}_{-6.4}$	1.5	$0.02^{+0.42}_{-0.07}$
T5	N(C IV)	197±1	211±10	-13	-0.07±0.05	264±4	266^{+69}_{-13}	-2.0	$-0.01^{+0.26}_{-0.05}$
T5	N(N V)	299±2	272^{+22}_{-14}	28	$0.09^{+0.08}_{-0.05}$	356±5	346^{+2500}_{-34}	10.2	$0.03^{+6.9}_{-0.10}$
T5	N(Si IV)	2.7±0.2	$4.6^{+1.4}_{-1.0}$	-2.0	$-0.74^{+0.54}_{-0.38}$	$2.8^{+21}_{-0.1}$	$9.5^{+43}_{-1.9}$	-6.7	$-2.5^{+31}_{-0.7}$
T6	N(C IV)	28.2±0.4	28.9±2.7	-0.7	-0.03±0.10	33.7±0.5	$35.3^{+5.6}_{-3.4}$	-1.6	$-0.05^{+0.17}_{-0.10}$
T6	N(N V)	50.6±0.8	48.4±4.9	2.3	0.04±0.10	54.8±0.7	53.6±3.8	1.2	0.02±0.07
T7	N(C IV)	24.9±0.4	27.7±2.8	-2.8	-0.11±0.12	···	···	···	···
T7	N(N V)	64.4±0.5	66.7±4.5	-2.3	-0.04±0.07	96.8±2.3	$69.0^{+360}_{-5.9}$	27.9	$0.29^{+3.8}_{-0.06}$
T8	N(C IV)	< 3.7	< 5.2	···	···	···	···	···	···
T8	N(N V)	16.8±0.6	16.6±3.6	0.1	0.01±0.22	21.3±0.8	$24.2^{+290}_{-7.9}$	-2.9	$-0.14^{+14}_{-0.37}$
T9	N(C IV)	< 4.2	< 4.9	···	···	···	···	···	···
T9	N(N V)	17.4±0.7	21.9±4.2	-4.5	-0.26±0.25	20.5±0.5	$34.0^{+150}_{-9.4}$	-13.5	$-0.66^{+32}_{-0.46}$

[a] N_{ion} in units of 10^{12} cm^{-2} measured from the 2009 COS observations. All errors are statistical only.
[b] N_{ion} in units of 10^{12} cm^{-2} measured from the 2001 STIS observations.

the addition of a lower ionization component fitting Si IV. Summation of the predicted column densities for the two ionization components results in an overprediction of C IV by a factor of 2. The solution is improved by increasing U_H and N_H of the high ionization component resulting in a band of solutions with $\log U_H \gtrsim -1.0$. These models predict all of the Si IV and C IV come from the low ionization component, while N V comes from the high ionization component. Our results differ from those of Kraemer et al. (2003), especially in the low ionization component, where they find about 10 times larger N_H than we do. They find such a large value by assuming a low covering of the emission source by Si IV. With higher S/N COS data, however, we find a covering near unity. We assume the high and low ionization components are at the same location, an assumption supported by the kinematic correspondence of all three troughs, and use the low ionization component solution to provide a lower limit on the distance.

It is also possible to find a single ionization parameter solution for component T5 if the assumption of solar abundances is relaxed. We find that increasing the abundances of nitrogen and silicon relative to carbon by a factor of 2 results in a model that accurately predicts the column densities of C IV, N V, and Si IV, with $\log U_H = -1.5$, and $\log N_H = 18.7$, values close to the low ionization component discussed above. However, Steenbrugge et al. (2011, Paper VII) used *XMM-Newton* and *Chandra* data to show that the abundances for C, N, and Si are consistent with the proto-solar abundances determined by Lodders & Palme (2009), and the ratio of nitrogen to carbon abundances is less than 30% higher than the solar ratio.

For each kinematic component (except T5), we find a satisfactory fit to the data with a single ionization component. This differs from the X-ray analysis in Detmers et al. (2011, hereafter Paper III) where some ions are formed by multiple ionization components. However, since the velocities are not resolved in the X-ray spectra, this does not necessarily imply disagreement between the X-ray and UV analysis. A comprehensive comparison of the UV and X-ray data

Table 3.18 Photoionization Models for Mrk 509

	COS				STIS				$\frac{\Delta N_{ion}}{N_{ion}(\mathrm{STIS})}$ [a]	
	AOD		PC		AOD		PC			
Trough	log U_H	log N_H (cm^{-2})	log U_H	log N_H (cm^{-2})	log U_H	log N_H (cm^{-2})	log U_H	log N_H (cm^{-2})	C IV	N V
T1	-1.1	18.5	-1.5	18.5	-1.2	18.3	-1.5	18.4	-0.51	-0.17
T2	-1.4	18.8	-1.4	18.9	-1.4	18.9	-1.3	19.0	-0.55	-0.28
T3	-1.2	18.4	-1.2	18.6	-1.3	18.4	-1.1	18.7	-0.57	-0.35
T4	-1.1	18.6	-1.1	18.6	-1.2	18.5	-1.2	18.6	-0.60	-0.41
T5(high)[b]	-1.0	19.2	-1.1	19.2	-1.1	19.1	-1.1	19.2	-0.62	-0.48
T5(low)	-1.6	18.6	-1.5	18.2	-1.8	18.4	-1.5	18.2	-0.41	+0.26
T6	-0.9	18.6	-0.9	18.6	-0.9	18.5	-0.9	18.8	-0.68	-0.56
T7[c]	-0.5	19.2	···	···	-0.8	18.8	···	···	-0.72	-0.59
Total N_H	···	19.8	···	19.6	···	19.6	···	19.7		

Notes. Troughs T8 and T9 have heavy blending in the blue component of C IV, and the red component of C IV is very weak. We therefore do not include ionization analysis of these troughs.

[a] Fractional changes in column density expected if the number density were high enough for the absorber to be in equilibrium at the time of the COS observations.

[b] Lower limits. Summation of low and high ionization components for trough T5 overpredicts C IV by a factor of 2, which is ameliorated by increasing U_H of the high ionization component. Since all of the C IV comes from the low ionization component, we use the lower ionization parameter to compute lower limits on the distance for this trough.

[c] Heavy blending in the blue component of C IV precludes partial covering measurements for trough T7.

Table 3.19 Initial Values

Trough	α(C III)	α(C IV)	log N(C IV)	log N(C V)	α(N IV)	α(N V)	log N(N V)	log N(N VI)
	(10^{-12} cm^3 s^{-1})		(cm^{-2})		(10^{-12} cm^3 s^{-1})		(cm^{-2})	
T1	23.9	5.86	14.1	14.8	28.0	10.8	14.0	13.9
T2	24.5	5.66	14.3	15.1	28.2	10.3	14.3	14.3
T3	26.4	5.26	13.7	14.7	28.9	9.40	13.8	14.1
T4	27.6	5.07	13.8	14.9	29.5	9.00	13.9	14.3
T5(low)	23.3	6.09	14.1	14.8	27.9	11.3	14.1	13.9
T6	30.8	4.67	13.5	14.8	31.4	8.23	13.7	14.4
T7	41.1	3.73	13.4	15.2	39.7	6.53	13.9	15.0

Notes. Using N_H and U_H derived from the 2009 COS data (see text) using the AOD method except for component T1 where we use values from the PC method due to the saturation of C IV.

is deferred to a future paper (Ebrero et al. 2012, in preparation).

Time-dependent Ionization Equations

The ionization parameter

$$U_H \equiv \frac{Q_H}{4\pi R^2 n_{_H} c} \tag{3.22}$$

(where Q_H is the rate of hydrogen ionizing photons emitted by the central source, c is the speed of light, R is the distance to the absorber from the central source, and $n_{_H}$ is the total hydrogen number density) characterizes a plasma in photoionization equilibrium. When the ionizing flux varies, the ionization state of the gas will change in response if the timescale for flux variations is an appreciable fraction of the recombination timescale for the gas. The latter depends on the electron number density (n_e), which is $\simeq 1.2 n_{_H}$ in highly ionized plasma. Gases of high density will respond faster than gases of low density due to a higher collision rate between free electrons and ions (e.g., Krolik & Kriss 1995; Nicastro et al. 1999; Paper VIII). If the gas has not had time to reach ionization equilibrium, determination of U_H by line ratios suffers from uncertainties since it is inappropriate to use the assumption of photoionization equilibrium. As we show in the appendix, in that case, the ionization state of the gas will be more accurately derived by using the average Q_H over a timescale roughly equal to the recombination timescale of the ion in question. Tracking changes in column density of a given ion between different epochs along with flux monitoring can lead to estimates of $n_{_H}$ and thereby, the distance R (e.g., Gabel et al. 2005a) assuming that changes in the hydrogen number density between epochs is negligible.

The abundance of a given element in ionization stage i is given by

$$\frac{dn_i}{dt} = -n_i(I_i + R_{i-1}) + n_{i-1} I_{i-1} + n_{i+1} R_i, \tag{3.23}$$

as a function of the ionization rate per particle, I_i, and the recombination rate per particle

from ionization stage $i+1$ to i, R_i. We have neglected Auger effects, collisional ionization, and charge transfer (e.g., Krolik & Kriss 1995). If the gas at distance r from an ionizing source of monochromatic luminosity L_ν is optically thin, as in Mrk 509, the ionization rate per particle is given by

$$I_i = \int_{\nu_i}^{\infty} \frac{(L_\nu/h\nu)\sigma_\nu}{4\pi r^2} d\nu, \tag{3.24}$$

where h is Planck's constant and σ_ν is the cross-section for ionization by photons of energy $h\nu$. The recombination rate per particle is given by

$$R_i = \alpha_i(T) n_e. \tag{3.25}$$

The recombination coefficient α depends on the electron temperature T and scales roughly as $T^{-1/2}$ (Osterbrock & Ferland, 2006).

Equation 3.23 forms a set of $n+1$ coupled differential equations for an element with n electrons and $n+1$ ions. In the steady state, these reduce to n equations of the form

$$\frac{n_{i+1}}{n_i} = \frac{I_i}{R_i}. \tag{3.26}$$

Closure of the steady state set of equations is given by $\sum n_i = n_{tot}$, where n_{tot} is the total number density of the element in question. Under these assumptions the level of ionization of the gas in photoionization equilibrium may be characterized by I_i/R_i, which is proportional to the ratio of ionizing flux to n_e and leads to the definition of ionization parameter given in Equation 3.22.

Simple scaling of Equation 3.23 leads to a characteristic timescale. Suppose an absorber in photoionization equilibrium experiences a sudden change in the incident ionizing flux such that $I_i(t>0) = (1+f)I_i(t=0)$, where $-1 \leq f \leq \infty$. Then taking the ratio $dn_i/dt \rightarrow n_i/t$

leads to the timescale for change in the ionic fraction:

$$t^* = \left[-f\alpha_i n_e \left(\frac{n_{i+1}}{n_i} - \frac{\alpha_{i-1}}{\alpha_i} \right) \right]^{-1}. \tag{3.27}$$

Note that the timescale defined here equals the recombination timescale of Krolik & Kriss (1995) when $f = -1$, i.e., the ionizing flux drops to zero (see also Nicastro et al. 1999; Bottorff et al. 2000; Steenbrugge et al. 2009). Including the ionizing flux in t^* gives more accurate timescales in cases where the ionizing flux either changes by small amounts ($|f| \ll 1$) or increases by a large amount. The recombination coefficients are obtained for each of our photoionization models using the CLOUDY command "`punch recombination coefficients`". The initial values needed to compute recombination times for C IV and N V for troughs T1 through T7 are given in Table 3.19. We compute t^* for reference (see Table 3.20), but the distance determinations discussed in Section 3.2.1 are from explicit solutions of the time-dependent photoionization equations using simulated lightcurves, not timescale arguments. We use the values derived from the 2009 COS data since the higher S/N allows for better constraints than the 2001 STIS data, and the photoionization solutions are similar for both data sets (see Table 3.18). Results for troughs T8 and T9 are not given due to heavy blending in the blue component of C IV and very weak lines in the red component precluding reliable photoionization solutions.

It is common to use the recombination timescale ($-ft^*$; e.g. Krolik & Kriss 1995; Bottorff et al. 2000; Netzer 2008) when determining limits on the number density of an AGN outflow. For large increases in flux, the ionization timescale (I_i^{-1}) has been invoked (e.g. Dunn et al. 2010a). Use of our refined timescale (Equation 3.27) allows us to treat both increases and decreases in flux for any ion and account for finite flux changes in a natural way.

For the Mrk 509 UV data, there are two physically motivated timescales we can use in

Table 3.20 Timescales per Electron Number Density

Trough	$-fn_e t$(CIV) (10^{10} cm^{-3} s)	$-fn_e t$(NV) (10^{10} cm^{-3} s)
T1	18.3	-5.15
T2	8.92	-5.59
T3	3.82	-9.86
T4	2.76	-14.5
T5(low)	13.8	-4.81
T6	1.60	10.2
T7	0.51	2.35

Notes. The numbers in this table are the product of t^* from Equation 3.27 and $-fn_e$. To get a timescale for a given n_e and flux change f, we divide the number in the table by $-fn_e$. For example, given $n_e = 10^3$ cm^{-3} (typical for the upper limits derived in Section 5) and $f = 0.72$ (the flux at the COS epoch minus that at the STIS epoch), t^*(C IV)$\sim$ 1.7 yr for component T3. Note that the numbers in this table are positive or negative depending on whether the change in ionic fraction is anti-correlated or correlated with a drop in ionizing flux, respectively (see also Bottorff et al. 2000).

Equation (3.27): 1) assuming an instantaneous increase in flux just after the STIS epoch that stays constant through the COS epoch ($t^* = 8$ years and $f = 0.72$ for this case); and 2) assuming a constant flux at the STIS epoch level until the 100 days monitoring prior to the COS observations followed by an instantaneous flux increase to the COS flux level thereafter, ($t^* = 100$ days and $f = 0.72$ for this case). Using the appropriate ionization equilibrium for each component, we derive upper limits on the number density for each of these cases (see columns 3 and 5 of Table 3.21). Due to the difference in timescales, the first case yields upper limits that are a factor of 30 smaller than the second case. We then use Equation 3.22 to derive the associated lower limits on the distance to the absorbers from the central source (see columns 4 and 6 of Table 3.21)

However, there are several limitations when using timescale arguments in order to infer the number density (or limits thereof) of the absorber. First, timescale analysis implicitly relies on the physically implausible lightcurves discussed above. As we show in Section 5, a more physically motivated approach is to use lightcurve simulations that are anchored in our knowledge of the power spectrum behavior of observed AGN lightcurves.

Second, timescale analysis does not take into account the quality of measurement. This is especially important for cases where no changes in column density are observed. We expect that tighter error bars on no-change measurements would yield smaller upper limits on the absorber's n_e. To correct the timescale inferred n_e values for this effect we use the following approach. For the simple lightcurve associated with the 100 days timescale, we numerically solve equation set 3.23, while requiring that changes in ionic column densities are less than the 1-σ errors from Table 2. The resulting limits on n_e and R are given in columns 7 and 8 of Table 3.21, designated n_e3 and $R3$. We note that we are able to put a range on the density for T1 and T2 due to the observed change in column density for these components.

Table 3.21 Density and Distance Limits from Timescale Calculations

Trough	v (km s^{-1})	log n_e1 (cm^{-3})	$R1$ (pc)	log n_e2 (cm^{-3})	$R2$ (pc)	log n_e3 (cm^{-3})	$R3$ (pc)
T1	-405	<2.4	>460	<3.9	>80	3.0–3.7	100–230
T2	-310	<2.4	>400	<3.9	>70	2.9–3.1	180–230
T3	-240	<2.3	>350	<3.7	>70	<2.7	>220
T4	-70	<2.1	>400	<3.6	>70	<2.6	>230
T5	-15	<2.4	>490	<3.8	>100	<3.6	>120
T6	+45	<1.9	>430	<3.4	>80	<1.8	>480
T7	+125	<1.4	>480	<2.9	>90	<1.9	>270

Notes. Timescales are derived from C IV for all troughs except T1, for which we use N V. While troughs T1 and T2 show change, the limits on number density derived from timescale arguments are upper limits since photoionization models imply the absorbers are not in equilibrium.

Third, use of Equation 3.27 can lead to problems when used for ions near their maximum concentration and should be avoided in these cases. As discussed in Paper VIII, ions near their maximum concentration are relatively insensitive to ionizing flux changes. In these cases, using Equation 3.27 can result in a large overestimation of the electron number density. For example, for an electron number density of 1900 cm^{-3}, the C IV timescale for trough T2 is ~ 5 times larger than the e-folding time determined by solving Equation 3.23 numerically.

Monte Carlo Simulations of Absorption Trough Changes

As mentioned above, timescale analysis implicitly relies on physically implausible lightcurves. This could be justified if these lightcurves resulted in "conservative" or "robust" limits on n_e. However, designating the 100 days timescale lightcurve (see section 4) as case A, we give examples of two cases that give larger upper limits on n_e:

Case B: The UV flux dropped to a very low state (say, 1% of the STIS flux level) shortly after the STIS epoch and instantaneously jumped to the COS level 100 days prior to that

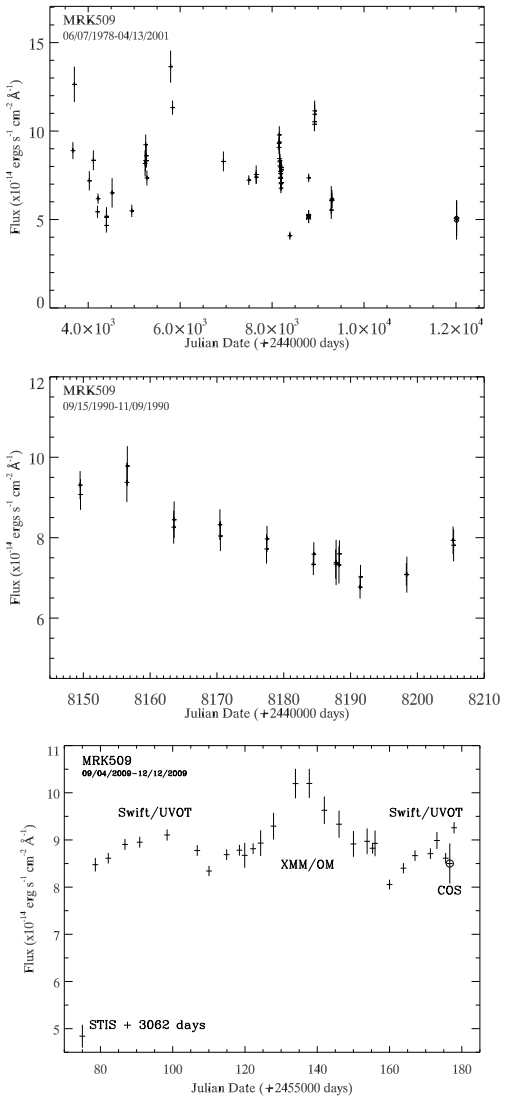

Figure 3.18 MRK 509 UV lightcurve monitoring at 1401 Å. The top panel shows all the UV flux monitoring observations of Mrk 509 prior to our campaign. Even in this sparse sampling, it is clear that the UV lightcurve of Mrk 509 changes by at least a factor of 3.5. The center panel gives a blow-up of the only intensive short-term monitoring (September-November 1990) before our campaign. The characteristics of this intensively monitored lightcurve are similar to the one we measured during our 2009 campaign shown in the bottom panel, where the COS observation is marked with a circle.

epoch (the time period for which we have monitoring). In this case the resulting n_e will be larger than in Case A. For example, solving Equation 3.23 with this lightcurve results in n_e

that is larger by a factor of 5 for kinematic component T2.

Case C. The flux level before the STIS measurement was similar to the one measured at the COS epoch and dropped suddenly just before the STIS observation, returning to the COS level shortly after the STIS epoch. In this case, we lose any distance information since no change in column density is expected and thus the electron number density could be arbitrarily high.

However, historical UV monitoring data of both Mrk 509 (see figure 3) and other nearby AGN clearly show that all 3 cases discussed above are highly unlikely. We therefore use a different approach to assess the limits on n_e from the available data and the well studied power spectrum behavior of AGN lightcurves. Using this information, we are able to produce representative simulated lightcurves that allow us to derive the (physical) statistical constraints on the upper limits for the number density of the outflow and therefore lower limits on the distance. This method also offers inherent improvements on traditional timescale analysis by accounting for the physical behavior AGN lightcurves and the quality of measurement in cases where no changes are observed in the absorption troughs (see second limitation of timescale analysis in section 4). We will show in section 6 that the two simple applications of the timescale described in the previous section are similar to and also bracket the statistical limits we obtain in this section.

There was no monitoring of the lightcurve of Mrk 509 between the STIS observation in 2001 and our 2009 multiwavelength campaign. However, we can use the prior history of UV and optical monitoring of Mrk 509 to establish the expected character of any variations that might have occurred. In general, the optical and UV continua show variations that are well characterized by a power-law power density spectrum $P(f) \propto f^{-\alpha}$, with spectral indices in the range of 1 to 2.5 (White & Peterson, 1994; Peterson et al., 1998; Collier & Peterson, 2001; Horne et al., 2004). Collier & Peterson (2001) analyzed ground-based optical

monitoring data for Mrk 509 as part of a study to characterize the optical and UV continuum variations of AGN. For 1908 days of monitoring at 10 to 100 day intervals, they established that the power density spectrum of Mrk 509 has a spectral index of $\alpha = 2.06 \pm 0.14$. To see what such variations over the 8 years between the STIS and COS observations might imply for changes in the UV-absorbing gas, we perform a Monte Carlo simulation to generate a set of 1000 light curves using the variability characteristics of Mrk 509. To generate these simulated light curves, we follow the procedure described by Peterson et al. (1998) and Horne et al. (2004). We first construct a power density spectrum with a spectral index randomly drawn from a Gaussian distribution with a mean $\alpha = 2.0$ and a dispersion of 0.5. Since the power density spectrum is the Fourier pair of the autocorrelation function, taking the square root of this distribution then gives the Fourier amplitudes of the light curve. As described by Peterson et al. (1998), a random lightcurve can then be generated by assigning random phases to these amplitudes and then taking the inverse Fourier transform. To normalize the mean flux and fractional variations in this light curve, we use the historical UV data for Mrk 509 compiled by Dunn et al. (2006, see our Figure 3.18), updated with our new COS observation. For these data, binned to 200-day timescales, we measure a mean flux at 1401 Å of 7.04×10^{-14} ergs cm^{-2} s^{-1} Å^{-1} and a fractional variation $F_{var} = 0.29$ (where F_{var} is as defined by Rodriguez-Pascual et al. 1997).

We solve the coupled time-dependent differential equations (Equation 3.23) for a given element numerically using the 4th order Runge-Kutta method. The initial recombination coefficients ($\alpha_X(T)$) and column densities (see Table 3.19) are taken from the best-fit CLOUDY models with parameters given in Table 3.18 for each trough. We compute ionization rates using Equation 3.26. We do not use the ionization rates provided by CLOUDY since those rates do not result in equilibrium using the simplified formalism that leads to Equation 3.26 (see also Paper VIII). In previous papers (Mehdipour et al. 2011, hereafter Paper IV; Pa-

per VIII), we have shown that flux variability in the optical, ultraviolet, and soft X-rays in Mrk 509 is highly correlated, which gives us confidence that the portion of the SED most important for the ionization of C IV and N V maintains a constant shape even as the overall normalization varies. We therefore assume that the SED maintains a constant shape for the entire time period. The simulated lightcurves, discussed above, extend over a period of 22 years. From those lightcurves, we select the ones that have a flux value at t_2 that is approximately 70% higher than that at t_1, where $t_2 - t_1 = 8$ yr (the time between the STIS and COS epochs). We use the simulated lightcurve only in the interval $t_1 < t < t_2$ in order to match the measured flux levels in the 2001 and 2009 epochs. From the 1000 original lightcurves, 928 contain regions that fit these criteria. Since 7 of the 928 lightcurves have two 8 yr periods separated by at least 6 months that fit our criteria, we have a sample of 935 lightcurves.

UV flux monitoring of the 100 days before the COS observations (Paper IV, Figure 2) reveals that the quasar continuum over that time interval was always at least 70% above that during the 2001 STIS epoch (Fig. 3, bottom panel). We therefore fix the last 100 days of all the lightcurves in our sample to be constant at $\simeq 1.72$ times the STIS value as a conservative estimate for the flux change.

For our initial conditions at the STIS 2001 epoch, we assume that the absorber was in photoionization equilibrium at that time. As can be seen in the top panel of Fig. 3.18, there is gap of several years between the STIS observation (the last point on the plot) and the previous IUE monitoring. We therefore have limited information about the lightcurve behavior prior to the 2001 epoch. However, both Fig. 3.18 (center panel) and our 2009 UV monitoring (bottom panel) suggest that the Mrk 509 UV flux changes gradually over timescales of 50-100 days. In the center panel of Fig. 3.18, the flux varies by a maximum of $\sim 40\%$, while our 2009 UV monitoring reveals maximum flux changes of $\sim 30\%$ (also see

Paper IV, Figure 2). Therefore, it is plausible that the UV flux in the 100 or so days before the STIS epoch was similar to that of the actual measurement during the 2001 observing epoch. Moreover, we note that FUSE observations in 1999 and 2000 show that the flux at 1175Å was within 10% of that for the STIS observations (see Table 2 in Paper VI). These two additional lightcurve points suggest that the low flux state of Mrk 509 probably existed in the two years prior to the 2001 STIS epoch. Under this assumption, as long as the recombination timescale is shorter than 2 years, we can use the photoionization equilibrium assumption. For lower density plasma ($n_e \lesssim 10^3$, see table 5) the plasma cannot be approximated as being in photoionization equilibrium even if the flux was constant for the previous two years. However, $n_e \simeq 10^3$ is roughly the upper limit we obtain from the full time-dependent solution for most components (see Table 3.22). A plasma with a lower n_e will be at a larger distance than the lower limits we derive in this paper and thereby, consistent with our results.

To determine an upper limit on the electron number density, we simulate the time-dependent changes in column densities of C IV and N V and compare them with the limits imposed by the observed differences between the STIS and COS data (see Table 3.17). For each given n_e, we track the fractional change in N(C IV) and N(N V) for all 935 simulated lightcurves in each of the seven troughs for which we have an initial photoionization solution. In Fig. 3.19, simulations for C IV and N V for two different electron number densities are shown for one of the simulated lightcurves with $t = 0$ corresponding to the STIS epoch and $t \simeq 8$ yr corresponding to the COS epoch. From the simulations, histograms of the fraction of simulations versus the predicted change in column density are produced for each ion in each trough. We choose the upper limit on n_e as the lowest density for which more than 99% of the lightcurves predict changes greater than those suggested by the data. Figure 3.20 shows an example of the resulting histograms, and Table 3.22 lists the results for each trough and ion.

Of components T1–T7, only T1 and T2 show a significant change in column densities. C IV

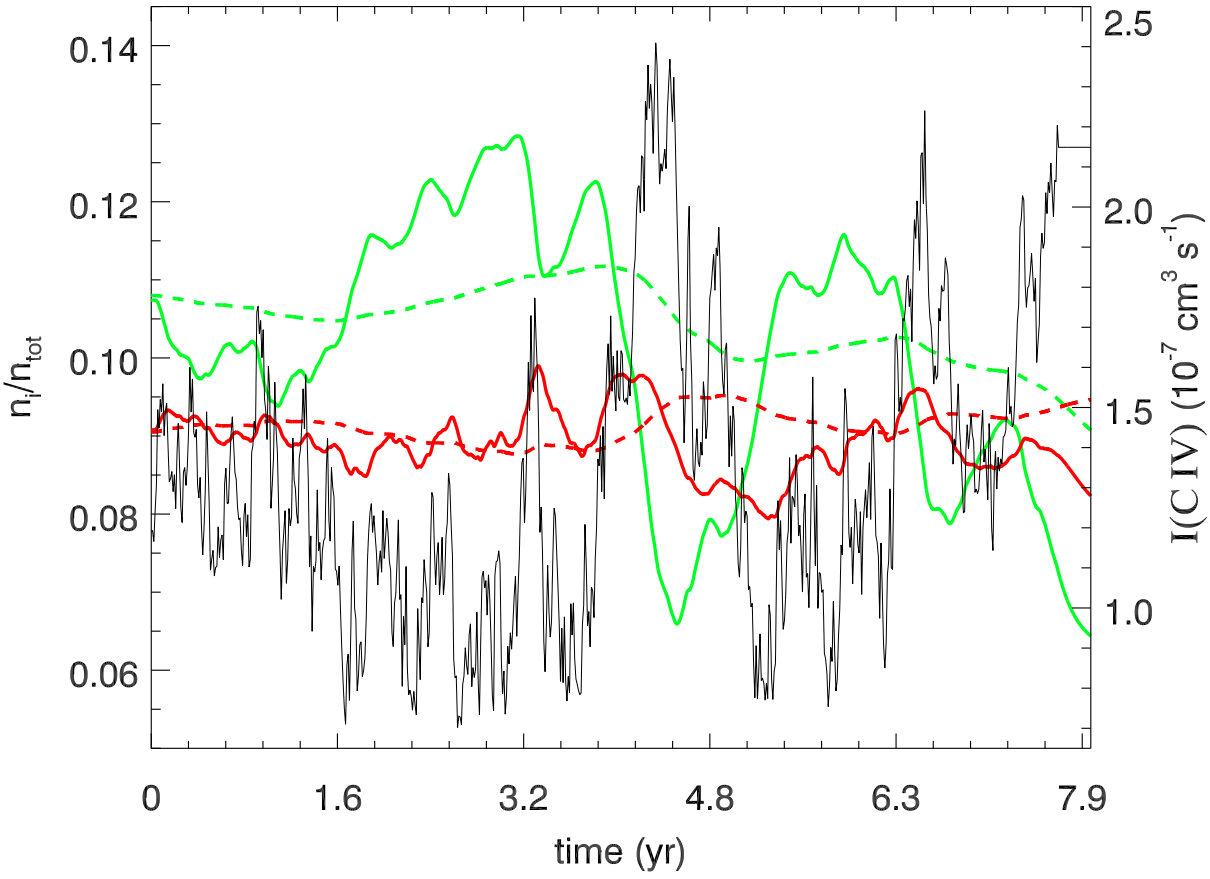

Figure 3.19 Simulations of CIV/C (green) and NV/N (red) versus time for one lightcurve in the sample. The solid lines are for a density $n_H = 10^{3.5}$ and the dashed lines are for $n_H = 10^{2.5}$. The black line is the ionization rate per particle for C IV and is propotional to the simulated lightcurve for this example.

is saturated in trough T1 and shows no significant change, but N V shows $> 3\sigma$ changes in residual intensity for both components of the doublet. In trough T2, change is observed for C IV, while no change is observed for N V. Since these two components have responded to continuum changes, we can put a lower limit on n_e and thereby, an upper limit on the distance. We do this by finding the highest density for which more than 99% of the lightcurves predict changes smaller than those suggested by the data. With distances $\lesssim 2.1$ kpc, these absorbers are within the confines of the host galaxy. We are also able to put an upper limit on n_e using the same method. We note that our simulations for trough T1 predict changes that are *smaller* than that measured for both high and low densities. This is because the ionization parameter is near the value producing the highest N V fractional abundance ($U_H = 10^{-1.5}$). As we increase n_e from 10 cm^{-3} to 10^4 cm^{-3}, the ionization state of the gas at the COS epoch increases. For $n_e \lesssim 100$ cm^{-3}, the change in n(N V) between STIS and COS epochs increases with increasing density. However, for $n_e \gtrsim 100$ cm^{-3}, the N V column density decreases as the ionization of the gas becomes higher than than that producing the highest fractional abundance of N V. At densities of $n_e \simeq 10^4$ cm^{-3}, the lower ionization state at the time of the STIS observation and the higher ionization state at the time of the COS observations produce approximately the same amount of N V, and it therefore appears as if there is no change between epochs. For even higher densities, simulations predict a decrease in n(N V) between the STIS and COS epochs.

We use the upper limits placed on the hydrogen number density n_H (recall that $n_H \simeq n_e/1.2$ in highly ionized plasma) to determine lower limits on the distance to the absorber from the ionizing source via the ionization parameter (Equation 3.22). These are given in Table 3.22, where R_{99} and R_{90} are the distances determined by requiring that 99% and 90% of the lightcurves, respectively, give results inconsistent with the differences in measured values. Except for component T1, these distances are determined using the n_e derived from C IV

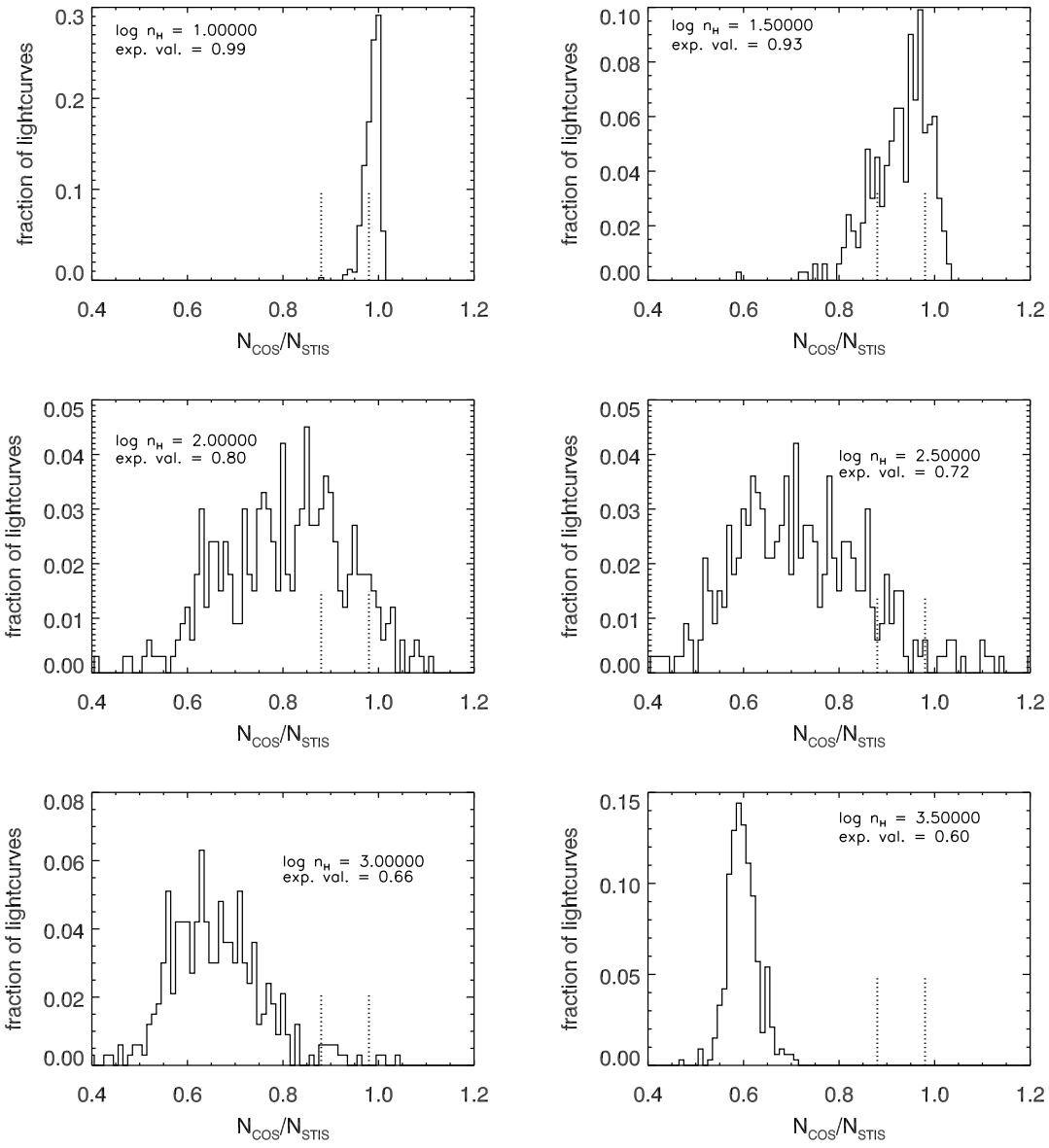

Figure 3.20 Determining the upper limit for n_H of the absorber. This example shows the results for trough T2, based on the C IV column density measurements. For each of the 935 simulated light curves (see section 5), we explicitly solve the time-dependent photoionization equations and calculate the expected ratio of C IV column density over a time period equal to the differences between the STIS and COS epochs. Each panel represents the fractional solution distribution of $N(\mathrm{C\,IV})_{COS}/N(\mathrm{C\,IV})_{STIS}$ for a given $\log(n_H)$ (cm^{-3}), which increases in the panels from left to right and top to bottom. The vertical dashed lines show the positive and negative 1σ errors on the measured value. We determine an n_H upper limit by increasing n_H until more than 99% of the calculated $N(\mathrm{C\,IV})_{COS}/N(\mathrm{C\,IV})_{STIS}$ are outside the error bars. In this example, we find $n_H < 10^{3.2}$ cm^{-3}.

Table 3.22 Density and Distance Limits from Simulations

Trough	v (km s^{-1})	log n_e(C IV) (cm^{-3})	log n_e(N V) (cm^{-3})	R_{99}[a] (pc)	R_{90}[b] (pc)
T1	-405	...[c]	1.1–4.2	60–2100	80–1500
T2	-310	1.1–3.2	<4.2	160–1830	370–1460
T3	-240	<3.2	<3.9	>130	>290
T4	-70	<3.1	<3.4	>130	>290
T5	-15	<3.6	...[d]	>130	>260
T6	+45	<2.8	<3.2	>150	>370
T7	+125	<2.5	...[e]	>130	>290

[a] Distances determined by requiring > 99% of the lightcurves to overpredict changes in column density.

[b] Distances determined by requiring > 90% of the lightcurves to overpredict changes in column density.

[c] Since C IV is saturated, we have no information about changes in N(C IV).

[d] For T5, the change predicted for the column density of N V is within the error regardless of number density precluding the determination of a useful limit.

[e] N V in trough T7 shows change in the red component but not the blue component yielding contradictory results.

since they give the smallest upper limit consistent with both the C IV and N V simulations. The rate of ionizing photons striking the gas is determined by fitting our SED to the 1175Å flux from STIS data given in Paper VI. We find $Q_H = 5.03 \times 10^{54}$ s^{-1}.

Chapter 4

Non-equilibrium Outflows

Photoionization analysis of AGN outflows often reveals a multi-phase structure, where multiple ionization components are required to fit the data. One interpretation is that these are physically disconnected outflows along our line of sight. However, it is difficult to explain the tight kinematic correspondence we observe if the outflows are not connected in some way. Another possiblility is that the outflow has an inhomogeneous structure. For example, a colder clumpy outflow embedded in a hotter wind. These outflows can be stable (Krolik et al., 1981), and are typically considered a more likely scenario. However, it is important to realize that the data are typically interpreted in models that assume ionization and thermal equilibria.

Is it possible that the inference of multiple ionization components is an artifact of our modeling under a false assumption of equilibrium? This question was partly addressed in Nicastro et al. (1999), but, to my knowledge, never fully developed. In this chapter, I discuss results of one of the first steps toward understanding the dynamical structure of outflows; namely, an investigation into the time-dependent photoionization structure of outflows subjected to

a variable flux. Three major findings have come out of simulations so far: 1) A plasma that appears to have multiple phases when ionization equilibrium is assumed may be a single-phase plasma that is out of equilibrium; 2) A non-equilibrium plasma is over/under ionized with respect to the radiation field. By tracking a time-dependent ionization parameter (a measure of the plasma response) and comparing it to changes in the radiation field, we can determine the density of the plasma; 3) Chemical abundances tend to be over/under predicted for non-equilibrium plasmas.

4.1 Example: A simulated data set with two distinct interpretations

Parts (a) and (b) of Figure 4.1 are different depictions of the same simulated data set. We used an electron number density of 10^3 cm^{-3} (a typical value found in outflows; e.g., Korista et al. 2008; Moe et al. 2009; Dunn et al. 2010b) and ionic column densities similar to those measured in AGN outflows (e.g., Mrk 509; Kriss et al. 2011; Arav et al. 2012). The simulated outflow has a single ionization phase with an ionization parameter $\log U(t = 0) = -1.5$ at time $t = 0$, and a total column density $\log N_H = 19.1$ cm^{-2} and is subjected to a drop in continuum flux.

In part (a) of Figure 4.1, ionization equilibrium is assumed. The curve for each ion represents points in the phase space where photoionization equilibrium models predict the observed column density. If all the lines were to cross at a single point, the result would be a single-phase model, characterized by the resulting (U) and (N_H), that is a good fit to the data. In Figure 1a, we see that there is no single-ionization model that accurately predicts the ionic column densities provided (see Table 4.1). If we allow for a two-phase medium with

each ionization phase characterized by one of the models marked with a square we obtain an acceptable solution.

In part (b) of Figure 4.1, we show how the ionic column densities evolve over time due the sudden drop in ionizing flux. We have plotted the ratio of the ionic column density predicted by the non-equilibrium model to the observed value for each ion as a function of time. A point where all the lines cross indicates a point in time when all the measured column densities are correctly predicted by the model. We see that for the given initial conditions and lightcurve, all the column densities are correctly predicted at time $t \approx 4.3 \times 10^7$ s (approximately 1 year after the drop in continuum flux).

In this simulated outflow, the assumption of ionization equilibrium results in a radically incorrect physical picture. The effect persists on timescales similar to long-term variability timescales of quasars (years to decades; de Vries et al. 2005). In Figure 2, we show the phase plots that occur at various times in the simulation presented in Figure 1b. Two ionization parameters are required in order to fit the data, and for a period of $\approx$ 3 years, they are separated by a factor of 10. Factor of 4 differences are seen over a 5 year period. For these simulations, we used a number density of 10^3 cm^{-3}. For lower density plasmas, the response time is even longer.

These two scenarios are easily distinguishable with monitoring. An important future project is to develop methods for distinguishing these scenarios when only a few spectral epochs are available in order to reduce the need for intensive spectral monitoring.

4.2 Effect on AGN feedback studies

A major goal in the study of quasar outflows is to measure their mass flow rate and kinetic power in order to assess their importance to AGN feedback processes. These quantities depend on the product of the distance and the total column density, RN_H, and **determination of these parameters is model dependent** (see Table 4.1). In the example above, the out-of-equilibrium model predicts a mass flow rate and kinetic power that are $\simeq 2$ times larger than the equilibrium models. In our example, the ionization parameters are separated by a factor of 10 in the equilibrium model, and the out-of-equilibrium model has an ionization parameter equal to that of the high-ionization component. In many cases the separation in ionization parameter is ~ 100: Discrepancies in the mass flow rate and kinetic luminosity between equilibrium and non-equilibrium models may be much larger than in our example.

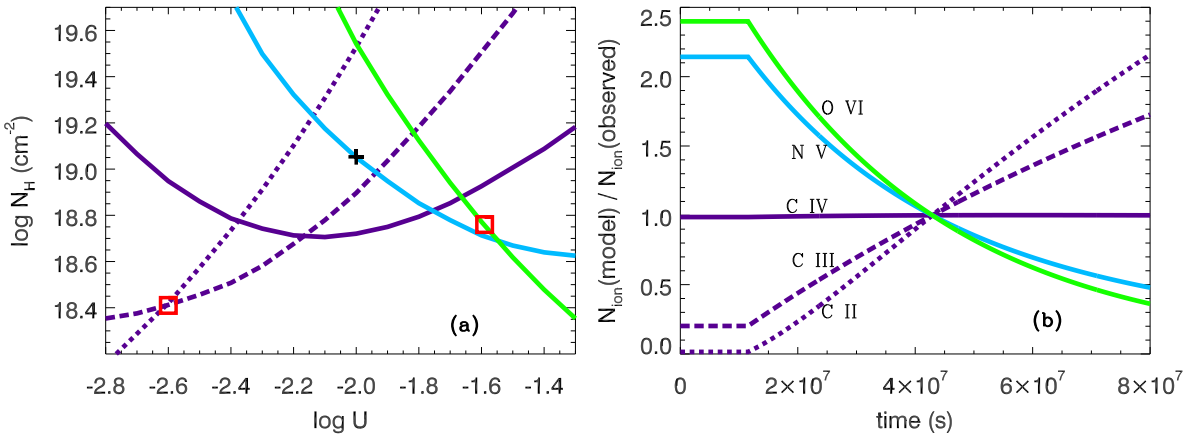

Figure 4.1 [(a)]**Photoionization equilibrium models.** Note that the single-phase model (A in Table 4.1; marked with a cross) is a poor fit to the simulated data. For the two-phase model (B in Table 4.1; marked with red squares), C IV comes from both ionization components. [(b)]**Time-dependent model** (C in Table4.1). This is a single-ionization-phase model with $\log U(t=0) = -1.5$ and $\log N_H = 19.1$ cm^{-2}. The flux drops to 5% of its original value for $t > 0$. The line for C IV is nearly flat since the maximum concentration of C IV occurs at $\log U \approx -2$. Once the plasma re-equilibrates (at $t \sim 10$ yr), the ionization parameter is $\log U = -2.8$ (see Figure 2).

Table 4.1 Photoionization Models for Figure 1

Model	$\log(U)$	$\log(N_H)$ (cm^{-2})	R (pc)	$\dot{M}$ ($M_\odot$ yr^{-1})	$\dot{E}_k$ (10^{40} erg s^{-1})	$(N_{\rm model} - N_{\rm observed})/\sigma$ C II	C III	C IV	N V	O VI
A	-2.0	19.1	55	0.04	1.1	4.1	-6.6	7.4	0.0	-6.6
B	-2.6,-1.6	18.4,18.7	109	0.05	1.3	0.0	0.0	0.0	1.2	0.0
C	-1.5	19.1	138	0.11	2.6	...	...	...	...	...

Notes. The initial photon rate ($Q(t=0)$)was chosen to be equal to that for NGC 3783 (Gabel05b), and the velocity is -1350 km/s (equal to component 1 in NGC 3783). σ is 10% of the simulated observed value for all ions. **Model A:** Single-phase outflow in photoionization equilibrium with $Q = 0.05\,Q(t=0)$; **Model B:** Two-phase outflow in photoionization equilibrium with $Q = 0.05\,Q(t=0)$; **Model C:** Single-phase outflow out of equilibrium. Model C fits the simulated observed values exactly since it was designed to do so. Predicted ionic column densities for models A and B are then compared to the same simulated observed values used for model C in order to determine if the outflow could be misinterpreted as being

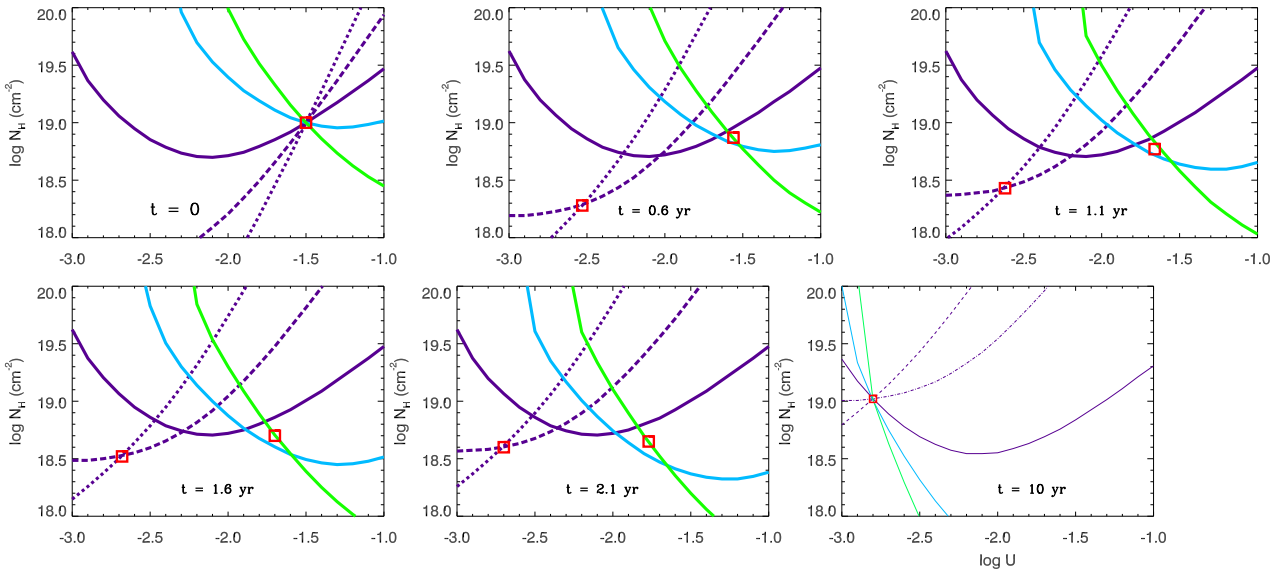

Figure 4.2 Phase plots for the outflow at various times. This is the same single-phase absorber model presented in Figure 1b (log $U(t = 0) = -1.5$, log $N_H = 19.1$ cm^{-2}). Colors and linestyles are the same as in Figure 1. The plots show the time-evolution of the outflow from top left to bottom right. The first plot shows the outflow in photoionization equilibrium just before the flux drops. Plots 2–5 show how the non-equilibrium single-phase outflow appears in phase-space diagrams, and the two-phase equilibrium solutions are marked with squares. The final plot shows the outflow in photoionization equilibrium after about 10 years. The effect persists on timescales similar to long-term variability timescales of quasars (years to decades; e.g., deVries05), with separation of a factor of 10 between ionization parameters for the two phases over a 2.7 year period. Factor of 4 differences are seen over a 5.1 year period. For these simulations, we used a number density of 10^3 cm^{-3}.

in photoionization equilibrium even though it was designed not to be. In this case, we find that assuming photoionization equilibrium underestimates the mass flow rate and kinetic luminosity by a factor of 2.

Chapter 5

Disc Winds

While the physical model of AGN outflows is a topic of ongoing research, a commonly adopted model is that of an accretion disk wind ((Murray et al., 1995; Murray & Chiang, 1995; Elvis, 2000; Proga et al., 2000)). Gas lifts off the accretion disk surrounding the supermassive black hole and is subjected to intense radiation from the X-ray and UV emission regions of the accretion disk. The typical launch radius for a black hole of a hundred-million solar masses is on the order of 10^16 cm (or ~ 0.001 pc). The gas closest to the emission source is overionized and cannot accelerate (Murray et al., 1995; Proga et al., 2000). However, this gas then forms a shield that protects the lithium-like ions (such as C IV, N V, and O VI) in the outer part of the outflow. The outer gas is then accelerated by radiation pressure (also known as line driving). The photoionization structure of these winds is poorly understood. Simulations that describe the dynamical structure by computing the density and wind velocity over time cannot provide self-consistent photoionization modeling due to computer-time limitations (Proga et al., 2000). Therefore, in the best simulations, only a rudimentary ionization solution is provided, and it is not clear whether these simulations actually produce the ions we typically see.

Historically, it was realized that the outflow must have a small filling factor and the "clouds" would require some sort of confinement. Accretion disk wind models proposed by Murray et al. (1995) bypassed the necessity for confined clouds at the cost of introducing a shielding gas. Theoretically, the shielding gas is supported by hydrodynamical modeling where it arises naturally in simulations (Proga et al., 2000). Observationally, there is little support for the existence of a shielding gas. X-ray studies finding very large column density gas that are highly ionized (so no C IV is observed) have cited this as evidence for a shield (e.g. Gallager 2002). But, to my knowledge, there has been no UV evidence.

In this Chapter, I describe our initial steps at determining the ionization structure of accretion disk winds. In particular, I discuss the ionization structure of the shielding gas that is required in order to accelerate the outflow to the high speeds typically observed. Future work will involve transmitting the SED through the shield in order to understand the ionization structure of the outflow itself.

5.1 Photoionization Simulations

Due to the prodigious amounts of radiation emitted from the accretion discs of super-massive black holes in AGN, radiation pressure is an obvious choice for accelerating large amounts of plasma to very high velocities (see Proga 2007 for a review of other acceleration mechanisms). However, ionization considerations lead to the well-known confinement problem (e.g., Weymann et al. 1985; Arav et al. 1994): In order to keep the absorber from being over-ionized as it accelerates, the clouds are required to have a small volume filling factor, necessitating a confining medium whose nature is unclear. The disc wind models of Murray et al. (1995, hereafter MCGV) bypass the necessity for confinement by introducing a shielding gas. The shield must have high He II bound-free opacity in order to protect lithium-like ions such as

C IV and N V. In hydrodynamic simulations of disc winds, the shielding gas arises naturally (Proga et al. 2000; hereafter PSK). A major effect of the shield is to allow lithium-like ions to survive in plasmas with ionization parameters $\gtrsim 10^5$ times larger than those typically inferred from UV spectra of quasar outflows.

Inclusion of self-consistent photoionization in full-scale hydrodynamic simulations is not feasible (PSK). Therefore, it becomes necessary to study the photoionization structure of outflows independently of the full dynamics. The ionization structure of shielded outflows was investigated by Chelouche & Netzer (2003). They found that, for heavy shielding, most metals in highly ionized outflows had a uniform ionization structure across a large range of ions (e.g., O III–O VIII have similar fractional abundances).

In this work, we investigate the ionization structure of the shielding gas in disc-wind models in order to predict signatures of the shield itself in UV absorption-line spectra. Of course, ionization structure is only part of the picture: We also consider the geometry of the shield/outflow system in relation to the UV and X-ray continuum regions and discuss possible configurations that could lead to non-detection of an existing shield.

5.1.1 UV Spectral Signatures of the Shielding Gas

In order to determine UV spectral signatures of the shielding gas, the following questions must be addressed: (1) Does the shield produce enough column density of lithium-like ions (such as C IV and N V)? (2) Is the shield along our line of sight? (3) Does the shield cover the UV emission region of the disc?

To address the first question, we determine the ionization structure of the shield. As we show in §5.1.1, a shielding gas that produces sufficient He II opacity to protect lithium-

like ions in the outflow enough for efficient line driving (i.e. $\tau(\mathrm{He\,II}) \gg 1$) will produce prodigious amounts of C IV. For the relevant range of ionization parameters, only models with $\tau(\mathrm{He\,II}) \ll 1$ produce too little C IV to be seen above noise levels in UV absorption line spectra. This implies that a shield that is along our line of sight fully covering the continuum source should be observed as absorption features in high-resolution UV spectra with BALs that are sufficiently detached from the peak of emission. In the following sub-sections, we discuss how the geometrical configuration of the shield/outflow affects the prediction of spectral signatures of shielding gas.

Photoionization modeling of the shield

We model the shielding gas as a homogenous, plane-parallel slab with a hydrogen density of 10^9 particles per cubic centimeter. The shield is irradiated with the UV-soft spectrum developed for quasars in Dunn et al. (2010b). The ionization equilbrium equations are solved self-consistently using version c08.00 of the spectral synthesis code *Cloudy* (last described by Ferland et al. 1998) for ionization parameters in the range $1 < U < 60$. This is the relevant range of ionization parameters for outflow models invoking the shielding gas: For a launch radius of 10^{16} cm and a bolometric luminosity of 10^{45} erg s^{-1}, number densities are $\sim 10^{11}$ cm^{-3} for the lowest ionization parameters and $\sim 10^9$ cm^{-3} for the highest (also see MCGV). In Figure 5.1, the optical depth of C IV is plotted as a function of ionization parameter for shield models having He II bound-free optical depths from 0.1 to 10^4. A major prediction of the shield models is strong absorption troughs in UV spectra due to the shield itself.

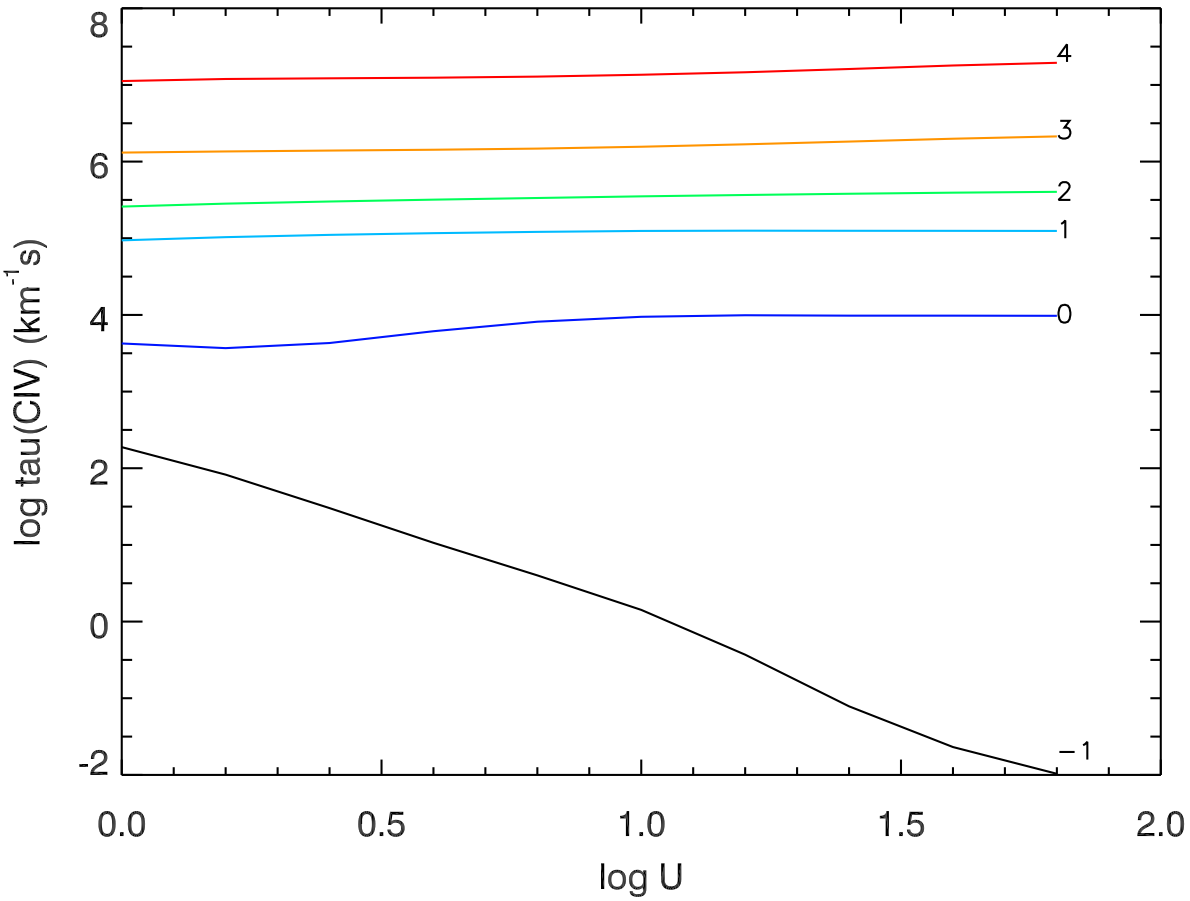

Figure 5.1 C IV optical depth as a function of U for various optical depths of He II(also given in log).

Geometrical Configurations

BALs are typically very deep. Absorption features from a shielding gas will be obscured by a BAL with on-set velocity ~ 0 km s^{-1}. Furthermore, in disc-wind models, the base of the outflow can have rotational velocities $\sim 0.1c$ (MCGV, Borguet & Hutsemékers 2010). The transverse Doppler effect blue-shifts C IV λ1550 Å by ~ 1500 km s^{-1} at these speeds. Therefore, it may be that absorption features from a shield will only be detectable when the BAL is sufficiently detached from its emission peak.

Is the shield along our line of sight?

Detached troughs in wind models are attributed to a line-of-sight effect in which we do not see the base of the wind. Obviously, a shield that is not along our line of sight to the continuum source will not appear as absorption features in spectra. Perhaps the shielding gas appears only near the base of the wind in order to facilitate acceleration, and our line of sight crosses through the wind to the UV continuum just over the shielding gas. Furthermore, the supermassive black holes powering quasars provide strong gravitational lenses for their accretion discs. The observed accretion disc has an apparent warping due the gravitational lensing (e.g., see Figure 4 of Armitage & Reynolds 2003; Jovanović 2012. Since the inclination angle for observation of BAL outflows in disc-wind models is high ($\sim 80°$), the disc is significantly lensed raising the possibility that the UV continuum source along our line of sight is from the far side of the disc. However, as discussed in MCGV, the ionization parameter of the outflow is too high to allow UV ions to form if the continuum is unshielded. Even if the gas is coasting, the ionization parameter is approximately constant since the number density goes like r^{-2}. Therefore, the shield must be along our line of sight if we are to see C IV in the outflow.

Does the shield cover the UV continuum source?

In order to efficiently drive an outflow by radiation pressure, the wind must be protected from soft X-rays but be exposed to UV continuum photons (MCGV, Chelouche & Netzer 2003). One way to do this is to spatially separate the shielding gas from the outflowing plasma such that the shield fully covers the X-ray continuum region but not the UV continuum region. While this is phenomenologically intriguing, it is not clear how such a situation would occur. In the model of MCGV, the boundary between shield and wind is indistinct. Similarly,

the shielding gas is naturally connected with the wind in simulations, typically launching at distances $\gtrsim 100 r_S$, where r_S is the Schwarzchild radius (e.g., PSK). For reference, UV emission at 1500Å for a typical quasar black hole peaks at $\sim 50 r_S$ (Peterson, 1997). At these launching radii, the contribution to the continuum from the accretion disc can be effectively treated as a point source. Furthermore, X-ray emission in quasars is not likely to be purely thermal. Several Seyfert galaxies show extended soft X-ray structures (e.g., Elvis et al. 1990; Wilson et al. 1992). Even if one could determine a mechanism for creating a shield physically separated by large distances from the outflow, the wind would likely be over-ionized by the extended X-ray emission.

5.1.2 Observations

Possible evidence of a shielding gas has been observed in X-ray data. In *Chandra* observations of a sample of six quasars, Gallagher et al. (2005) found that the objects whose C IV broad emission lines are most heavily blue-shifted show evidence of intrinsic X-ray absorption with no accompanying C IV absorption, indicating highly ionized gas that may be attributed to a shield in disc-wind models. However, as we have shown, any shielding gas with large enough He II opacity to radiatively drive an outflow to observed velocities will produce prodigious amounts of C IV. To our knowledge, no evidence of a shielding gas has been presented for UV data.

The shielding gas suffers some radiative driving before becoming over-ionized with typical velocities $\lesssim 100$ km s^{-1} (MCGV). As shown in Figure 5.1, For He II bound-free optical depths $\gtrsim 1$, the optical depth per unit velocity of C IV is $\gtrsim 10^4$. Therefore, the C IV absorption troughs will be fully saturated. In order that the outflow not be over-ionized, the continuum covering fraction of the shield must be at least as high as that of the outflow.

However, the broad emission lines are not covered by the shield. As mentioned above, the transverse Doppler effect can blue-shift the lines up to ~ 1500 km s^{-1}. We therefore expect to see narrow absorption features from the C IV doublet in the rest-frame wavelength range of 1540–1550 Å.

In Figure 5.2, we show VLT/X-shooter observations of four BAL quasars that should allow for direct observational evidence of a shielding gas. Only in SDSS J1100+0036 is there C IV absorption before the on-set of broad absorption. There are three narrow line systems with only one strong enough to be evidence of a shielding gas. The strongest absorption system appears to be fully saturated, but only if the absorber covers both the continuum source and the broad emission line region. Since the shield only covers the continuum, this system is not affiliated with a shielding gas.

5.2 Discussion

Disc-wind models invoking radiation pressure as the main acceleration mechanism require the existence of a shielding gas (MCGV; PSK), which has important consequences for outlfow ionization and quasar feedback studies. In particular, a shielded outflow will have ionization parameters much larger than those typically inferred. As a consequence, outflow distances derived from photoionization studies would be greatly overestimated.

In this work, we investigated the ionization structure of the shielding gas in disc wind models. Photoionization modeling predicts large optical depths of lithium-like ions for a shielding gas that allows for efficient line driving of quasar outflows. Observations of a sample of four BAL quasars in sufficiently high resolution UV data showed no evidence of a shielding gas. This poses a significant challenge to disc-wind models relying on a shielding gas to allow for

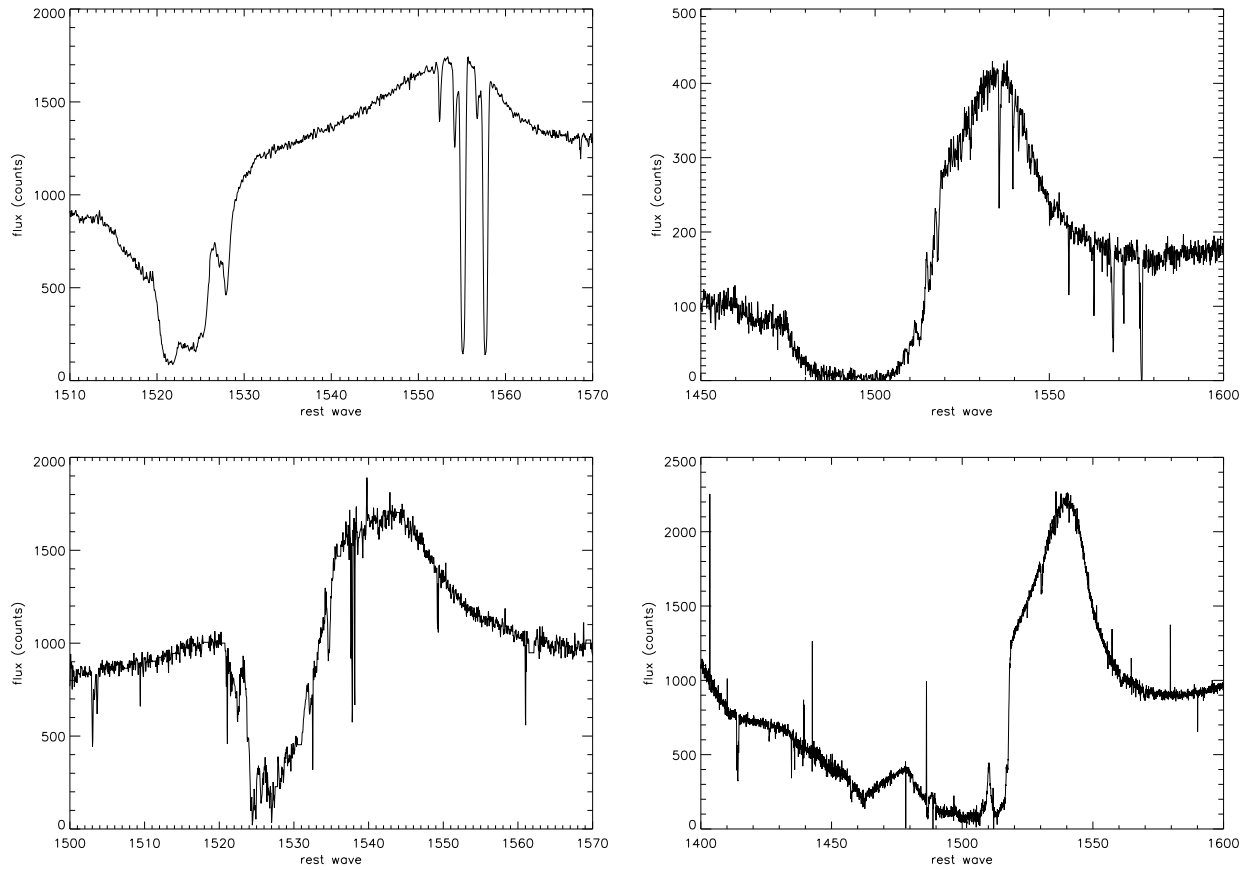

Figure 5.2 C IV region of four BAL quasars: top left: J1100+0036; top right: J1106+1939; bottom left: J1143+1934; bottom right: J1451+1441.

acceleration of quasar outflows by radiation pressure.

In absense of a shielding gas, radiation line driving can be a dominant acceleration mechanism only if the outflow is confined by some external medium, with magnetic fields being a leading candidate (e.g., Arav et al. 1994). Hamann et al. (2012) have discovered NAL and mini-BAL data that do not show evidence of X-ray shielding even in outflows with very high velocities, implying that a shielding gas is not a necessary component of the outflow phenomenon. With NAL velocities $\gtrsim 10^4$ km s^{-1} in some cases, the acceleration mechanism must be non-thermal. However, models invoking confinement of the outflow to a small filling factor in order to avoid over-ionization of the plasma do not naturally explain the observation that

BAL quasars have lower X-ray-to-optical flux ratios than do non-BAL quasars (e.g., Stalin et al. 2011).

Due to the importance of determining the existence of a shielding gas to ionization and quasar feedback studies, it would be worthwhile to expand the sample. One difficulty in creating an unbiased sample is that, in the context of a disc-wind model, the disc is viewed at angles near the opening angle of the wind (e.g., MCGV1995). This specialized line of sight is difficult to avoid. However, we have shown that any line of sight along which we see absorption due to lithium-like ions in the outflow must include the shielding gas. The main difficulty has been in finding sufficiently high resolution data with BAL on-set velocities $\gtrsim 2000$ km s^{-1}.

Chapter 6

Conclusion

My work for this thesis mainly involved determining distances and energetics of AGN outflows using photoionization modeling and density diagnostics. Densities were determined in one of two ways; 1) comparing ionic column densities of metastable and ground states of a given ion and 2) analysis of the time-variability of spectral absorption features. This work is relevant for understanding how the outflows are formed and accelerated and how they interact with their environment. We also address the question of whether AGN can provide the necessary feedback for galaxy evolution. For example, galaxies produced in simulations are much larger than those we observe today. In one scenario, energy from the supermassive black hole at the center of the galaxy couples to the interstellar medium and evacuates gas necessary for star formation, thus curbing the growth of the host galaxy. This same mechanism curbs the growth of the black hole itself since it is expelling the gas that would otherwise eventually fall into the black hole. In the following sections, I discuss results from our observations, some implications of these results, and theoretical work inspired by our observations.

Table 6.1 Densities and Distances for Outflows in this Thesis

Object	n_H cm^{-3}	R (kpc)
IRAS F04250-5718	< 30	> 3
IRAS F22456-5125	1.5	11.9[a]
QSO 1044+3656	10^4	1.7
AKARI J1757+5907	$< 10^{3.8}$	> 3.7
HE0238-1904	$10^{3.8}$	1.5[b]
Mrk 509	$< 10^{3.1}$	> 0.2[c]

[a] Average value of both troughs.
[b] From trough A.
[c] For most troughs.

The distance and energetics of AGN outflows are poorly known. Observations of objects with density diagnostics in the form of troughs from ions with excited states or significant flux variation are required in order to improve our understanding. We have therefore targeted objects that allow for robust density determinations. Table 6.1 shows the distances and densities for objects discussed in this thesis. A major result of our work that outflows are often at distances of hundreds to thousands of parsecs from the central source, much farther than typically assumed. The large disances we find are not easily explained by current theoretical models. For example, a well-accepted model is that the outflow originates from the accretion disk around the supermassive black hole (see Chapter 5). However, with a launch radius $\sim 10^{16}$ cm and an acceleration region extending to $\sim 10^{17}$ cm, it becomes very difficult to explain outflows that are at distances of $\gtrsim 10^{21}$ cm. In the adaptation of the disk-wind model by Elvis (2000), NAL outflows are oserved very near the launch radius. Our observations are in stark disagreement: Outflows at large distances cannot be connected with the accretion disk.

When we have density diagnostics, we often find the density of the outflow is less than the canonical 10^4 cm^{-2}. As shown in Arav et al. (2012), outflows with densities lower than

$\sim 10^3$ cm^{-2} have recombination timescales that are larger than the variability timescales typical of AGN. In these cases, the outflow is not in ionization equilibrium as is commonly assumed. This has implications for photoionization analysis of outflows as well as distance determinations. As discussed in Chapter 4, work to understand the time-dependent photoionization structure of AGN outflows is in its infancy. If low density outflows are common, much more work needs to be done in this area.

What connects our work on AGN outflows to the larger astronomical community is the possible effect they have on their environment, including the curbing of galaxy growth and metal enrichment of the intergalactic medium. Density determinations and photoionization modeling allow us to determine the kinetic luminosity of AGN outflows. Currently, simulations show kinetic luminosities $\sim$ 0.5–5% of the bolometric luminosity of the AGN are sufficient to provide the feedback necessary to solve many problems in evolutionary scenarios. We have found outflows in two objects that are powerful enough to provide feedback. Future work is required to determine whether these are isolated cases or representative of quasars in general.

In order to further investigate the implications of our observational results, I have investigated the photoionization structure in toy models. As discussed in Chapter 4, non-equilibrium effects can have unexpected results. In particular, I find in simulations: 1) If ionization equilibrium is assumed, the outflow appears to have multiple ionization phases; 2) Chemical abundances can be over/under estimated if the outflow is over/under ionized with respect to equilibrium. In Chapter 5, I discussed photoionization modeling of shielded outflows. Simulations show that a shielding gas that sufficiently protects lithium-like ions in the outflow will, itself, produce prodigious amounts of lithium-like ions. Therefore, observations with sufficiently high resolution should show absorption features from the shielding gas. The troughs will likely be blue-shifted to the transverse doppler effect for high rotation speeds.

Therefore, observations of quasar outflows with detached troughs are good candidates for observing the shielding gas. In a preliminary look at four objects, we find no evidence for a shielding gas. In a recent paper by Hamann et al. (2013), photoinization modeling of mini-BAL outflows show that high speeds can be obtained without a shielding gas. Our results along with simulations are indicating that the commonly adopted model of an accretion disc wind fails in many cases.

Bibliography

Aoki, K., Oyabu, S., Dunn, J. P., Arav, N., Edmonds, D., Korista, K. T., Matsuhara, H., & Toba, Y. 2011, ArXiv e-prints

Arav, N. 2010, in IAU Symposium, Vol. 267, IAU Symposium, ed. B. M. Peterson, R. S. Somerville, & T. Storchi-Bergmann, 350–353

Arav, N., Becker, R. H., Laurent-Muehleisen, S. A., Gregg, M. D., White, R. L., Brotherton, M. S., & de Kool, M. 1999, ApJ, 524, 566

Arav, N., Borguet, B., Chamberlain, C., Edmonds, D., & Danforth, C. 2013, ArXiv e-prints

Arav, N., Dunn, J. P., Korista, K. T., Edmonds, D., Gonzalez Serrano, J. I., Benn, C., & Jimenez-Lujan, F. 2011, ApJ

Arav, N., Kaastra, J., Kriss, G. A., Korista, K. T., Gabel, J., & Proga, D. 2005, ApJ, 620, 665

Arav, N., Korista, K. T., & de Kool, M. 2002, ApJ, 566, 699

Arav, N., Li, Z.-Y., & Begelman, M. C. 1994, ApJ, 432, 62

Arav, N., Moe, M., Costantini, E., Korista, K. T., Benn, C., & Ellison, S. 2008, ApJ, 681, 954

Arav, N., et al. 2001, ApJ, 561, 118

—. 2007, ApJ, 658, 829

—. 2012, A&A, 544, A33

Armitage, P. J., & Reynolds, C. S. 2003, MNRAS, 341, 1041

Ballero, S. K., Matteucci, F., Ciotti, L., Calura, F., & Padovani, P. 2008, A&A, 478, 335

Barlow, T. A., Hamann, F., & Sargent, W. L. W. 1997, in Astronomical Society of the Pacific Conference Series, Vol. 128, Mass Ejection from Active Galactic Nuclei, ed. N. Arav, I. Shlosman, & R. J. Weymann, 13–+

Barlow, T. A., & Sargent, W. L. W. 1997, AJ, 113, 136

Bennert, V. N., Treu, T., Woo, J.-H., Malkan, M. A., Le Bris, A., Auger, M. W., Gallagher, S., & Blandford, R. D. 2010, ApJ, 708, 1507

Bentz, M. C., Peterson, B. M., Pogge, R. W., Vestergaard, M., & Onken, C. A. 2006, ApJ, 644, 133

Borguet, B., & Hutsemékers, D. 2010, A&A, 515, A22

Borguet, B. C. J., Arav, N., Edmonds, D., Chamberlain, C., & Benn, C. 2013, ApJ, 762, 49

Borguet, B. C. J., Edmonds, D., Arav, N., Dunn, J., & Kriss, G. A. 2012, ApJ, 751, 107

Bottorff, M. C., Korista, K. T., & Shlosman, I. 2000, ApJ, 537, 134

Brissenden, R. J. V., Tuohy, I. R., Remillard, R. A., Buckley, D. A. H., Bicknell, G. V., Bradt, H. V., & Schwartz, D. A. 1987, Proceedings of the Astronomical Society of Australia, 7, 212

Brotherton, M. S., Tran, H. D., Becker, R. H., Gregg, M. D., Laurent-Muehleisen, S. A., & White, R. L. 2001, ApJ, 546, 775

Chelouche, D., & Netzer, H. 2003, MNRAS, 344, 233

Ciotti, L., Ostriker, J. P., & Proga, D. 2010, ApJ, 717, 708

Colbert, E. J. M., Baum, S. A., Gallimore, J. F., O'Dea, C. P., Lehnert, M. D., Tsvetanov, Z. I., Mulchaey, J. S., & Caganoff, S. 1996, ApJS, 105, 75

Collier, S., & Peterson, B. M. 2001, ApJ, 555, 775

Crenshaw, D. M., & Kraemer, S. B. 2007, ApJ, 659, 250

Crenshaw, D. M., Kraemer, S. B., Boggess, A., Maran, S. P., Mushotzky, R. F., & Wu, C. 1999, ApJ, 516, 750

Crenshaw, D. M., Kraemer, S. B., & George, I. M. 2003, ARAA, 41, 117

Dahlem, M., Weaver, K. A., & Heckman, T. M. 1998, ApJS, 118, 401

Dai, X., Shankar, F., & Sivakoff, G. R. 2008, ApJ, 672, 108

de Kool, M., Arav, N., Becker, R. H., Gregg, M. D., White, R. L., Laurent-Muehleisen, S. A., Price, T., & Korista, K. T. 2001, ApJ, 548, 609

de Kool, M., Korista, K. T., & Arav, N. 2002, ApJ, 580, 54

de Vries, W. H., Becker, R. H., White, R. L., & Loomis, C. 2005, AJ, 129, 615

Detmers, R. G., et al. 2011, A&A, 534, A38

Di Matteo, T., Springel, V., & Hernquist, L. 2005, Nature, 433, 604

Dunn, J. P., Crenshaw, D. M., Kraemer, S. B., & Gabel, J. R. 2007, AJ, 134, 1061

Dunn, J. P., Crenshaw, D. M., Kraemer, S. B., & Trippe, M. L. 2010a, ApJ, 713, 900

Dunn, J. P., Jackson, B., Deo, R. P., Farrington, C., Das, V., & Crenshaw, D. M. 2006, PASP, 118, 572

Dunn, J. P., et al. 2010b, ApJ, 709, 611

Edmonds, D., et al. 2011, ApJ, 739, 7

Elvis, M. 2000, ApJ, 545, 63

Elvis, M., Fassnacht, C., Wilson, A. S., & Briel, U. 1990, ApJ, 361, 459

Elvis, M., Plummer, D., Schachter, J., & Fabbiano, G. 1992, ApJS, 80, 257

Ferland, G. J., Korista, K. T., Verner, D. A., Ferguson, J. W., Kingdon, J. B., & Verner, E. M. 1998, PASP, 110, 761

Ferrarese, L., & Merritt, D. 2000, ApJL, 539, L9

Gabel, J. R., Arav, N., & Kim, T. 2006, ApJ, 646, 742

Gabel, J. R., et al. 2003, ApJ, 583, 178

—. 2005a, ApJ, 631, 741

—. 2005b, ApJ, 623, 85

Gallagher, S. C., Richards, G. T., Hall, P. B., Brandt, W. N., Schneider, D. P., & Vanden Berk, D. E. 2005, AJ, 129, 567

Ganguly, R., Bond, N. A., Charlton, J. C., Eracleous, M., Brandt, W. N., & Churchill, C. W. 2001, ApJ, 549, 133

Ganguly, R., Eracleous, M., Charlton, J. C., & Churchill, C. W. 1999, AJ, 117, 2594

Gebhardt, K., et al. 2000, ApJL, 539, L13

González Delgado, R. M., & Pérez, E. 2000, MNRAS, 317, 64

Guainazzi, M., et al. 1998, A&A, 339, 327

Halpern, J. P., Leighly, K. M., Marshall, H. L., Eracleous, M., & Storchi-Bergmann, T. 1998, PASP, 110, 1394

Hamann, F. 1997, ApJS, 109, 279

Hamann, F., Barlow, T. A., Junkkarinen, V., & Burbidge, E. M. 1997, ApJ, 478, 80

Hamann, F., Chartas, G., McGraw, S., Rodriguez Hidalgo, P., Shields, J., Capellupo, D., Charlton, J., & Eracleous, M. 2013, ArXiv e-prints

Hamann, F., & Ferland, G. 1999, ARAA, 37, 487

Hamann, F., Kanekar, N., Prochaska, J. X., Murphy, M. T., Ellison, S., Malec, A. L., Milutinovic, N., & Ubachs, W. 2011, MNRAS, 410, 1957

Hamann, F., Korista, K. T., Ferland, G. J., Warner, C., & Baldwin, J. 2002, ApJ, 564, 592

Hamann, F., Simon, L., Hidalgo, P. R., & Capellupo, D. 2012, in Astronomical Society of the Pacific Conference Series, Vol. 460, AGN Winds in Charleston, ed. G. Chartas, F. Hamann, & K. M. Leighly, 47

Hamann, F. W., Barlow, T. A., Chaffee, F. C., Foltz, C. B., & Weymann, R. J. 2001, ApJ, 550, 142

Hamann, F. W., Netzer, H., & Shields, J. C. 2000, ApJ, 536, 101

Heckman, T. M., Lehnert, M. D., Strickland, D. K., & Armus, L. 2000, ApJS, 129, 493

Heinz, S., Brüggen, M., Young, A., & Levesque, E. 2006, MNRAS, 373, L65

Hewett, P. C., & Foltz, C. B. 2003, AJ, 125, 1784

Hopkins, P. F., & Elvis, M. 2010, MNRAS, 401, 7

Horne, K., Peterson, B. M., Collier, S. J., & Netzer, H. 2004, PASP, 116, 465

Ishihara, D., et al. 2010, A&A, 514, A1

Jovanović, P. 2012, NAR, 56, 37

Kawaguchi, T. 2003, ApJ, 593, 69

Khachikyan, É. Y., & Weedman, D. W. 1971, Astrophysics, 7, 231

Korista, K. T., Bautista, M. A., Arav, N., Moe, M., Costantini, E., & Benn, C. 2008, ApJ, 688, 108

Kraemer, S. B., Crenshaw, D. M., Yaqoob, T., McKernan, B., Gabel, J. R., George, I. M., Turner, T. J., & Dunn, J. P. 2003, ApJ, 582, 125

Kraemer, S. B., et al. 2001, ApJ, 551, 671

Kriss, G. A., et al. 2011, A&A, 534, A41+

Krolik, J. H., & Kriss, G. A. 1995, ApJ, 447, 512

Krolik, J. H., McKee, C. F., & Tarter, C. B. 1981, ApJ, 249, 422

Laor, A., Fiore, F., Elvis, M., Wilkes, B. J., & McDowell, J. C. 1997, ApJ, 477, 93

Lehnert, M. D., & Heckman, T. M. 1996, ApJ, 462, 651

Lodders, K., & Palme, H. 2009, Meteoritics and Planetary Science Supplement, 72, 5154

Marshall, H. L., Fruscione, A., & Carone, T. E. 1995, ApJ, 439, 90

Martin, C. L. 2005, ApJ, 621, 227

Martin, C. L., & Bouché, N. 2009, ApJ, 703, 1394

Mathews, W. G., & Ferland, G. J. 1987, ApJ, 323, 456

McCarthy, I. G., et al. 2010, MNRAS, 406, 822

Mehdipour, M., et al. 2011, A&A, 534, A39+

Misawa, T., Charlton, J. C., Eracleous, M., Ganguly, R., Tytler, D., Kirkman, D., Suzuki, N., & Lubin, D. 2007, ApJS, 171, 1

Misawa, T., Eracleous, M., Chartas, G., & Charlton, J. C. 2008, ApJ, 677, 863

Moe, M., Arav, N., Bautista, M. A., & Korista, K. T. 2009, ApJ, 706, 525

Murakami, H., et al. 2007, PASJ, 59, 369

Murray, N., & Chiang, J. 1995, ApJL, 454, L105

Murray, N., Chiang, J., Grossman, S. A., & Voit, G. M. 1995, ApJ, 451, 498

Muzahid, S., Srianand, R., Savage, B. D., Narayanan, A., Mohan, V., & Dewangan, G. C. 2012, MNRAS, 424, L59

Netzer, H. 2008, NAR, 52, 257

Nicastro, F., Fiore, F., Perola, G. C., & Elvis, M. 1999, ApJ, 512, 184

Olive, K. A., & Scully, S. T. 1996, International Journal of Modern Physics A, 11, 409

Omma, H., & Binney, J. 2004, MNRAS, 350, L13

Onken, C. A., Ferrarese, L., Merritt, D., Peterson, B. M., Pogge, R. W., Vestergaard, M., & Wandel, A. 2004, ApJ, 615, 645

Osterbrock, D. E., & Ferland, G. J. 2006, Astrophysics of gaseous nebulae and active galactic nuclei

Osterman, S., et al. 2010, arXiv:1012.5827 [astro-ph.IM]

Ostriker, J. P., Choi, E., Ciotti, L., Novak, G. S., & Proga, D. 2010, ApJ, 722, 642

Peterson, B. M. 1997, An Introduction to Active Galactic Nuclei

Peterson, B. M., Wanders, I., Horne, K., Collier, S., Alexander, T., Kaspi, S., & Maoz, D. 1998, PASP, 110, 660

Pounds, K. A., Reeves, J. N., Page, K. L., & O'Brien, P. T. 2004a, ApJ, 605, 670

—. 2004b, ApJ, 616, 696

Proga, D. 2007, ApJ, 661, 693

Proga, D., Stone, J. M., & Kallman, T. R. 2000, ApJ, 543, 686

Reichard, T. A., et al. 2003, AJ, 125, 1711

Rodriguez-Pascual, P. M., et al. 1997, ApJS, 110, 9

Rupke, D. S., Veilleux, S., & Sanders, D. B. 2005, ApJ, 632, 751

Salpeter, E. E. 1964, ApJ, 140, 796

Savage, B. D., & Sembach, K. R. 1991, ApJ, 379, 245

Scannapieco, E., & Oh, S. P. 2004, ApJ, 608, 62

Schlegel, D. J., Finkbeiner, D. P., & Davis, M. 1998, ApJ, 500, 525

Skrutskie, M. F., et al. 2006, AJ, 131, 1163

Soker, N. 2010, MNRAS, 401, 2793

Soker, N., & Meiron, Y. 2011, MNRAS, 411, 1803

Stalin, C. S., Srianand, R., & Petitjean, P. 2011, MNRAS, 413, 1013

Steenbrugge, K. C., Fenovčík, M., Kaastra, J. S., Costantini, E., & Verbunt, F. 2009, A&A, 496, 107

Steenbrugge, K. C., et al. 2011, A&A, 534, A42+

Tennyson, J. 2005, Astronomical spectroscopy : an introduction to the atomic and molecular physics of astronomical spectra

Thomas, H., Beuermann, K., Reinsch, K., Schwope, A. D., Truemper, J., & Voges, W. 1998, A&A, 335, 467

Tueller, J., Mushotzky, R. F., Barthelmy, S., Cannizzo, J. K., Gehrels, N., Markwardt, C. B., Skinner, G. K., & Winter, L. M. 2008, ApJ, 681, 113

Turner, T. J., Miller, L., Kraemer, S. B., Reeves, J. N., & Pounds, K. A. 2009, ApJ, 698, 99

Turner, T. J., et al. 1999, ApJ, 510, 178

Urrutia, T., Becker, R. H., White, R. L., Glikman, E., Lacy, M., Hodge, J., & Gregg, M. D. 2009, ApJ, 698, 1095

Urry, C. M., & Padovani, P. 1995, PASP, 107, 803

Veilleux, S., Cecil, G., & Bland-Hawthorn, J. 2005, ARAA, 43, 769

Vernaleo, J. C., & Reynolds, C. S. 2006, ApJ, 645, 83

—. 2007, ApJ, 671, 171

Véron-Cetty, M., & Véron, P. 2006, A&A, 455, 773

Wakker, B. P., & Savage, B. D. 2009, ApJS, 182, 378

Weymann, R. J., Morris, S. L., Foltz, C. B., & Hewett, P. C. 1991, ApJ, 373, 23

Weymann, R. J., Turnshek, D. A., & Christiansen, W. A. 1985, in Astrophysics of Active Galaxies and Quasi-Stellar Objects, ed. J. S. Miller, 333–365

Weymann, R. J., Williams, R. E., Peterson, B. M., & Turnshek, D. A. 1979, ApJ, 234, 33

White, R. J., & Peterson, B. M. 1994, PASP, 106, 879

Wilson, A. S., Elvis, M., Lawrence, A., & Bland-Hawthorn, J. 1992, ApJL, 391, L75

Wood, K. S., et al. 1984, ApJS, 56, 507

AGN feedback references cited in the fourth paragraph of Chapter 1.

a - AGN feedback influence on cluster cooling flow: 1. Baum, S. A. & O'Dea, C. P. 1991,MNRAS, 250, 737; 2. Begelman, M. C. & Cioffi, D. F. 1989, ApJ, 345, L21; 3. Best, P. N. et al. 2005, MNRAS, 362, 25; 4. Best, P. N. et al. 2007, MNRAS, 379, 894; 5. Birzani, L. et al. 2004, ApJ, 607, 800; 6. Borgani S. et al. 2002, MNRAS, 336,409; 7. Bower, R. G. et al. 2001, MNRAS, 325, 497; 8. Brüggen, M. & Kaiser, C. R. 2002, Nature, 6895, 301; 9. Brüggen, M. & Scannapieco, E. 2009, MNRAS, 398, 548; 10. Cattaneo, A. & Teyssier, R. 2007, MNRAS, 376, 1547; 11. Churazov, E. et al. 2001, MNRAS, 332, 729; 12. Churazov, E. et al. 2002, MNRAS, 332,729; 13. Ciotti, L. & Ostriker, J. P. 2001, ApJ, 551, 131; 14. Ciotti, L. & Ostriker, J. P. 2007, ApJ, 665, 1038; 15. Ciotti, L. et al. 2009, ApJ, 699, 89; 16. McCarthy, I. G. et al. 2010, MNRAS, 406, 822; 17. Gaspari, M. et al. 2011, MNRAS, 415, 1549; 18. Omma, H. & Binney, J. 2004, MNRAS, 350, L13; 19. Omma, H. et al. 2004, MNRAS, 348, 1105; 20. Ma, C.-J. et al. 2011, ApJ, 740, 51; 21. Platania, P. et al. 2002, MNRAS, 337, 242; 22. Pope, E.C.D. et al. 2012, MNRAS, 419, 50; 23. Puchwein, E. et al. 2010, MNRAS, 406, 936; 24. Tabor, G. & Binney, J. 1993, MNRAS, 263,323; 25. Vernaleo, J. C. & Reynolds, C. S. 2006, ApJ, 645, 83; 26. Wu, K. K. S. et al. 2000, MNRAS, 318, 889;
b - AGN feedback influence on the growth and evolution of the SMBH: 27. Begelman, M. & Ruszkowski, M. 2005, RSPTA, 363, 655; 28. Blandford, R, D. & Begelman, M. C. 2004, MNRAS, 349, 68; 29. Blecha, L. et al. 2011, MNRAS, 412, 2154; 30. Booth, C. M. & Schaye, J. 2009, MNRAS, 398, 53; 31. Cattaneo, A. et al. 2005, MNRAS, 364, 407; 32. Croton, D. J. et al.

2006, MNRAS, 365,11; 33. De Buhr, J. et al. 2011, MNRAS, 412, 1341; 34. Di Matteo, I. et al. 2003, ApJ, 593, 56; 35. Di Matteo, I. et al. 2008, ApJ 678, 33; 36. Fabian, A. et al. 2006, MNRAS, 373, 16; 37. Gitti, M. et al. 2011, ApJ 732, 13; 38. Hopkins, P. F. et al. 2006, ApJ, 652, 864; 39. Hopkins, P. F. et al. 2007, ApJ, 669, 45; 40. Hopkins, P. F. et al. 2009, MNRAS, 398, 303; 41. Kauffmann, G. & Haenelt, M. 2000, MNRAS, 311, 576; 42. King, A. et al. 2003, ApJ, 596, L27; 43. King, A. et al. 2005, ApJ, 635, L121; 44. Lamastra, A. et al. 2010, MNRAS, 405, 29; 45. Lusso, E. & Ciotti, L. 2011, A&A, 525, 115; 46. Loeb, A. 2004, MNRAS, 350, 725; 47. Malbon, R. K. 2007, MNRAS, 382, 1394; 48. Monaco, P. et al. 2000, MNRAS, 311, 279; 49. Silk, J. & Rees, M. J. 1998, A&A 331, 1; 50. Younger, J. D. et al. 2008, ApJ, 686, 815; 51. Volonteri, M. et al. 2003, ApJ, 582, 559; 52. Volonteri, M. et al. 2008, MNRAS, 383, 1079; 53. Volonteri, M. & Stark, D.P. 2011, MNRAS, 417, 2085; 54. Wyithe, I. S. B. & Loeb, A. 2003, ApJ, 595,614;
c - AGN feedback influence on the evolution of the host galaxy: 55. Begelman, M. C. & Nath, B. B. 2005, MNRAS, 361, 1387; 56. Bower, R. G. et al. 2006, MNRAS, 370, 645; 57. Bower, R. G. et al. 2010, MNRAS, 407, 201; 58. Cattaneo, A. et al. 2006, MNRAS, 370, 1651; 59. Cattaneo, A. et al. 2007, MNRAS, 377, 63; 60. Ciotti, L. et al. 2010, ApJ, 717, 718; 61. De Lucia, G. et al. 2006, MNRAS, 266, 499; 62. Di Matteo, T. et al. 2005, Nature, 433, 604; 63. Granato, G. L. et al. 2004, ApJ, 600, 580; 64. Haiman et al. 2006, ApJ, 650, 7; 65. Hambrick, D. et al. 2011, ApJ, 738, 16; 66. Hatton, S. et al. 2003, MNRAS, 343, 75; 67. Hopkins, P. F., et al. 2005, ApJ, 630, 705; 68. Hopkins, P. F., et al. 2008, ApJS, 175, 356; 69. Kaviraj, S. et al. 2005, MNRAS, 360, 60; 70. Kaviraj, S. et al. 2011, MNRAS, 415, 3798; 71. Khochfar, S. & Silk, J. 2006, MNRAS, 370, 902; 72. Menci, N., et al. 2006, ApJ, 647, 753; 73. Monaco, P. & Fantanot, F. 2005, MNRAS, 359, 283; 74. Ostriker, J. et al. 2010, ApJ, 722, 642; 75. Rettura, A. et al. 2010, ApJ, 709, 512; 76. Scannapieco, E. & Ho, P. S. 2004, ApJ, 608, 62; 77. Shabala, S. et al. 2011, MNRAS, 413, 2815; 78. Schawinski, K. et al. 2006, Nature, 442, 888; 79. Somerville, R. S., et al. 2008, MNRAS.tmp.1241S; 80. Springel, V., et al. 2005, MNRAS, 361, 776; 81. van de Voort, F. et al. 2011, MNRAS, 415, 2782;
d - AGN feedback influence on the IGM: enrichement, entropy, and magnetization: 82. Barai, P. et al. 2004, Bull. Astron. Soc. India, 32, 385; 83. Bhattacharya, S. et al. 2008, MNRAS, 389, 34; 84. Brüggen, M. et al. 2009, RevMexAA, 36, 216; 85. Calura, F. & Menci, N. 2009, MNRAS, 400, 1347; 86. Cavaliere, A., Lapi, A. & Menci, N. 2002, ApJ, 581, 1; 87. Colgate, S. A. & Li, H. 1999, Ap&SS, 264, 357; 88. De Lucia, G. et al. 2004, MNRAS, 349, 1101; 89. Dubois, Y. et al. 2011, MNRAS, 417, 1853; 90. Fabjan, D. et al. 2010, MNRAS, 401, 1670; 91. Furlanetto, S. R. & Loeb, A. 2001, ApJ 556, 619; 92. Germain, J. et al. 2009, ApJ, 704, 1002; 93. Gopal Krishna et al. 2004, Korean. Astron. Soc., 37, 517; 94. Jetha, N. N. et al. 2007, MNRAS, 376, 193; 95. Khalatyan, A. et al. 2008, MNRAS, 387, 13; 96. Kronberg, P. P., et al. 2001, ApJ 560, 178; 97. Levine, R. & Gnedin, N. Y. 2005, ApJ, 632, 727; 98. Li, Y. et al. 2007, ApJ, 665, 187; 99. Menci, N. et al. 2006, ApJ, 647, 753; 100. Nagai, D. et al. 2007, ApJ, 668, 1; 101. Nath, B. & Roychowdhury, S. 2002, MNRAS, 333, 145; 102. Oh, S.P. & Benson, A. 2003, MNRAS, 342, 664; 103. Tescari, E. et al. 2011, MNRAS, 411, 826; 104. Tornatore, L. et al. 2010, MNRAS, 402, 1911; 105. Vernaleo, J. C. & Reynolds, C. S. 2007, ApJ, 671, 171; 106. Wiersma, R. C. P. et al. 2011, MNRAS, 415, 353